

# Dissertation

submitted to the

Combined Faculty of Mathematics, Engineering and Natural Sciences  
of the Ruperto-Carola-University of Heidelberg, Germany

for the degree of

Doctor of Natural Sciences

Put forward by

**Kathrin M. E. Kromer**

born in Freiburg im Breisgau (Germany)

**Oral examination: 21.05.2024**



Mass measurements on highly charged lead and uranium ions  
with the Penning-trap mass spectrometer PENTATRAP

Referees: Prof. Dr. Klaus Blaum  
Prof. Dr. Selim Jochim



## Massenmessungen an hochgeladenen Blei und Uran Ionen mit dem Penningfallen-Massenspektrometer PENTATRAP

Mit dem Penningfallen-Massenspektrometer PENTATRAP ist es möglich, Massenverhältnisse mit einer relativen Ungenauigkeit von einigen  $10^{-12}$  zu bestimmen. Erreicht wird dies durch die Verwendung eines Stapels von fünf zylindrischen Penningfallen in einem starken, homogenen 7 T-Magnetfeld, das gegen Umwelteinflüsse stabilisiert ist und dadurch phasensensitive Nachweisverfahren für einzelne hochgeladene Ionen ermöglicht. Kernstück dieser Arbeit sind drei begutachtete Publikationen, die Messungen des Massenspektrometers PENTATRAP beschreiben. Die erste Publikation stellt die Bestimmung der Atommasse von Blei-208 dar und die zweite beschreibt die Messung der Atommasse von Uran-238. Beide Messungen erfolgten mit bisher unerreichten Präzisionen im schweren Massenbereich von 7 bzw.  $6 \times 10^{-11}$ . Diese Ergebnisse tragen direkt zum "Massen-Rückgrat" bei, einer Reihe von Nukliden, deren Masse mit hoher Präzision bekannt ist, was eine Verbesserung der relativen Massenmessungen im Bereich der schweren und superschweren Nuklide, sowie die Bestimmung des  $g$ -Faktors des gebundenen Elektrons in schweren, wasserstoffähnlichen Ionen ermöglicht. In der dritten Publikation wird die Messung eines metastabilen Zustandes mit einer Energie von etwa 31 eV in  $^{208}\text{Pb}^{41+}$  als Massendifferenz relativ zur absoluten Masse des Blei-Ions von  $\approx 194 \text{ GeV}/c^2$  gezeigt und mit zwei *ab initio* Multikonfigurations-Dirac-Hartree-Fock-Atomstrukturberechnungen verglichen.

## Mass measurements on highly charged lead and uranium ions with the Penning-trap mass spectrometer PENTATRAP

With the Penning-trap mass spectrometer PENTATRAP it is possible to carry out mass ratio determinations with a relative uncertainty of a few times  $10^{-12}$ . This is achieved by using a stack of five cylindrical Penning traps in a strong, homogeneous 7 T magnetic field, stabilized against environmental influences, which allows phase-sensitive detection methods on single highly charged ions. The core of this thesis are three peer-reviewed publications that present measurements with the mass spectrometer PENTATRAP. The first and second publication present the determination of the atomic mass of lead-208 and uranium-238 to an unparalleled precision in the heavy mass sector of 7 and  $6 \times 10^{-11}$ , respectively. These results directly contribute to the mass "backbone", a number of nuclides whose mass is known to high precision, allowing one to improve relative mass measurements in the range of heavy and superheavy nuclides as well as to determine the  $g$ -factor of the bound electron in heavy, hydrogenlike ions. In the third article, a metastable state with an excitation energy of around 31 eV was measured in  $^{208}\text{Pb}^{41+}$  as a mass difference on top of the absolute mass of the lead ion of  $\approx 194 \text{ GeV}/c^2$  and compared to two *ab initio* multiconfiguration Dirac-Hartree-Fock atomic-structure calculations.



# Contents

<b>List of Figures</b>	<b>iii</b>
<b>List of Tables</b>	<b>iii</b>
<b>1 Introduction</b>	<b>1</b>
1.1 Mass-ratio determinations on heavy, highly charged ions . . . . .	1
1.1.1 Applications in nuclear physics of heavy nuclides . . . . .	1
1.1.2 Testing quantum electrodynamics with the $g$ -factor of the bound electron	3
1.1.3 Clocks based on highly charged ions . . . . .	5
1.2 Structure of this thesis . . . . .	7
<b>2 Experimental Techniques</b>	<b>9</b>
2.1 The ideal Penning trap . . . . .	9
2.2 Ion detection . . . . .	12
2.2.1 Non-destructive ion detection and cooling . . . . .	12
2.2.2 Mass-ratio measurement . . . . .	15
2.3 The real Penning trap . . . . .	16
2.3.1 Electric field . . . . .	16
2.3.2 Magnetic field . . . . .	16
2.4 Image charge shift . . . . .	16
<b>3 PENTATRAP</b>	<b>19</b>
3.1 Ion production and transport . . . . .	19
3.1.1 Double TipEBIT beamline . . . . .	21
3.2 Vertical beamline and trap tower . . . . .	24
<b>4 Publications</b>	<b>27</b>
4.1 High-precision mass measurement of doubly magic $^{208}\text{Pb}$ . . . . .	28
4.2 Atomic mass determination of uranium-238 . . . . .	39

4.3	Observation of a low-lying metastable electronic state in highly charged lead by Penning-trap mass spectrometry . . . . .	53
<b>5</b>	<b>Discussion</b>	<b>61</b>
5.1	The mass of lead-208 . . . . .	61
5.2	The mass of uranium-238 . . . . .	62
5.3	Observation of a low-lying electronic state in $^{208}\text{Pb}^{41+}$ . . . . .	63
5.3.1	Dip-lineshape uncertainty due to a shifting resonator . . . . .	63
5.3.2	Improvement strategies of the axial frequency determination . . . . .	65
5.3.3	Further investigation of the clock state $^2H_{11/2}$ in $\text{Pb}^{41+}$ . . . . .	67
5.3.4	Excited-state lifetime measurement . . . . .	68
<b>6</b>	<b>Summary</b>	<b>69</b>
	<b>Bibliography</b>	<b>79</b>



# List of Figures

1.1	Two neutron separation energy . . . . .	3
1.2	Atomic Mass Evaluation 2020: mass precision . . . . .	4
2.1	Cylindrical Penning trap . . . . .	10
2.2	Motion of an ion in an ideal Penning trap . . . . .	11
2.3	Axial dip signal . . . . .	13
2.4	Schematic of the pulse and phase technique . . . . .	14
3.1	TipEBIT sectional view . . . . .	20
3.2	The PENTATRAP beamline with two ion sources . . . . .	22
3.3	Future PENTATRAP beamline with two TipEBITs . . . . .	23
3.4	Time-of-flight spectrum of highly charged ions . . . . .	24
3.5	Vertical beamline and Penning-trap tower . . . . .	25
5.1	Atomic Mass Evaluation 2020: mass precision incl. new mass results . . . . .	63
5.2	Voltage of the correction electrode during transport . . . . .	64
5.3	Axial phase measurement . . . . .	66

# List of Tables

2.1	Exemplary set of ion trap frequencies at PENTATRAP . . . . .	12
-----	--	----



# 1 Introduction

## 1.1 Mass-ratio determinations on heavy, highly charged ions

The Penning-trap experiment PENTATRAP is aimed at mass-ratio determinations with a precision in the low  $10^{-12}$  [Repp 12, Roux 12a]. This precision is achieved by using single, highly charged ions with mass  $m_{\text{ion}}$  and charge  $q_{\text{ion}}$ , which increases the ion's cyclotron frequency

$$\nu_c = \frac{q_{\text{ion}}B}{2\pi m_{\text{ion}}} \quad (1.1)$$

inside the Penning trap with a magnetic field  $B$  compared to ions with low charge states. With a higher cyclotron frequency, the relative uncertainty will decrease if the absolute frequency determination remains at the same level. With this straightforward trick, PENTATRAP competes with the world's best mass-ratio determination experiments [Myer 13] which use e.g. the MIT two ion scheme [Rain 04, Rain 05].

At this level of precision, the applications of mass-ratio determinations are diverse and span across different fields of physics. The relevant ones for this thesis are nuclear physics, specifically in the heavy mass region, tests of quantum electrodynamics and the search for physics beyond the Standard Model via highly-charged-ion clocks in the extreme ultraviolet (XUV).

### 1.1.1 Applications in nuclear physics of heavy nuclides

One of the unique features of a nuclide is its mass. By measuring the mass of nuclides, the concept of a nuclear binding energy was postulated before the neutron had even been discovered [Asto 27]. Instead of integer numbers  $A$  of the lightest particle hydrogen, the measured masses showed a *mass defect*  $\delta_x$ , meaning the mass of a nuclide was lighter than the sum of its constituents: protons with mass  $m_p$  and electrons with mass  $m_e$  [Asto 27]:

$$M_{\text{atom}}(A) = Am_p + Am_e - \delta_x \quad (1.2)$$

The mass defect was a first hint to the forces binding the atom together, which led Arthur Eddington to predict the mechanism of fusion as the source of solar energy [Eddi 20]. The mass defect was later identified as the binding energies of the nucleus  $E_B(N, Z)$  and the electrons  $E_e(N, Z)$ :

$$M_{\text{atom}}(N, Z) = Nm_n + Zm_p + Zm_e - (E_B(N, Z) + E_e(N, Z))/c^2, \quad (1.3)$$

with the number of neutrons  $N$  and of protons  $Z$  in the nucleus. The nuclear binding energy, determined by precision mass measurements, initially rises with increasing mass number  $A$ , with a soft maximum at  $^{62}\text{Ni}$ , after which it decreases slowly [Kond 21]. With this, the chain of fusion reactions will have a natural end around iron and nickel since adding more nucleons would no longer be energetically favourable. This limits the nucleosynthesis due to fusion inside stars to the lighter elements. Heavier elements must be created by other processes, e.g. by the slow and rapid neutron capture, also called the *s-* and *r-process* [Lang 96].

Besides the investigation of nucleosynthesis, precision mass measurements can also contribute to the understanding of nuclear structure. Using the mass of a chain of isotopes, one can calculate the separation energy which is the energy necessary to remove a nucleon from the nucleus. The separation energies show a zig-zag pattern in energy between even and odd  $A$  isotopes that can be attributed to the two-nucleon pairing [Lunn 03] which is described in the nuclear shell model analogous to the electron shell model [Pove 01]. Besides the two-nucleon pairing, nuclear shell effects are especially striking when looking at the two-nucleon separation energies (the energy necessary to separate two nucleons from the nucleus), see Fig. 1.1 for the case of the two-neutron separation energy  $S_{2n}$ . Investigating two-nucleon separation energies removes the two-nucleon pairing pattern and reveals clear drops in separation energy at specific numbers of neutrons or protons, which can be attributed to shell closures similar to closed electron shells. The proton or neutron numbers which correspond to closed shells are called *magic numbers* [Maye 48], with the nuclei having both a magic proton and neutron number being called *doubly-magic*. The prediction of the next doubly-magic nucleus after lead-208 is of great interest to nuclear research to determine the center and extension of the *island of stability* in the nuclide chart, describing a region of superheavy nuclides that possess a longer lifetime due to the stronger bounds around a nuclear shell closure [Sobi 07, Ogan 12]. Without these nuclear shell effects, superheavy elements would instantaneously disintegrate due to Coulomb repulsion. While some magic numbers ( $Z = 82$  and  $N = 126$ ) correspond to spherical nuclei, others like the shell closure at  $N = 152$  appear in deformed nuclei [Juli 01, Bloc 22] which need advanced nuclear models to approximate [Nils 55].

In order to examine these effects, the Atomic Mass Evaluation (AME) evaluates all types of connections from inertial to energy measurements in order to form a comprehensive network of masses [Huan 21, Wang 21]. All relative measurements will have to be fixed to some masses

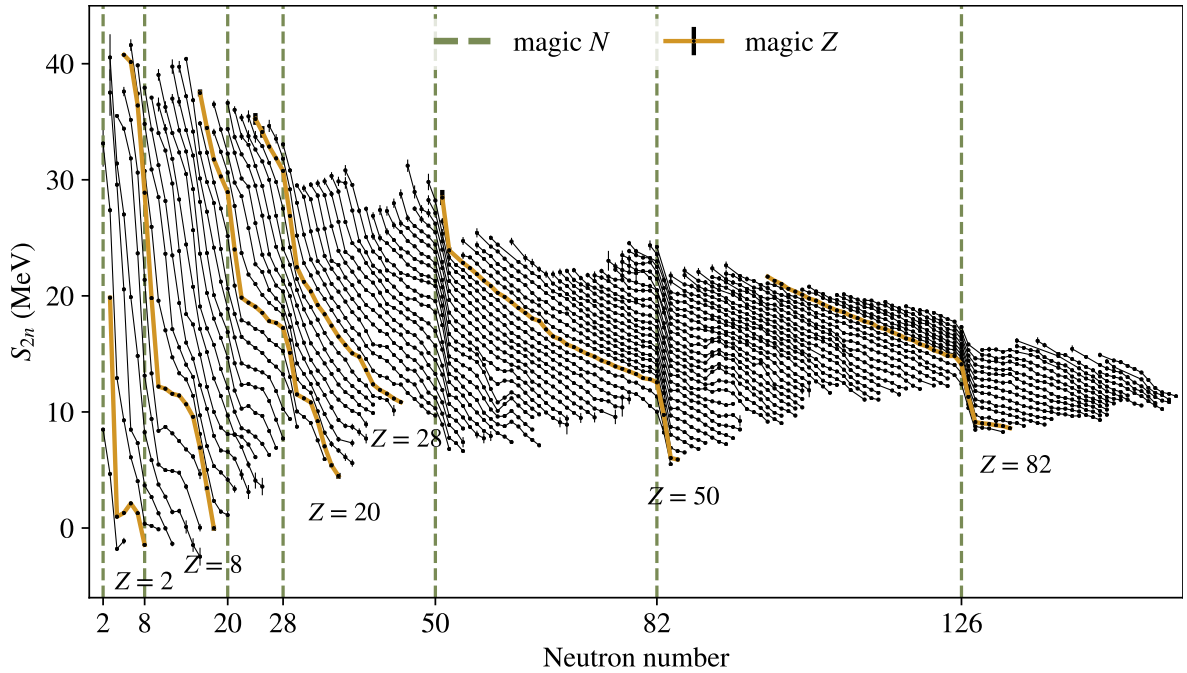


**Figure 1.1:** Two-neutron separation energies with clearly visible drops in energy at nuclear shell closures. Figure created by adapting the Python code [Kart 19a] and inputting data from the NUBASE2020 [Kond 21].

that are known absolutely to a high precision, called the *mass backbone* [Audi 12]. However, no nuclide beyond  $Z = 70$  was known to a relative precision of better than  $2 \times 10^{-9}$ , see the lack of blue-colored nuclides in the heavy mass region of Fig. 1.2. This limits measurements using heavy references to the same precision. In this thesis work, the mass precision of lead-208 and uranium-238 was improved by two orders of magnitude, using high-precision measurements in a Penning trap. With the improved precision of  $7 \times 10^{-11}$  and  $6 \times 10^{-11}$  (Pb and U) the mass backbone now extends to the heavy region of the nuclear chart, which directly improves the mass precision of several surrounding nuclides connected via relative energy measurements. Radionuclides are typically measured with a precision in the range of  $10^{-8} - 10^{-9}$  [Dwor 10, Hukk 23, Kart 19b], so these two nuclides present as excellent references for mass determinations up to the actinide region.

### 1.1.2 Testing quantum electrodynamics with the $g$ -factor of the bound electron

The theory of quantum electrodynamics (QED) describes the electromagnetic interaction by exchange of photons, and thus predicts all interactions of matter and light. Theoreticians can calculate energy levels of light atomic systems, like hydrogen, helium, muonium, etc., using expansions in  $\alpha$  and  $\alpha Z$ , where  $\alpha$  is the fine structure constant and  $Z$  the nuclear

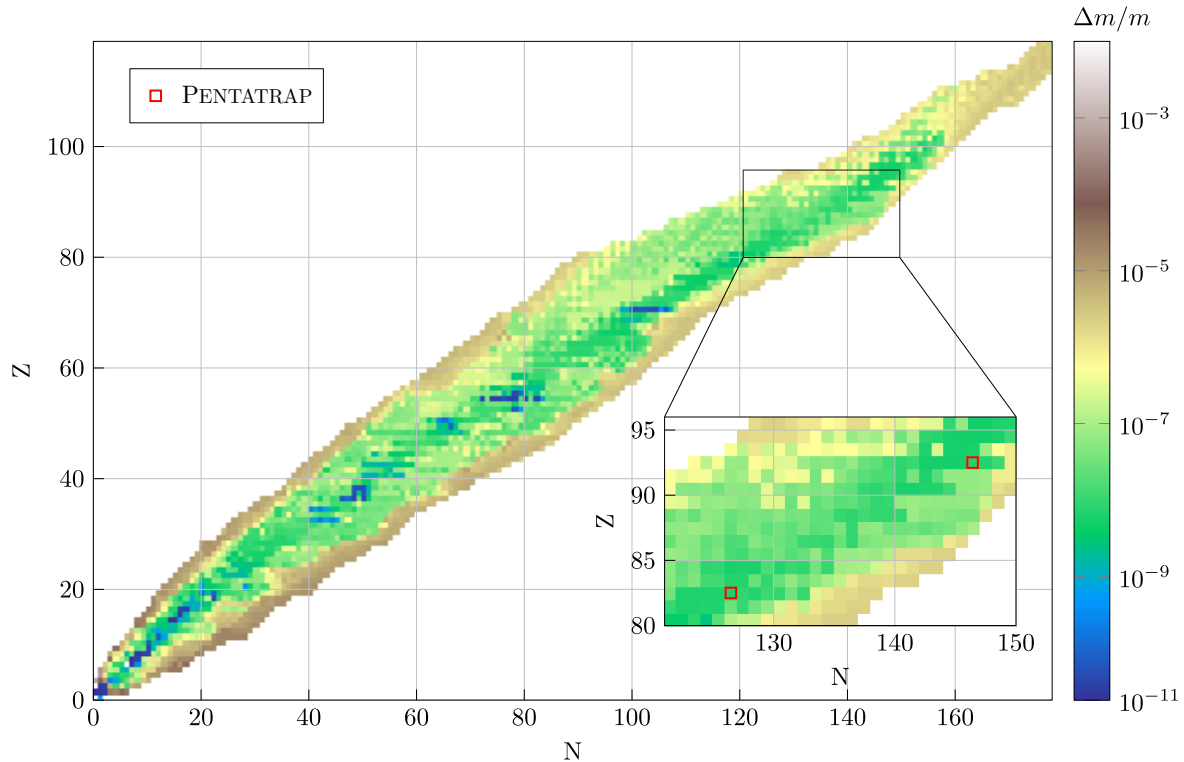


**Figure 1.2:** The nuclide chart indicating by color the mass precision of all nuclides that are listed in the AME2020 [Huan 21, Wang 21] prior to our measurements. The inset shows the heavy mass region and indicates with red squares lead-208 and uranium-238 which were determined to be the prime candidates for PENTATRAP to measure in order to elongate the mass backbone.

charge. By combining these calculations with spectroscopic data it is possible to test the QED predictions [Kars 05]. However,  $\alpha$  and  $\alpha Z$  of light systems are small numbers and the tests are therefore limited to only a few low orders. In order to extend these tests to higher orders, it was proposed to use highly charged ions (HCIs) or high- $Z$ , few-electron systems, that can be approximated using QED [Mohr 98]. Besides probing higher order QED terms, HCIs test QED in strong electric fields since the remaining electrons experience the interaction with the nucleus as a strong electric field, e.g. on the surface of a uranium nucleus this amounts to  $2.3 \times 10^{19}$  V/cm [Beie 00]. The investigation of HCIs is carried out, among others, in terms of the Lamb shift, hyperfine splitting or  $g$ -factor of the bound electron [Shab 18]. Stringent tests of QED are particularly carried out in HCIs with a single bound electron left, called hydrogenlike systems. The  $g$ -factor of HCIs can be measured in a Penning trap by combining a measurement of the cyclotron frequency  $\nu_c$ , see Eq. (1.1), with a measurement of the spin-precession or Larmor frequency  $\nu_L = geB/(4\pi m_e)$  of the bound

electron, using the relation [Brow 86]

$$g = 2 \frac{\nu_L}{\nu_c} \frac{q_{\text{ion}}}{e} \frac{m_e}{m_{\text{ion}}} = 2\Gamma_0 N_q \frac{m_e}{m_{\text{ion}}} . \quad (1.4)$$

In this formula, the charge ratio  $N_q$  is an integer number, the mass ratio  $m_e/m_{\text{ion}}$  needs to be measured separately, and the frequency ratio  $\Gamma_0$  is measured at experiments like ALPHATRAP at the Max-Planck-Institute for Nuclear Physics in Heidelberg, Germany [Stur 19] or at ARTEMIS at the GSI in Darmstadt, Germany [Voge 19]. As can be seen in Eq. (1.4), the precision of the mass ratio needs to match or exceed the precision of the frequency ratio  $\Gamma_0$  in order not to limit the  $g$ -factor determination. The mass of the electron  $m_e$  is known to a precision of  $3 \times 10^{-11}$  [Stur 14, Zato 17], which is precise enough for the current  $g$ -factor determination on heavy HCI. In fact, the mass of the electron is extracted from a  $g$ -factor measurement in light systems in which the QED is better tested. Here, the argument can be turned around by using e.g. a carbon-12 ion<sup>1</sup> trusting the theory input  $g$ -factor, and in turn extracting the electron mass  $m_e$  from Eq. (1.4). Since the mass  $m_e$  is known very precisely, it means that the  $g$ -factor determination of heavy ions and with it the quality of QED test will be determined by the frequency ratio measurement of  $\Gamma_0$ , the mass of the ion of interest, and the theoretical determination of the  $g$ -factor.

The teams at ALPHATRAP and ARTEMIS plan to investigate HCI systems of up to hydrogenlike uranium [Voge 19, Morg 23]. However, as described in Sec. 1.1.1, no nuclide beyond  $Z = 70$  was known to a relative precision better than  $2 \times 10^{-9}$  [Huan 21, Wang 21] before the start of this thesis work, while the team of ALPHATRAP has already shown their capability of measuring the frequency ratio  $\Gamma_0$  on a level of a few times  $10^{-11}$  up to  $Z = 50$  [Morg 23]. The aim was therefore to provide high-precision mass values of some heavy nuclides, so they can be used for the investigation of the  $g$ -factor of the bound electron. In Sec. 4.1 and Sec. 4.2 the masses of two high- $Z$  nuclides, lead-208 and uranium-238, were measured to high precision. These nuclides as well as the connected nuclides, whose masses were indirectly improved, are good candidates to be used for future  $g$ -factor determinations. In case the binding energies of the remaining electrons of the HCI might become a limiting factor for the  $g$ -factor determination, there is the possibility to connect the ion source of the ALPHATRAP experiment to the beamline of the PENTATRAP experiment. It would thereby be possible to measure the mass of the ion directly in the correct charge state in order to be independent of theoretical binding energy calculations.

### 1.1.3 Clocks based on highly charged ions

Optical atomic clocks have reached incredible fractional frequency stabilities since the invention of the frequency comb [Hall 06, Hans 06] and have, in the meantime, surpassed

---

<sup>1</sup>Since atomic carbon-12 defines the SI unit  $u$ , the mass of a carbon ion is very well known.

microwave based standards [Ludl 15]. This was possible due to the higher frequency of the optical transitions. The logical next step would be to increase the clock frequency even more and push clocks into the ultraviolet regime. Thanks to the rapid technical development in the field of frequency combs, they are now available up to the extreme ultraviolet (XUV) [Gohl 05, Jone 05, Pupe 13, Cars 16, Saul 19, Pupe 21]. To push the next generation of clocks even further, HCIs have been proposed to replace the neutral or singly charged ions that have been utilized as standards until now [Bere 10, Cres 16]. The advantage in HCIs lies in the remaining electrons being orders of magnitude stronger bound to the nucleus. On the one hand, this shields HCIs from perturbations due to external fields like blackbody radiation [Yudi 14]. On the other hand, it increases their sensitivity to new physics, e.g. a potential variation of the fine structure constant  $\alpha$  [Cres 16, Kozl 18].

HCIs, however, have two disadvantages: firstly, they tend to lack fast optical cooling and state readout transitions and secondly, their structure is not as well understood as that of neutral atoms or singly charged ions, making it difficult to find narrow clock transitions. Recently, a group at the Physikalisch Technische Bundesanstalt (PTB) in Braunschweig, Germany, has successfully tackled the first of the problems by implementing the Quantum Logic Method in a first HCI clock [Mick 20, King 22]. Tackling the second problem is where mass spectrometry comes into play: In 2020, our group has discovered that we can distinguish between an ion in a ground state and an ion in an electronically excited state, if the excited state lives long enough for us to load it into our Penning-trap mass spectrometer and compare its frequency to that of an ion in the ground state [Schu 20]. This metastable state does not need to be driven actively with that form of measurement, since the excited state is populated automatically during the electron impact ionization: the ions are in highly excited states inside the ion plasma at the center of the electron beam ion trap used for ion breeding and a fraction of the HCIs cascades down to the metastable state during deexcitation.

The excited state can only be detected in a Penning trap if it lives long enough for the ion to be loaded into the trap. At the same time, a long lifetime  $\tau$  means a narrow natural linewidth  $\Delta\nu = 1/(2\pi\tau)$  and therefore a potentially very precise clock. By determining the excited state energy, Penning-trap mass spectrometry can test state-of-the-art atomic structure calculations and help in the discovery of clock states in HCIs. With this technique one can determine transitions in the XUV to a precision of around 1 eV, taking a first step towards being able to drive the transition with an XUV laser.

While the publication [Schu 20] describes the first energy measurement of an excited state in a Penning trap, the energy of that particular metastable state of around 200 eV corresponds to a transition frequency that lies outside the range of lasers and frequency combs that could be used to build a clock. Hence, the next goal was to find a transition that is lower in energy to reach the range of application of the existing XUV frequency combs. This was achieved



in the publication in [Sec. 4.3](#) where a metastable state of around 30 eV was measured as a mass difference of the excited state ion against the ground state ion. With the ion's mass of around 200 GeV/c<sup>2</sup>, the small mass difference to the metastable state was measured with an uncertainty of 0.8 eV, making it the most precise mass-ratio determination at the time of publication with a relative precision of  $4 \times 10^{-12}$ . The measurement of the metastable state energy further benchmarks challenging atomic structure calculations on open-shell ions that can be used to predict energy levels in similar ions [[Lyu 23a](#)].

## 1.2 Structure of this thesis

In this cumulative thesis, three recent publications will be introduced, presenting high-precision mass determinations with the aforementioned physics applications. Starting with an overview of the basic principles of mass determinations in Penning traps in [Chap. 2](#), where the differences between an ideal, theoretical Penning trap and the real version found in our laboratory will be described. This chapter will give insight into the mechanisms of the non-destructive ion detection technique of a single ion in a Penning trap. Specifics about the experiment PENTATRAP and its main components for ion production and transport can be found in [Chap. 3](#). Following this, the three peer-reviewed publications, forming the core of this thesis, are presented. Starting with the publication of the atomic mass of lead-208 in [Sec. 4.1](#), then continuing with the paper on the atomic mass of uranium-238 in [Sec. 4.2](#). The second paper includes supplemental material describing the systematic measurements in detail, including a precise image charge shift measurement, which was the limiting experimental uncertainty during the ion mass-ratio measurement of lead-208. The last publication in [Sec. 4.3](#) describes the measurement and theoretical calculation of a metastable electronic state in Nb-like Pb<sup>41+</sup>. The mass determination reached a fractional uncertainty of  $4 \times 10^{-12}$ . Following the publications, there will be a discussion of the measurements and their main limitations including prospects for future improvements of the measurement methods.



# Experimental Techniques

“Never measure anything but frequency!”, Arthur Schawlow, the 1981 Nobel Prize winner in physics, recommended [Hans 06]. What he wanted to emphasize was, that frequency or the number of cycles during a given time interval is the quantity which one can measure to the highest precision. Penning traps align perfectly with this statement, as the mass of a charged particle is directly accessible by measuring its trapping frequencies. The Penning trap, invented in 1959 by Hans Georg Dehmelt, combines a strong homogeneous magnetic field with an electrostatic quadrupolar field for three-dimensional confinement of a charged particle. The motional frequencies of the trapped particle depend on their mass and are nowadays frequently used for some of the most precise mass determinations [Rain 05, Fink 20, Fili 21, Sasi 23]. In the following chapter, the basic principles of physics governing the particle movement inside a Penning trap and the relevant single-ion detection techniques and measurement schemes will be described, as well as the influence of subideal conditions on the trapping frequencies.

## 2.1 The ideal Penning trap

A charged particle with charge  $q$  and mass  $m$  in a homogeneous magnetic field  $B$  will oscillate on a circular trajectory around the field lines with the free cyclotron frequency

$$\nu_c = \frac{qB}{2\pi m}. \quad (2.1)$$

With the magnetic field, the particle will be confined in radial direction but can still escape in axial direction. In order to confine the particle in all three dimensions, an electrostatic potential  $\Phi$  is formed by applying voltages to a set of trap electrodes that lead to oscillations parallel to the magnetic field lines. In order for this oscillation frequency to be independent of the motion’s amplitude, a harmonic potential needs to be applied. With a Penning trap with cylindrical electrodes, at least two correction electrodes, and appropriately applied correction voltages a harmonic potential can be approximated in the relevant region

for ion trapping. The cylindrical electrode structure used within this thesis can be seen in Fig. 2.1. The potential can be approximated around the trap center in cylindrical coordinates as a series of Legendre polynomials  $P_n$  with purely even orders due to the axial symmetry  $z \rightarrow -z$  [Gabr 89]

$$\Phi(z, \rho) = V_0 \sum_{n=1}^{\infty} C_n (z^2 + \rho^2)^{n/2} P_n \left( \frac{z}{\sqrt{z^2 + \rho^2}} \right). \quad (2.2)$$

If the coefficients  $C_n = 0$  for  $n > 2$ , Eq. (2.2) describes the ideal quadrupolar field. Higher order terms ( $C_4, C_6, \dots$ ) are undesirable and must be minimized by careful design of the electrode geometry.

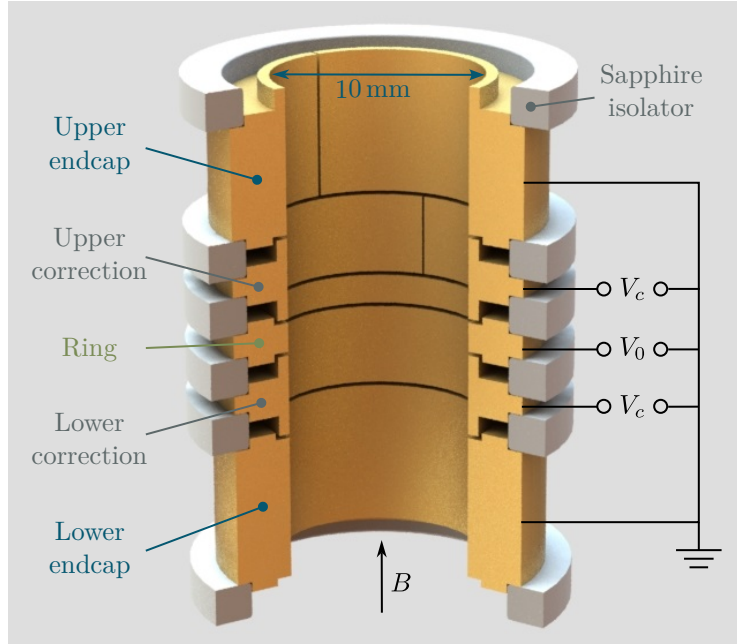


**Figure 2.1:** CAD rendering of a sectional-view of the cylindrical trap electrode geometry used at PENTATRAP. The applied voltages  $V_c$  at the correction electrode and  $V_0$  at the ring electrode are shown, as well as the direction of the magnetic field  $B$ .

The motion of the stored particle in this combination of homogeneous magnetic and quadrupolar electrostatic field is composed of three independent eigenmotions, see Fig. 2.2: A fast modified cyclotron motion in radial direction with frequency  $\nu_+$ , a slower axial motion with frequency  $\nu_z$  due to the electric field, and the slowest motion called magnetron motion with frequency  $\nu_-$  corresponding to a radial drift around the trap center. The frequencies

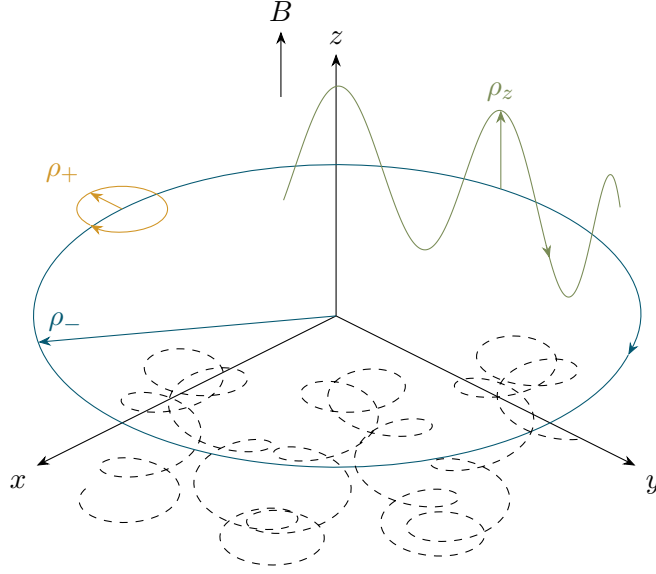


**Figure 2.2:** Schematic of the three eigenmotions of an ion inside a Penning trap. The dashed line shows the addition of all three motions, which is the full ion motion. The motional radii  $\rho$  are scaled for better visibility.

can be calculated as follows [Brow 86]:

$$\nu_z = \frac{1}{2\pi} \sqrt{\frac{2qV_0C_2}{m}} \quad (2.3)$$

$$\nu_+ = \frac{\nu_c}{2} + \sqrt{\frac{\nu_c^2}{4} - \frac{\nu_z^2}{2}} \approx \nu_c - \frac{1}{2\pi} \frac{2C_2V_0}{B_0} \quad (2.4)$$

$$\nu_- = \frac{\nu_c}{2} - \sqrt{\frac{\nu_c^2}{4} - \frac{\nu_z^2}{2}} \approx \frac{1}{2\pi} \frac{2C_2V_0}{B_0} \quad (2.5)$$

The free cyclotron frequency can be calculated from the three eigenmotions for the determination of the ion's mass either by the sideband relation [Brow 86]

$$\nu_{c,\text{sb}} = \nu_+ + \nu_- \quad , \quad (2.6)$$

or by using the invariance theorem which can be derived from Eq. (2.5) and Eq. (2.4)

$$\nu_c = \sqrt{\nu_+^2 + \nu_z^2 + \nu_-^2} \quad . \quad (2.7)$$

The invariance theorem has the advantage of being invariant against first order imperfections like a tilting angle of the electrostatic trap against the magnetic field or an ellipticity of the quadrupolar field [Brow 82]. The eigenfrequencies of the ions follow a strong hierarchy, see Tab. 2.1, therefore, the larger frequencies will have to be determined to a higher precision.

**Table 2.1:** Typical eigenfrequencies and trapping voltages at PENTATRAP based on the example of the ions used during the lead measurement campaign.

	Trap 2		Trap 3	
	$^{132}\text{Xe}^{26+}$	$^{208}\text{Pb}^{41+}$	$^{132}\text{Xe}^{26+}$	$^{208}\text{Pb}^{41+}$
$V_0$ (V)	-38.2027	-38.1980	-17.7205	-17.7185
$\nu_-$ (Hz)	12 936	12 934	6 005	6 004
$\nu_z$ (Hz)	740 285	740 286	504 456	504 459
$\nu_+$ (Hz)	21 184 119	21 186 776	21 191 076	21 193 731
$\nu_c$ (Hz)	21 197 054	21 199 709	21 197 080	21 199 735

## 2.2 Ion detection

A single ion in a Penning trap can live for days in ultra high vacuum (UHV) and at cryogenic temperatures- or even up to months if the vacuum trapping region is sealed or pinched off. To make use of these long lifetimes, a non-destructive detection technique is imperative.

### 2.2.1 Non-destructive ion detection and cooling

The non-destructive detection of an ion movement in a Penning trap can be achieved by detecting the current the ion movement induces in the trap electrodes. This small current on the order of a few fA, is also known as image current. For the detection of the axial image current and thereby the axial frequency, a superconducting inductance  $L$  is connected to an axially offset electrode. Together with the parasitic capacitance of the trap itself  $C$  and small, but finite parasitic losses throughout the circuit  $R$ , this forms an  $RLC$  or tank circuit. By adjusting the trapping voltage  $V_0$ , one can tune the ion's axial frequency to the resonance frequency of the tank circuit (further: resonator frequency). Once close enough to the resonator frequency, the ion will become visible as a peak in the noise spectrum at the ion's axial frequency [Feng 96]. The tank circuit is connected to two stages of low-noise amplifiers to make the small voltage drop measurable. For details on the cryogenic and room temperature electronics used in this thesis see [Roux 12b, Dorr 15, Risc 18].

### Dip technique

In addition to acting as a detection method, the resonant coupling of the ion's axial motion to the tank circuit will reduce the amplitude of the axial motion due to energy losses in the tank circuit which acts as a heat bath at  $\approx 4$  K. The Fourier transform of the resulting signal after thermalization shows a dip at the axial frequency in the Johnson-Nyquist noise of the

resonator, see Fig. 2.3. The mathematical description of the ion-resonator interaction and analytical fit function can be found in [Feng 96].

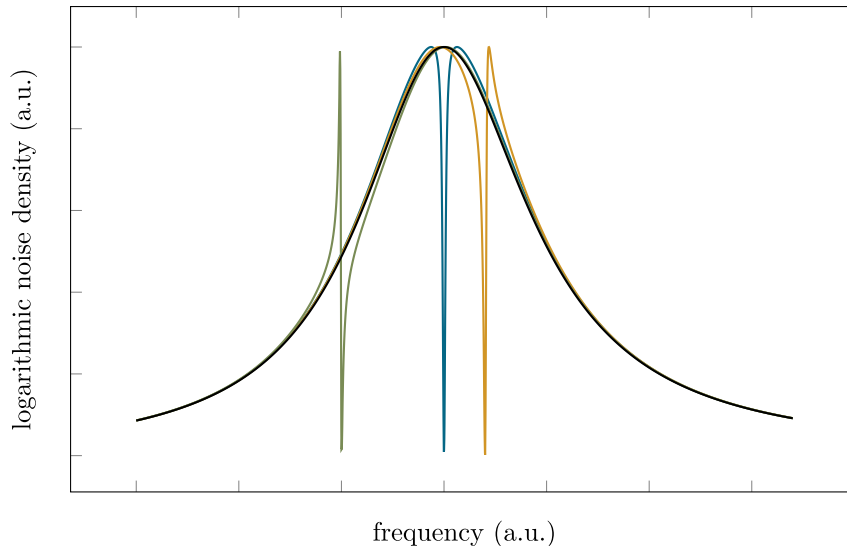


**Figure 2.3:** Three solutions for the interaction of the detection circuit with the ion’s image current. In blue, the axial frequency of the ion matches the resonator frequency, in yellow and green, the axial frequency is shifted away from the resonator.

For measuring and cooling the radial motions of the ion without any additional tank circuits at different resonator frequencies, one can couple either one of the radial motions to the axial motion by applying a radio frequency (rf) sideband drive at  $\nu_{\text{rf},\pm} = \nu_{\pm} \mp \nu_z$ . The single axial dip will split up into a double dip with frequency  $\nu_l$  of the left dip and  $\nu_r$  of the right dip which can be used to calculate the radial frequencies

$$\nu_+ = \nu_{\text{rf},+} + \nu_l + \nu_r - \nu_z \text{ and} \quad (2.8)$$

$$\nu_- = \nu_{\text{rf},-} - \nu_l - \nu_r + \nu_z . \quad (2.9)$$

It should be mentioned that the dip and double dip technique relies on a model-based fit which is only as good as the model itself. Within the publications in Chap. 4, fit-related systematic uncertainties will be described.

### PnP technique

For high-precision frequency determinations, the phase-sensitive pulse and phase (PnP) technique is applied throughout this thesis [Corn 89]. The technique, graphically depicted in Fig. 2.4, is made up of four steps. First, the initially cooled ion’s modified cyclotron motion is excited by an rf pulse at frequency  $\nu_+$  to set an initial phase  $\phi_0$ . Then, during the phase accumulation time  $t_{\text{acc}}$ , the ion’s modified cyclotron motion can evolve freely to accumulate

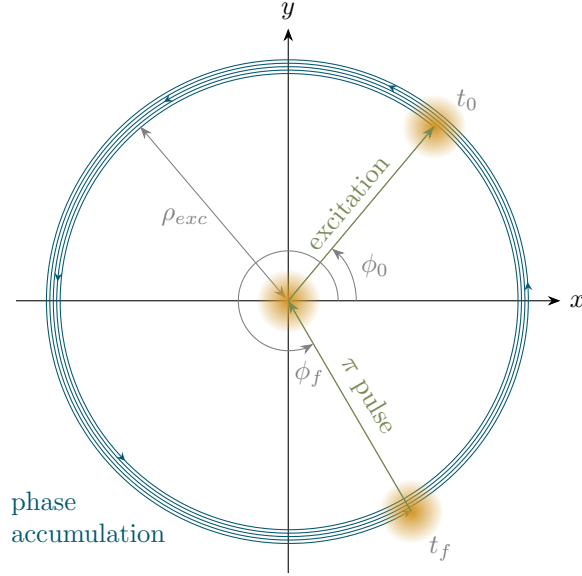


**Figure 2.4:** The modified cyclotron motion during the PnP cycle which starts with an excitation, followed by the phase accumulation and ending with the coupling  $\pi$  pulse. The thermal amplitude spread is indicated by the yellow circles. The different blue rings during the phase accumulation time are only for illustrative reasons and do not signify an increasing radius.

its final phase  $\phi_f$ . In order to read out the phase, the amplitude as well as the phase information of the modified cyclotron motion is transferred to the axial motion by applying a  $\pi$  pulse at the sideband frequency  $\nu_{rf} = \nu_+ - \nu_z$ . Lastly, the transferred phase can be read out as an axial phase using the tank circuit. For any residual amplitude in the modified cyclotron mode due to an imperfect  $\pi$ -pulse conversion, the modified cyclotron mode is coupled to the axial mode after each PnP cycle to cool the radial mode again.

The final readout phase  $\phi_f$  relates to the modified cyclotron frequency

$$\nu_+ = \frac{1}{2\pi} \frac{\Delta\phi + 2\pi N}{t_{acc}}, \quad (2.10)$$

with  $\Delta\phi = \phi_f - \phi_0$  being the accumulated phase during  $t_{acc}$  modulo  $2\pi$ .  $N$  is the number of full turns between excitation and phase readout. To determine this number, a preparatory measurement is carried out where phases at different  $t_{acc}$  are measured and then the frequency  $\nu_+$  is calculated for which the number  $N$  becomes integer for all the measured phase accumulation times. Typical phase accumulation times at PENTATRAP lie between 40 s and 100 s for heavy ions. In Eq. (2.10), we can directly see that when measuring phase sensitively, the uncertainty of the frequency determination scales with  $1/t$ , whereas a frequency determination with the dip method relies on incoherent sampling of electrical noise whose uncertainty only improves with  $1/\sqrt{t}$ . The PnP measurement of  $\nu_+$  can be combined with



a simultaneous axial dip measurement during the phase accumulation time to decrease the influence of field drifts on the determination of the free cyclotron frequency.

The PnP technique can be employed for the magnetron mode as well, which has been done for the first time at PENTATRAP within this thesis work, described in Sec. 4.2, to determine the image charge shift systematic [see Sec. 2.4]. In the typical measurement scheme for mass determinations, a magnetron frequency determination using the double dip technique at the beginning of each measurement run suffices, since the impact of the magnetron uncertainty in the cyclotron frequency determination via the invariance theorem Eq. (2.7) is small compared to the other eigenfrequencies due to the strong frequency hierarchy.

### 2.2.2 Mass-ratio measurement

As mentioned before, masses are determined by measuring the three eigenfrequencies and combining them to calculate the free cyclotron frequency  $\nu_c$ , using the invariance theorem in Eq. (2.7). Since the cyclotron frequency depends on the magnetic field strength  $B$  at the trap center, the mass precision by measuring  $\nu_c$  would be limited to the precision of the magnetic field characterization. In order to overcome this limitation, mass measurements are typically done as relative mass-ratio measurements. In relative measurements two ions are used whose  $\nu_c$  will be measured alternately and afterwards the frequency ratio

$$R = \frac{\nu_{\text{ioi}}}{\nu_{\text{ref}}} = \frac{q_{\text{ioi}} m_{\text{ref}}}{q_{\text{ref}} m_{\text{ioi}}} \quad (2.11)$$

is formed, with  $m_{\text{ioi}}$ ,  $q_{\text{ioi}}$  being the mass and charge of the ion of interest and  $m_{\text{ref}}$ ,  $q_{\text{ref}}$  the mass and charge of the reference ion. By forming the ratio, the magnetic field is cancelled in this equation. As an ideal reference ion, one would use carbon-12 since its atomic mass is the basis for the definition of the atomic mass unit  $u$ . However, some systematic uncertainties increase with the mass difference between the ion of interest and the reference ion. For heavy ions it is therefore common to use a reference ion closer in mass whose atomic mass is known to enough precision. In order to calculate back to the atomic mass of the nuclide of interest, one needs to calculate the mass of the reference ion

$$m_{\text{ref}} = m_{\text{ref}}^{\text{atom}} - q_{\text{ref}} m_e + E_{\text{ref}} , \quad (2.12)$$

with the neutral atomic mass of the reference nuclide  $m_{\text{ref}}^{\text{atom}}$  taken from the AME [Wang 21] and  $m_e$  the mass of the electron. The binding energy of the missing electrons of the reference ion  $E_{\text{ref}}$  as well as the ion of interest  $E_{\text{ioi}}$  needs to be supplied by other experimental data or, in our case of heavy, highly charged ions, by advanced atomic structure calculations. With the mass of the reference ion, the atomic mass of the nuclide of interest  $m_{\text{ioi}}^{\text{atom}}$  can be calculated

$$m_{\text{ioi}}^{\text{atom}} = \frac{1}{R} \frac{q_{\text{ioi}}}{q_{\text{ref}}} m_{\text{ref}} + q_{\text{ioi}} m_e - E_{\text{ioi}} . \quad (2.13)$$

## 2.3 The real Penning trap

Contrary to what has been described in the previous chapter, the reality in the lab deviates from the theoretical Penning trap.

### 2.3.1 Electric field

The electric potential in the Penning trap, see Eq. (2.2), ideally is a quadrupolar field with coefficients  $C_n = 0$  for  $n > 2$ . In reality, however, machining tolerances as well as misalignment lead to nonzero higher order coefficients. By optimizing the tuning ratio  $TR = V_0/V_c$  the coefficient  $C_4$  can be minimized, however, the uncertainty of the  $TR$  determination as well as higher order corrections create remaining systematic uncertainties of the eigenfrequencies. For details and the explicit expressions for the main frequency shifts, see [Kett 14]. The systematic  $C_4$  and  $C_6$  shifts from the uranium-238 mass campaign can be found in the Supplemental Material of Sec. 4.2.

### 2.3.2 Magnetic field

Similar to the electric potential, the magnetic potential deviates from its homogeneous form. The real magnetic field is not fully homogeneous but can be described by a polynomial

$$B(z) = B_0 + B_1 z + B_2 z^2 + \dots, \quad (2.14)$$

with coefficients  $B_n$  which can be determined when carrying out systematic measurements. For example,  $B_1$  is determined by displacing the ion's center of oscillation in axial direction, calculating the new center of the ion's oscillation in  $z$ -direction and then measuring the cyclotron frequency of the ion in dependence of its position in  $z$ -direction. For a description of the systematic measurements of  $B_1$  and  $B_2$  at PENTATRAP, see [Door 18].

Once measured, the systematic shifts for the trap frequencies can be calculated by the use of the explicit expressions in [Kett 14]. The results of the  $B_2$  measurement from the uranium-238 mass campaign can, again, be found in the Supplemental Material of Sec. 4.2.

## 2.4 Image charge shift

The image charge induced in the trap electrodes creates an additional electric field which acts back on the ion, shifting the frequencies. The resulting systematic shift of the free cyclotron frequency is called image charge shift (ICS). The ICS scales with the mass of the ion and will be especially significant in mass-ratio determination for measurements in which the reference ion has a large mass difference  $\Delta m$  compared to the ion of interest. In this

thesis two such measurements with large  $\Delta m$  were carried out, see [Sec. 4.1](#) and [Sec. 4.2](#). In these measurements the leading systematic shift was the ICS.

The ICS for a cylindrical Penning trap can be estimated by the use of the analytical solution for the image charge shift in an infinitely long cylinder [[Haff 00](#)]

$$\frac{\Delta\nu_c}{\nu_c} \approx \left( -\frac{\nu_+}{\nu_c} + \frac{\nu_-}{\nu_c} \right) \frac{m}{4\pi\epsilon_0 r_0^3 B_0^2}, \quad (2.15)$$

with the radius of the trap  $r_0$  and the vacuum permittivity  $\epsilon_0$ . The approximation with the solution for an infinitely long cylinder evokes an uncertainty of 5 % of the calculated shift of the ratio [[Schu 19a](#)]. For the measurements described in this thesis, the ICS is on the order of  $2 \times 10^{-10}$  which means 5 % of this determination corresponds to a systematic uncertainty on the order of  $10^{-11}$ , which will limit the experimental ratio determination. In order to go below this 5 % uncertainty, we decided to measure the image charge shift in the case of the uranium-238 measurement campaign, using a phase-sensitive detection method of the magnetron frequencies. A final uncertainty of the systematic ICS of 0.8 % in Trap 2 and 1.7 % in Trap 3 was achieved. For the description of the ICS measurement and the determination of all other relevant systematic shifts, see the Supplemental Material of [Sec. 4.2](#).



# PENTATRAP

PENTATRAP is an experiment aimed at mass determinations of heavy, highly-charged and long-lived ions. The use of highly-charged ions (HCIs) increases the free cyclotron frequency, see Eq. (2.1), and thereby allows to reach a better relative precision. In addition, the high charge states create a larger image current inside the trap electrodes, making cooling and detection faster. Furthermore, with a multitude of charge states available, one can choose similar charge-to-mass or  $q/m$  ratios for the ion of interest and the reference ion. This decreases most systematic effects which scale with  $q/m$ , allowing the use of reference ions far away in mass from the ion of interest. With this technique, PENTATRAP has produced high-precision mass data for a series of publications [Risc 20, Schu 20, Fili 21, Heis 23].

To allow the creation of high charge states, the ion source at PENTATRAP is located outside of the cryogenic trapping region. The whole experiment is composed of two external ion sources connected via electrostatic and magnetic beamlines to a Penning-trap tower containing 5 cryogenic Penning traps inside a 7 T magnet. The Penning-trap tower and its electronic components have remained mostly unchanged in recent years and are described in detail in [Roux 12a, Repp 12, Schu 19b, Risc 18]. This chapter will, therefore, focus on the experimental updates mainly to the ion production and transport sections.

## 3.1 Ion production and transport

The ion production of PENTATRAP is achieved in two electron beam ion traps (EBITs). The first one is a Heidelberg compact EBIT, built according to the model of [Mick 18] and extended by a laser ablation source [Schw 19], see Fig. 3.1. This EBIT is called TipEBIT due to the shape of the sample holders. The TipEBIT shoots an electron beam of several milliamperes from the electron gun (composed of cathode, anode, and focus electrode, see Fig. 3.1) towards the trap center. During flight, the electron beam is focused by the magnetic field of 72 permanent magnets and a soft-iron yoke. The TipEBIT offers two possibilities to

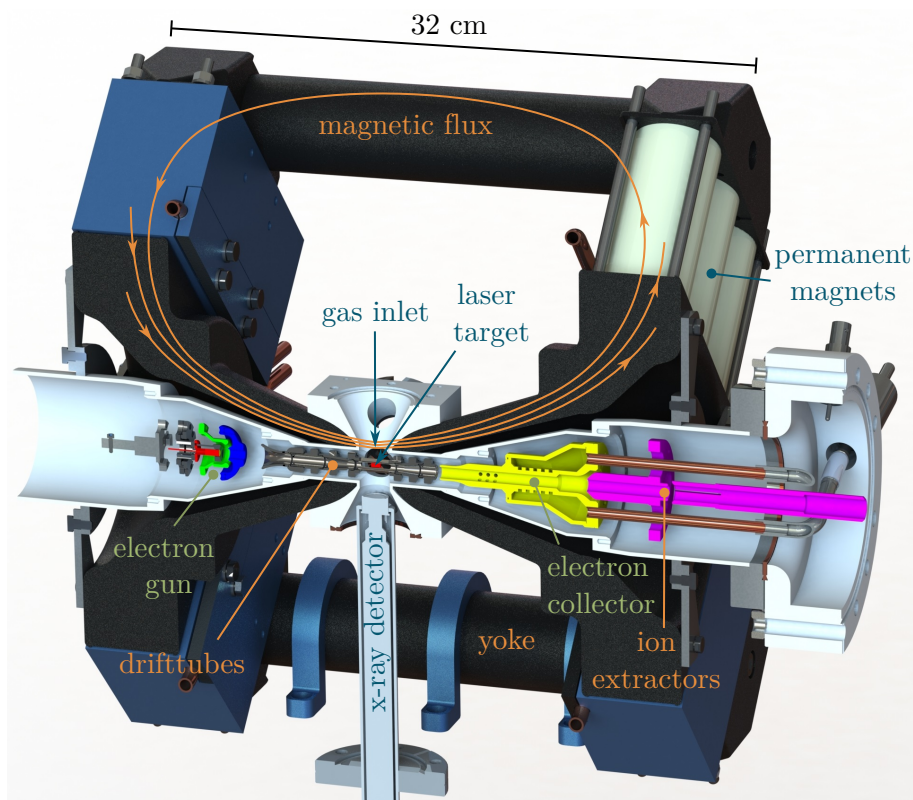


**Figure 3.1:** Sectional view of the CAD model of the TipEBIT stripped of most insulators and spacers for better view of the main components. The electron gun is made up of a cathode drawn in red, a focus electrode in green, and an anode in blue. The laser is not shown here but is located on the opposite side of the target.

load neutral and singly charged ions into the EBIT: One can either use the differentially pumped, collimating gas inlet system (not depicted in Fig. 3.1) or shoot an ablation laser onto the laser target (depicted in red in Fig. 3.1) located right next to the trap center in close proximity to the electron beam. Once the cloud of atoms and singly charged ions reach the center of the drifttubes, some of them will be hit by the electron beam, thereby ionizing them by electron impact ionization. In order to elongate the time the ions spend inside the electron beam, an electrostatic axial trapping field is applied to the drifttubes. In combination with the negative space charge of the electron beam, this prohibits the ions from leaving the trap. By keeping the ions inside the trap for an extended period of time (typically 100 ms - 1 s) the ions' charge states increase in the so-called "charge-breeding time". The maximum charge state achievable depends on the ionization potentials of the ions inside the trap, the compression of the electron beam and its current, as well as the electron beam energy determined by the voltage difference between cathode and central drifttube. In order to extract the electron beam after the ionization region, the electron collector at the right side of Fig. 3.1 is set to ground potential and the ion extractors are set to a voltage that is more negative than the

cathode’s potential. Thereby, all electrons are deflected and hit the collector and no electrons can escape along the beamline axis. The collector is hollow to allow cooling water to flow through, to keep the temperature rise of the collector by electron impacts below a critical threshold. In order to extract the ions in a bunched fashion, the drifttube on the beamline-side of the central drift tube (CDT) is pulsed to ground potential after the charge breeding time, which accelerates the ions with an energy of  $U_{\text{CDT}}/q$  through the ion extractors, in the direction of the beamline. For details on the TipEBIT see [Schw 17, Schw 19].

The ions produced inside the TipEBIT are accelerated out of the trapping region with a kinetic energy of typically  $\approx 4 \text{ keV}/q$ . They are  $q/m$  or time-of-flight selected by a Bradbury Nielsen gate (BNG) [Brad 36], see Fig. 3.2. Since the flight path of the ions from the EBIT center to the BNG is only 1.45 m, a fast high-voltage switch has recently been developed in our group with rise and fall times of  $\approx 10 \text{ ns}$  and an on-time of as little as 20 ns [Schw 22]. Once the desired charge state and isotope is selected, the ions are guided towards an electrostatic bender which deflects the ions into the vertical direction, so they can fly towards the cryogenic region inside the magnet bore in the low-noise magnet laboratory.

The second ion source is a commercial EBIT by the company DREEBIT [DREE] and is mainly used for gaseous or MIVOC (Metal Ions from Volatile Compounds) sources [Koiv 98]. The HCIs are accelerated out of the charge breeding region with a kinetic energy of  $\approx 6.5 \text{ keV}/q$  towards a  $90^\circ$  bender magnet for  $q/m$  selection, see Fig. 3.2. For guidance and detection, there are several electrostatic lenses and retractable detection units mounted along the beamline. The ions in the selected charge state are bent towards the vertical beamline, using an electrostatic bender, at which point both beamlines are joined and share the remaining vertical ion-optical elements.

### 3.1.1 Double TipEBIT beamline

The TipEBIT 1 in combination with the time-of-flight beamline, see Fig. 3.2, have become the main ion source for PENTATRAN since their installation in spring 2021. This is due to the TipEBIT’s flexibility regarding the selection of sample material as well as the absence of a magnetic bender. The distortion of the ion beam by a bender magnet is difficult to compensate by electrostatic lenses and leads to higher ion losses. In addition, the TipEBIT is built very robustly and only requires a cathode change or exchange of insulator after several years of continuous use. In order to keep the flexibility of having two ion sources, e.g. no downtime during target change or in case of maintenance, part of this thesis work included building a second TipEBIT and planning a new beamline. The new beamline, see Fig. 3.3, will join the ionbeam paths from the two TipEBITs after two electrostatic lenses by the use of an electrostatic bender. This way, the already existing BNG and electrostatic bender towards the vertical beamline can be used with ions from both TipEBITs. The old DREEBIT

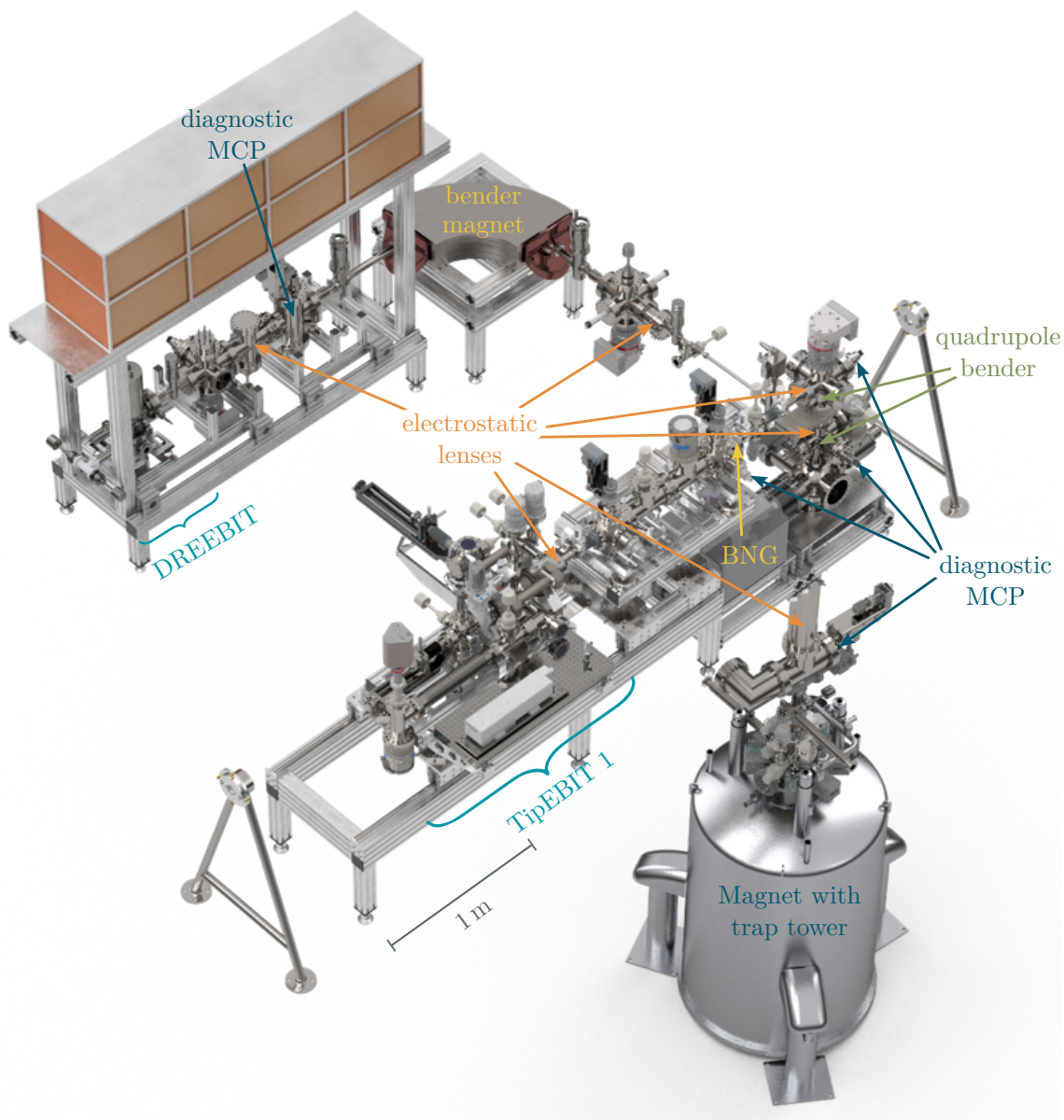


**Figure 3.2:** CAD rendering of the current PENTATRAP beamlines and ion sources up to the magnet in which the Penning-trap tower is located.

beamline is currently being dismantled and the new beamline will be assembled in the coming months.

The new TipEBIT was built and commissioned in 2022 and is already in use today. Details on the commissioning can be found in [Gram 22]. One of the new features compared to the first version is a shortened final drifttube, which is now 8.9 mm long, combined with an elongated collector, see Fig. 3.1. This change was implemented since the last drifttube was typically hit by too many electrons and we were therefore forced to set it to ground potential. The heat-up of the collector due to electron impacts leads to outgassing. This gas used to be



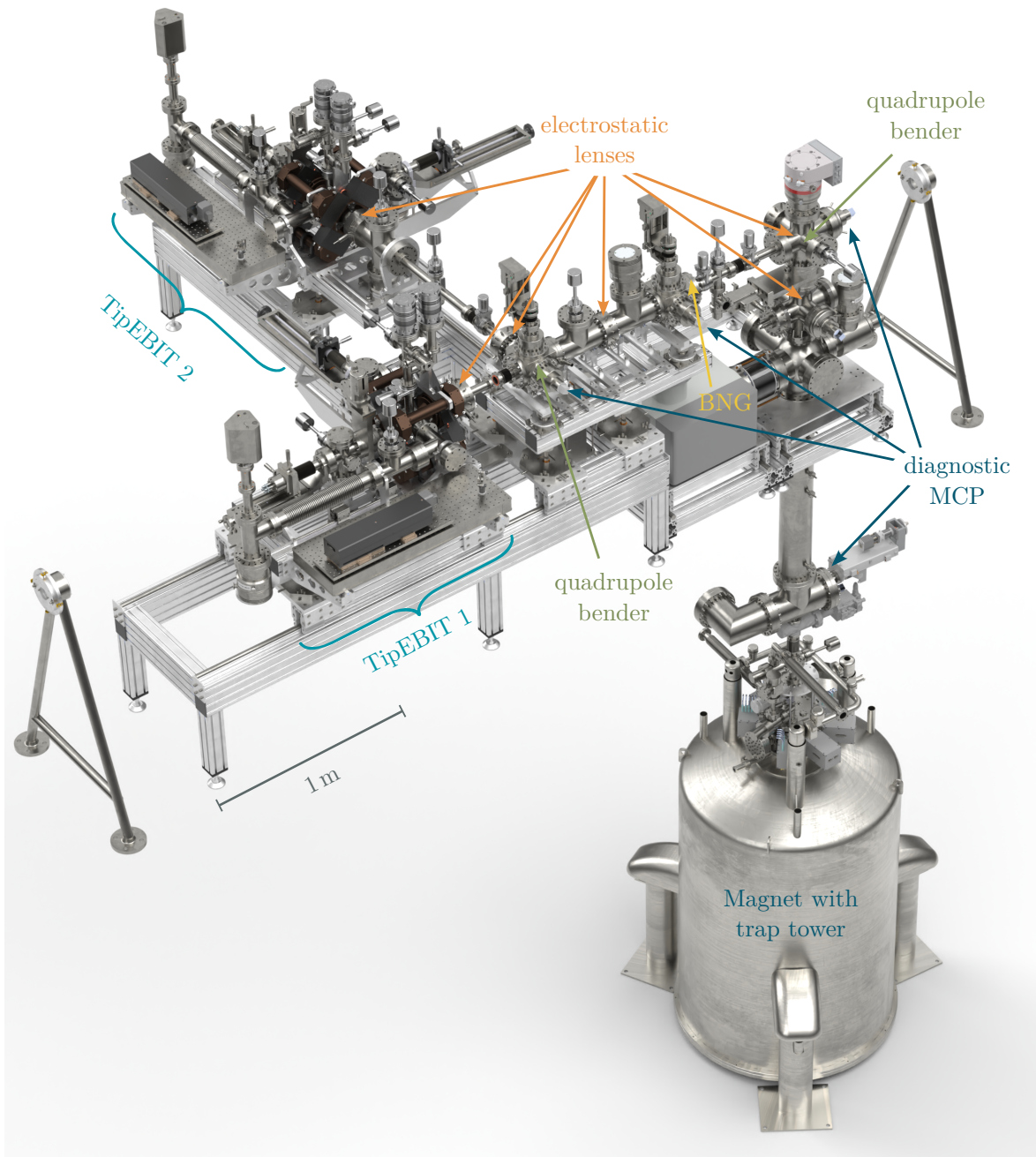


**Figure 3.3:** CAD rendering of the planned beamline adjustment and its most important parts. The two TipEBITs are connected to one time-of-flight beamline which is connected to the magnet with the Penning traps.

pumped through the narrow trap center in older versions of the TipEBIT, which resulted in a low pumping cross section. Therefore, the vacuum setup of the new TipEBIT was extended by a turbomolecular pump below the electron collector.

At the end of 2023, the old TipEBIT was taken out for repairs and the new TipEBIT was swapped into the PENTATRAN setup at the position TipEBIT 1 and has since been used

as the main ion source of PENTATRAP. Fig. 3.4 shows a time-of-flight spectrum of the new TipEBIT, measured at the end of the horizontal beamline (flight path of  $\approx 2.2$  m) with an accelerating voltage at the central drifttube of 2.545 kV. For the shorter charge breeding time of 0.7 s, there are still some lighter rest-gas ions visible, i.e. the collection of peaks of ions with charge-to-mass-number  $q/A = e/2$  with  $e$  the elementary charge. For longer charge breeding times of 1.1 s, the lighter ions are lost from the trap since the heavier argon ions rest deeper in the trapping potential of the EBIT and drive the lighter rest-gas ions out of the trapping region. Once the old TipEBIT is repaired, the double TipEBIT beamline will be assembled and tested.

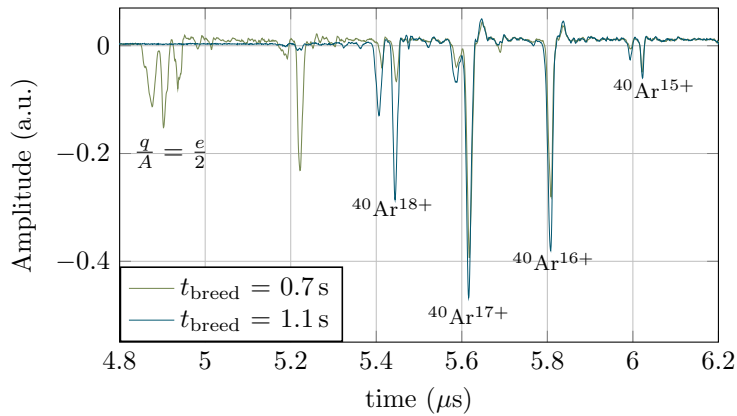


**Figure 3.4:** Time-of-flight spectrum of highly charged argon ions from the new TipEBIT that was taken with the MCP at the end of the horizontal beamline. The ions can be observed as dips in the signal of the anode behind the MCP detector plates.

### 3.2 Vertical beamline and trap tower

The ion beam of the selected ion species is guided vertically towards the cryogenic region inside the 7 T magnet with the help of electrostatic lenses and focus electrodes, see Fig. 3.5. In order to be able to stop the ions from flying through the traps, there are two pulsed drifttubes, one in the room temperature section and one in the cryogenic section, with which it is possible to lower the ions' kinetic energy from  $\approx 4$  keV/ $q$  to just a few eV/ $q$ . For the flight-path optimization, there is one last multi-channel plate (MCP) with a phosphor screen and camera mounted on a translation stage just above the magnet. Below the last MCP one can guide the ions through the traps by adjusting the lenses and foci so that the ions are guided towards the Faraday cup centered below the traps instead of hitting the ring-shaped electrode above the trap tower used as a Faraday cup. Once there are ions reaching the Faraday cup below the traps, one can try to capture ions inside the first Penning trap. This

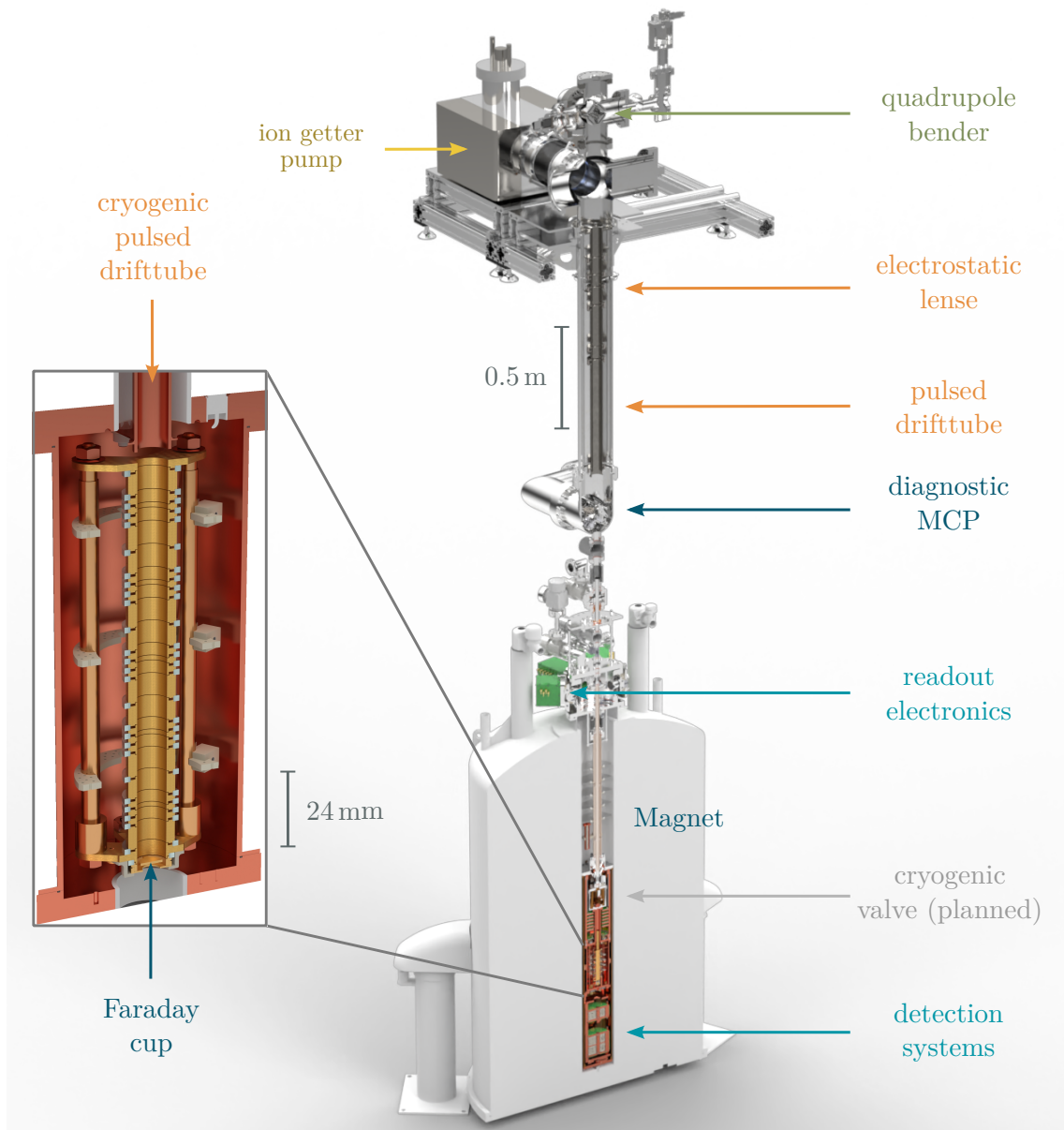


**Figure 3.5:** CAD rendering of the vertical beamline (sectional) with the Penning-trap tower. Close-up of the trap chamber with the stack of five cylindrical Penning traps made up of five electrodes each.

is possible by reflecting the ions with the lower endcap of Trap 1 (positive voltage of 20 V) and capturing them by quickly switching the cryogenic drifttube located just above the first trap to a positive voltage as well. Once trapped inside the first Penning trap, the ions are transported to the second trap which is equipped with a detection system to determine if the loading was successful (single ion) or if it was unsuccessful (no ions or several ions). The first and fourth trap are used for ion storage, Trap 2 and Trap 3 are used for measurements, and the fifth trap is currently not in use. The trap tower is depicted in the insert of Fig. 3.5.

Technically, the fourth trap could be used as a measurement trap as well since it is equipped with an axial detection system. However, since the voltage of the neighboring traps should be symmetric around each measurement trap, Trap 4 could only be used if the detection system were at the same frequency as the detection circuit of Trap 2, which is not the case. In the next generation cryogenic setup, which has already been assembled, this is planned to be changed so all three inner traps can be used as measurement traps.

# 4 Publications

This thesis was written as a cumulative dissertation in agreement with the regulations of the Department of Physics and Astronomy of the University of Heidelberg. The following chapter includes three published articles in internationally acclaimed peer-reviewed journals. The author of this thesis holds the first authorship of all three publications.

The first and second paper in [Sec. 4.1](#) and [Sec. 4.2](#) describe atomic mass determinations of lead-208 and uranium-238, respectively. The masses find their application as “backbone” masses for the Atomic Mass Evaluation (AME) [[Audi 12](#)], providing high-precision reference masses for the heavy mass region. The applied technique is a phase-sensitive cyclotron frequency measurement on a single highly charged ion in a Penning trap. The mass is determined by forming a cyclotron frequency ratio comparing the ion of interest with a highly charged reference ion with well-known mass, which was in both cases  $^{132}\text{Xe}^{26+}$ . The determination of the neutral atomic mass is completed with a theoretical determination of the binding energies of the missing electrons of both ions. While working on the paper on the uranium mass, I noticed a sign error of the image charge shift in the lead mass publication. This was corrected in form of an Erratum, which can be found in [Sec. 4.1](#) after the main publication. [Sec. 4.2](#) is completed with a Supplemental Material, describing in detail the systematic measurements and estimations for the highly precise mass-ratio measurements at PENTATRAP. This includes a measurement of the ICS to a precision of below 2%.

While the first two papers are aimed to determine precise atomic masses, in the third paper, see [Sec. 4.3](#), a mass difference between two  $^{208}\text{Pb}^{41+}$  ions is determined. This mass difference can be explained by one of the two ions being in a long-lived electronically excited state and its energy increasing the ion’s mass. The measurement of the excited state energy is accompanied by two partially different *ab initio* multi-configuration Dirac-Hartree-Fock calculations, allowing the comparison of state-of-the-art atomic structure calculations with an energy measurement without directly driving the transition of the highly charged ion.

## 4.1 High-precision mass measurement of doubly magic $^{208}\text{Pb}$

In this article the measurement of the atomic mass of lead-208 is described. The article has been published in the *European Physics Journal A*.

**Authors:** [Kathrin Kromer](#), Chunhai Lyu, Menno Door, Pavel Filianin, Zoltán Harman, Jost Herkenhoff, Wenjia Huang, Christoph H. Keitel, Daniel Lange, Yuri N. Novikov, Christoph Schweiger, Sergey Eliseev, Klaus Blaum

**Publication status:** Published 25 October 2022

**Journal reference:** Kromer *et al.* *Eur. Phys. J. A* **58**, 202 (2022)

**Digital Object Identifier:** [10.1140/epja/s10050-022-00860-1](https://doi.org/10.1140/epja/s10050-022-00860-1)

Erratum: [10.1140/epja/s10050-024-01276-9](https://doi.org/10.1140/epja/s10050-024-01276-9)

**Authors' contributions:** [KK](#), MD, PF, CS, and SE conducted the experiment and took the data. [KK](#), MD, and SE analyzed the data. CL and ZH calculated and discussed the theory. WH calculated the influence of the new mass on other nuclides. CL wrote the theory part of the manuscript. [KK](#) wrote the remaining parts: the introduction, the experimental part, analysis, and results and prepared all figures. All authors took part in the critical review of the manuscript before and after submission.

**Abstract:** The absolute atomic mass of  $^{208}\text{Pb}$  has been determined with a fractional uncertainty of  $7 \times 10^{-11}$  by measuring the cyclotron-frequency ratio  $R$  of  $^{208}\text{Pb}^{41+}$  to  $^{132}\text{Xe}^{26+}$  with the high-precision Penning-trap mass spectrometer PENTATRAP and computing the binding energies  $E_{\text{Pb}}$  and  $E_{\text{Xe}}$  of the missing 41 and 26 atomic electrons, respectively, with the *ab initio* fully relativistic multi-configuration Dirac-Hartree-Fock (MCDHF) method.  $R$  has been measured with a relative precision of  $9 \times 10^{-12}$ .  $E_{\text{Pb}}$  and  $E_{\text{Xe}}$  have been computed with an uncertainty of 9.1 eV and 2.1 eV, respectively, yielding  $207.976\,650\,571(14)$  u ( $u = 9.314\,941\,024\,2(28) \times 10^8$  eV/c<sup>2</sup>) for the  $^{208}\text{Pb}$  neutral atomic mass. This result agrees within  $1.2\sigma$  with that from the *Atomic-Mass Evaluation* (AME) 2020, while improving the precision by almost two orders of magnitude. The new mass value directly improves the mass precision of 14 nuclides in the region of  $Z = 81 - 84$  and is the most precise mass value with  $A > 200$ . Thus, the measurement establishes a new region of reference mass values which can be used e.g. for precision mass determination of transuranium nuclides, including the superheavies.



# High-precision mass measurement of doubly magic $^{208}\text{Pb}$

Kathrin Kromer<sup>1,a</sup>, Chunhai Lyu<sup>1</sup>, Menno Door<sup>1</sup>, Pavel Filianin<sup>1</sup>, Zoltán Harman<sup>1</sup>, Jost Herkenhoff<sup>1</sup>, Wenjia Huang<sup>2</sup>, Christoph H. Keitel<sup>1</sup>, Daniel Lange<sup>1,3</sup>, Yuri N. Novikov<sup>4,5</sup>, Christoph Schweiger<sup>1</sup>, Sergey Eliseev<sup>1</sup>, Klaus Blaum<sup>1</sup>

<sup>1</sup> Max-Planck-Institut für Kernphysik, 69117 Heidelberg, Germany

<sup>2</sup> Advanced Energy Science and Technology Guangdong Laboratory, Huizhou 516007, China

<sup>3</sup> Ruprecht-Karls-Universität Heidelberg, 69117 Heidelberg, Germany

<sup>4</sup> Department of Physics, St Petersburg State University, Saint Petersburg 198504, Russia

<sup>5</sup> NRC “Kurchatov Institute” Petersburg Nuclear Physics Institute, Gatchina 188300, Russia

Received: 7 June 2022 / Accepted: 12 October 2022 / Published online: 25 October 2022

© The Author(s) 2022, corrected publication 2022

Communicated by Navin Alahari

**Abstract** The absolute atomic mass of  $^{208}\text{Pb}$  has been determined with a fractional uncertainty of  $7 \times 10^{-11}$  by measuring the cyclotron-frequency ratio  $R$  of  $^{208}\text{Pb}^{41+}$  to  $^{132}\text{Xe}^{26+}$  with the high-precision Penning-trap mass spectrometer PENTATRAP and computing the binding energies  $E_{\text{Pb}}$  and  $E_{\text{Xe}}$  of the missing 41 and 26 atomic electrons, respectively, with the *ab initio* fully relativistic multi-configuration Dirac–Hartree–Fock (MCDHF) method.  $R$  has been measured with a relative precision of  $9 \times 10^{-12}$ .  $E_{\text{Pb}}$  and  $E_{\text{Xe}}$  have been computed with an uncertainty of 9.1 eV and 2.1 eV, respectively, yielding 207.976 650 571(14) u ( $u = 9.314\,941\,024\,2(28) \times 10^8$  eV/ $c^2$ ) for the  $^{208}\text{Pb}$  neutral atomic mass. This result agrees within  $1.2\sigma$  with that from the *Atomic-Mass Evaluation* (AME) 2020, while improving the precision by almost two orders of magnitude. The new mass value directly improves the mass precision of 14 nuclides in the region of  $Z = 81$ – $84$  and is the most precise mass value with  $A > 200$ . Thus, the measurement establishes a new region of reference mass values which can be used e.g. for precision mass determination of transuranium nuclides, including the superheavies.

## 1 Introduction

Heavy and superheavy nuclides beyond the doubly magic nucleus of  $^{208}\text{Pb}$  can only exist due to nuclear shell effects holding them together by counteracting the rapidly increasing Coulomb repulsion with growing proton number  $Z$  [1]. Insight into these quantum-mechanical nuclear structure effects can be derived from the masses of such nuclides. In

addition to some direct heavy mass measurements [2–5], a network of nuclear transitions and relative mass measurements, i.e. the *Atomic-Mass Evaluation* (AME), provides mass values for most heavy and superheavy nuclides by tracing them back to a few well-known masses of uranium isotopes [6]. However, no nuclide beyond  $Z = 70$  can be found whose mass is known to a relative precision of better than  $2 \times 10^{-9}$  to act as a precise reference point for these heavy elements. This directly limits the achievable precision in the heavier mass regions and can possibly lead to tensions or shifts of the relative measured masses due to their referencing to only one reference point. The limitations by mass dependent shifts can be reduced significantly once there is a reference mass with similar mass known to high precision [7]. The need for new anchor points for the AME arose during recent mass measurements with TRIGA-TRAP [5, 8] at the research reactor TRIGA in Mainz, specifically, an improved absolute mass of  $^{208}\text{Pb}$  [9]. Measuring this mass will also directly improve the masses of several Pb isotopes and other nuclides in this mass region [6].

In addition to the impact as a mass reference for other mass measurements, the mass of  $^{208}\text{Pb}$  will soon be needed when the magnetic moment, or the  $g$ -factor, of the bound electron of hydrogen-like  $^{208}\text{Pb}$  is planned to be determined by the Penning-trap experiments Alphatrap at the MPIK in Heidelberg [10] and Artemis at GSI Darmstadt [11]. This measurement could be the most stringent test of bound-state quantum electrodynamics in strong fields. The error of the mass of the nucleus, however, enters the error budget and therefore needs to be known to high precision [12]. With the results of this paper, the error of the mass of  $^{208}\text{Pb}$  will be negligible in future  $g$ -factor determinations.

<sup>a</sup> e-mail: [kathrin.kromer@mpi-hd.mpg.de](mailto:kathrin.kromer@mpi-hd.mpg.de) (corresponding author)

Based on the accurate absolute mass of  $^{132}\text{Xe}$  [13, 14], in this paper, we present a determination of the absolute atomic mass of  $^{208}\text{Pb}$  with a fractional uncertainty of  $7 \times 10^{-11}$ . This is the result of measuring the cyclotron-frequency ratio of  $^{208}\text{Pb}^{41+}$  and  $^{132}\text{Xe}^{26+}$  with the high-precision Penning-trap mass spectrometer PENTATRAP [15, 16] in combination with a computation of the binding energies of the missing 41 and 26 atomic electrons, respectively, using the *ab initio* fully relativistic multi-configuration Dirac–Hartree–Fock (MCDHF) method. The masses of  $^{132}\text{Xe}^{26+}$  and  $^{208}\text{Pb}^{41+}$  can be related to their neutral counterparts via

$$m(^{132}\text{Xe}^{26+}) = m(^{132}\text{Xe}) - 26m_e + E_{\text{Xe}}, \quad (1)$$

$$m(^{208}\text{Pb}^{41+}) = m(^{208}\text{Pb}) - 41m_e + E_{\text{Pb}}, \quad (2)$$

with  $m_e = 5.485\,799\,090\,65(16) \times 10^{-4}$  u being the electron rest mass [17] and  $m(^{132}\text{Xe}) = 131.904\,155\,086(10)$  u being the mass of a neutral  $^{132}\text{Xe}$  atom [13, 14], each has a relative accuracy of  $2.9 \times 10^{-11}$  and  $7.6 \times 10^{-11}$ , respectively.  $E_{\text{Xe}}$  and  $E_{\text{Pb}}$  are the binding-energy differences that represent the energies required to ionize the outermost 26 and 41 electrons, respectively, from neutral Xe and Pb atoms. With the mass ratio

$$R = \frac{m(^{208}\text{Pb}^{41+})}{m(^{132}\text{Xe}^{26+})} \quad (3)$$

being experimentally measured, one can improve the accuracy of the absolute mass of  $^{208}\text{Pb}$  via

$$\begin{aligned} m(^{208}\text{Pb}) &= R \left[ m(^{132}\text{Xe}) + 26m_e - E_{\text{Xe}} \right] \\ &\quad + 41m_e - E_{\text{Pb}}, \end{aligned} \quad (4)$$

based on the theoretically calculated  $E_{\text{Xe}}$  and  $E_{\text{Pb}}$ . By improving the mass of  $^{208}\text{Pb}$  the masses of other Pb isotopes and nearby elements can be improved accordingly since they are linked via decays of which the energy has been measured.

## 2 Experimental and theoretical methods

If one introduces a charged particle into a magnetic field  $B$ , it will describe a free space cyclotron motion with the frequency  $\omega_c = \frac{q}{m}B$ , with  $q/m$  being the charge-to-mass ratio. The working principle of a Penning trap is based on a strong homogeneous magnetic field in combination with an electrostatic quadrupole potential. While the electrostatic potential prevents the ion from escaping in axial direction, forcing it onto an oscillatory axial motion with frequency  $\omega_z$ , the magnetic field forces the ion in radial direction onto a circular orbit with a modified cyclotron frequency  $\omega_+$ . The

cross product of the two fields in the Lorentz equation leads to an additional slow drift around the trap center called magnetron motion with frequency  $\omega_-$ . When comparing these three Penning-trap eigenfrequencies to the movement of a free charged particle in a purely magnetic field, it holds [18]:

$$\omega_c = \sqrt{\omega_+^2 + \omega_z^2 + \omega_-^2}. \quad (5)$$

From this equation we can see that the determination of eigenfrequencies of an ion in a Penning trap can be used to determine its mass, if the magnetic field inside the trap is known. However, a determination of a magnetic field of  $B \approx 7$  T inside a volume of just a few  $10 \mu\text{m}^3$  to sufficient precision is not possible. Therefore, a relative measurement is chosen at PENTATRAP, using a reference ion and a sequential measurement scheme to determine mass ratios [15]. Highly charged ions are used due to the advantage that with higher  $q/m$  the modified cyclotron frequency increases and can therefore be measured to a higher relative precision. For each mass determination a reference nuclide and charge states have to be chosen that form a  $q/m$  doublet with the nuclide of interest in order to largely suppress systematic effects in the cyclotron-frequency ratio determination [15, 16]. The advantage being, that with  $q/m$  doublets the same trapping voltage can be used to match the axial frequency to the detection tank circuit's resonance frequency. Using the same trapping voltage reduces systematic shifts due to trap anharmonicities. In addition, the absolute mass of the reference nuclide has to be known better than the aimed uncertainty of the mass of the nuclide of interest. More technical restrictions are posed by the production of the reference ion, limited by binding energies and the availability of probe material. For these reasons, the near  $q/m$  doublet  $^{208}\text{Pb}^{41+}$  ( $q/m = 0.197\,138$  e/u) and  $^{132}\text{Xe}^{26+}$  ( $q/m = 0.197\,113$  e/u) [13, 14] was chosen. The  $^{132}\text{Xe}^{26+}$  ion was created from a gaseous natural source inside a commercial *Dresden electron beam ion trap* (DREEBIT) [19, 20]. The DREEBIT is connected to a beamline with a large bender magnet for  $q/m$  selection, see Fig. 1a upper beamline. The  $^{208}\text{Pb}^{41+}$  ion was produced in a Heidelberg Compact electron beam ion trap (compact EBIT) [21] equipped with an in-trap laser-desorption target of monoisotopic  $^{208}\text{Pb}$  [22]. After ion breeding, the  $q/m$  selection was achieved using the time-of-flight separation technique with fast high-voltage switches recently developed at the MPIK [23], supplying the voltages to a Bradbury-Nielson gate [24], see Fig. 1a lower beamline. Once the ions were selected and decelerated by two pulsed drift tubes, they were consecutively trapped in the first of PENTATRAP's five traps and transported down to their individual traps.

Due to the five stacked Penning traps available, see Fig. 1b, a simultaneous measurement in two traps is possible, increasing the measurement speed by higher statistics and offering up the opportunity for cross checks between the traps



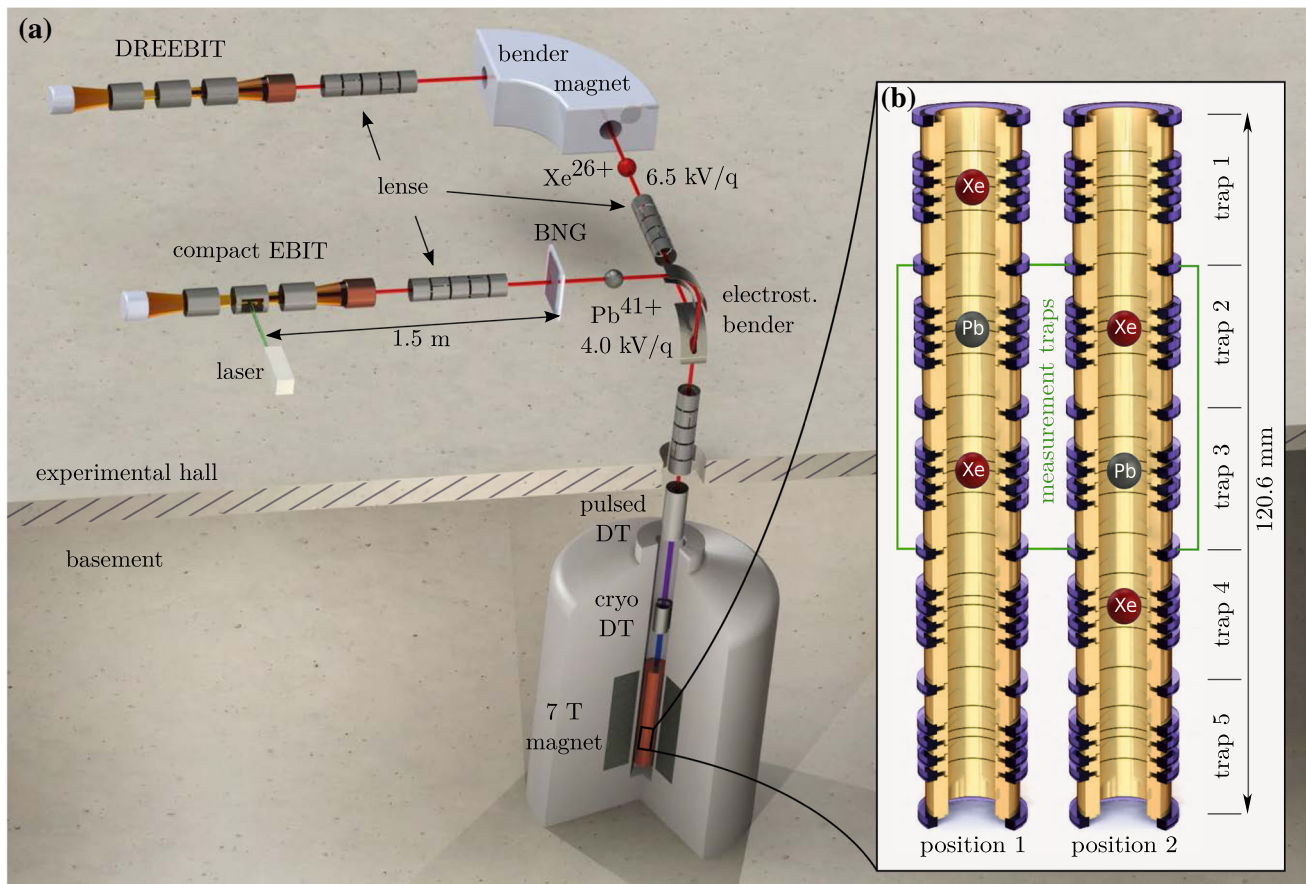


**Fig. 1** **a** Schematic illustration of the ion production section, the two beamlines, and the combined deceleration region ending in the trap chamber. The ion bunches with their respective energies are shown after they have been  $q/m$  selected by the bender magnet or the Bradbury-Nielson gate (BNG). **b** Schematic drawing of the Penning-trap tower

with two measurement ion configurations. The ions are moved from position 1–2 or back every  $\approx 15$  min. The frequency measurements are carried out in traps 2 and 3. Traps 1 and 4 are utilized as storage traps and trap 5 is currently not in use but is planned to be used to monitor magnetic field fluctuations in the future

and several analysis methods. Out of the other three traps, two are needed for ion storage and one trap is planned for monitoring, however, currently not in use.

The ion’s frequencies depend on the magnetic field and the electrostatic potential. All environmental influences on these quantities need to be stabilized over the duration of the measurement. For this, the PENTATRAP laboratory is temperature-stabilized to  $\delta T < 50$  mK/h and the height of the liquid helium level  $z_{\text{He}}$  used for cooling the superconducting magnet, Penning traps, and the detection system is stabilized to  $\delta z_{\text{He}} < 1$  mm/h along with the pressure of helium gas inside the magnet’s bore to  $\delta p < 10$   $\mu$ bar/h [15].

We employ the Fourier-transform ion-cyclotron-resonance detection technique [25] using cryogenic tank circuits connected to the Penning traps to pick up the small image current induced in the trap electrodes by the ion. The largest frequency  $\omega_+$ , and therefore the frequency with the highest contribution to the overall error, is measured using the phase-sensitive pulse and phase (PnP) method [26,27]. This

method, described in more detail below, sets an initial phase of the reduced cyclotron frequency, then the motion is left decoupled for a variable phase accumulation time  $t_{\text{acc}}$  during which the phase can evolve freely, before reading out the final phase  $\phi_{\text{meas}}$ . The other two frequencies  $\omega_z$  and  $\omega_-$  are measured with the Fast-Fourier-Transform (FFT) dip and the double-dip technique, respectively [28].

The measurements of  $^{208}\text{Pb}^{41+}$  versus  $^{132}\text{Xe}^{26+}$  were carried out with the measurement scheme shown in Fig. 2. After a rough estimate of all three frequencies of both ions in both positions, shown in Fig. 1b, using the dip and double-dip technique, the measurement run starts with an  $N$  determination, with  $N$  being the integer number of full turns of the reduced cyclotron motion during the phase accumulation time. This preparatory measurement is necessary before the actual PnP measurement because the cyclotron phase of the ion increases linearly with time with the increment of the frequency  $\omega_+$  and will thereby pass a full turn of  $2\pi$  many times during the phase accumulation time. The inte-

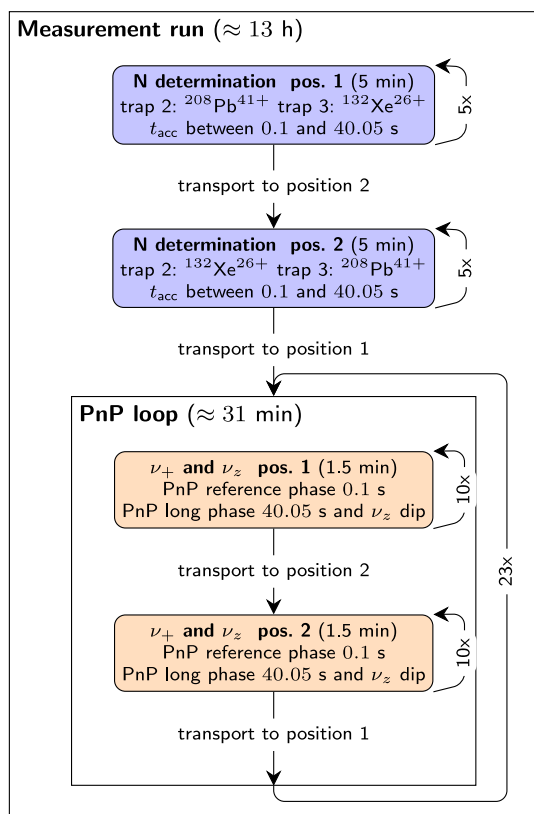


**Fig. 2** The figure depicts a flowchart of the measurement scheme and the relevant measurement times during the lead mass campaign. In blue at the top one can see the initial  $N$  determination followed by the main measurement PnP loop in orange with the simultaneous measurement of axial frequency and modified cyclotron phase. The ions are frequently swapped in order to minimize the magnetic field drift between position 1 and 2

ger  $N$  needs to be known in order to determine the modified cyclotron frequency through the total accumulated phase

$$\phi(t_{\text{acc}}) = t_{\text{acc}} \times \omega_+ = 2\pi \times N + \phi_{\text{meas}}, \quad (6)$$

with  $\phi_{\text{meas}}$  being the measured phase at the end of the accumulation time  $t_{\text{acc}}$ . The  $N$  determination utilizes 9 different phase accumulation times between 0.1 and 40.05 s and finds an  $\omega_+$  for which each  $N$  for all accumulation times is integer.

A constant phase offset, unavoidable due to the phase readout, is cancelled out by subtracting a short reference phase with an accumulation time of 0.1 s from each long measurement phase. After concluding the  $N$  determination in both traps for lead and xenon, the actual PnP loop is started, see Fig. 2 lower half. Here, a starting phase is imprinted on the modified cyclotron motion by an  $\omega_+$  dipole excitation pulse. The phase can then evolve freely for  $t_{\text{acc}}$  before the final modified cyclotron phase is imprinted on the axial motion by a coupling  $\pi$ -pulse, where it can be detected as an axial phase [26, 27]. All excitation and coupling pulses are shaped with a Tukey window [29] in order to avoid systematic phase

shifts during the phase readout. During the phase evolution time of the PnP sequence, an FFT axial-dip measurement is performed. This simultaneous phase determination and dip detection leads to a reduction of systematic effects associated with the temporal variation of the trap potential and the magnetic field, since they cancel out when calculating the free cyclotron frequency, using the invariance theorem in Eq. (5). After repeating the measurement of the two ions in trap 2 and 3 ten times, the ions are swapped. If  $^{132}\text{Xe}^{26+}$  was in the trap, then  $^{208}\text{Pb}^{41+}$  is swapped in and vice versa. This is repeated for around 12 hours before restarting the whole measurement scheme again with the  $N$  determination. The magnetron frequency, being a factor  $\approx 1,600$  smaller than the modified cyclotron frequency, does not need to be measured repeatedly since the double-dip determination during the preparation phase is sufficiently precise. After one measurement run a relative statistical uncertainty of  $\approx 10^{-11}$  is reached.

To determine a neutral mass of  $^{208}\text{Pb}$  from the ions' free cyclotron frequency ratio we need to include the mass of the missing electrons in combination with their binding energies (in the following we always refer to the absolute binding energies). We employ the *ab initio* fully relativistic multiconfiguration Dirac–Hartree–Fock (MCDHF) method [30–32] to compute the binding energies  $E_{\text{Xe}}$  and  $E_{\text{Pb}}$  of the outermost 26 and 41 electrons, respectively, in neutral Xe and Pb atoms. First, for the case of Xe, the ionization energy of the outermost 8 electrons has been experimentally determined to be of 424.7(7) eV [33]. Thus, one only needs to calculate the binding-energy difference between the ground states of  $\text{Xe}^{26+}$  ( $[\text{Ar}]3d^{10} 1S_0$ ) and  $\text{Xe}^{8+}$  ( $[\text{Kr}]4d^{10} 1S_0$ ). Similarly, since the ionization energy of the outermost 4 electrons in neutral Pb has been measured to be 96.71904(61) eV [33], only the corresponding binding-energy difference between the ground states of  $\text{Pb}^{41+}$  ( $[\text{Kr}]4d^{5} 4P_{5/2}$ ) and  $\text{Pb}^{4+}$  ( $[\text{Xe}]4f^{14} 5d^{10} 1S_0$ ) needs to be determined theoretically. In the following, we use  $E_{\text{Xe}^{08-26}}$  and  $E_{\text{Pb}^{04-41}}$  to represent these two terms.

Within the MCDHF scheme, the many-electron atomic state function (ASF) is constructed as a linear combination of configuration state functions (CSFs) with common total angular momentum ( $J$ ), magnetic ( $M$ ), and parity ( $P$ ) quantum numbers:  $|\Gamma P J M\rangle = \sum_k c_k |\gamma_k P J M\rangle$ . The CSFs  $|\gamma_k P J M\rangle$  are given as  $jj$ -coupled Slater determinants of one-electron orbitals, and  $\gamma_k$  summarizes all the information needed to fully define the CSF, i.e. the orbital occupation and coupling of single-electron angular momenta.  $\Gamma$  collectively denotes all the  $\gamma_k$  included in the representation of the ASF. The set of CSF basis is generated by the GRASP2018 code [32] via single and double (SD) excitation of electrons from the reference configurations to high-lying virtual orbitals. After solving the self-consistent MCDHF equations for the radial wavefunctions and the mixing coefficients  $c_k$ , the rel-

ativistic configuration interaction (RCI) method is applied to account for the corrections arising from the quantum electrodynamic terms and Breit interactions. We systematically expand the size of the basis set by adding and optimizing virtual orbitals layer by layer up to  $n = 10$  ( $n$  is the principle quantum number), with the final correlation energies being derived by extrapolating to  $n = \infty$ .

As the ground states of  $\text{Xe}^{26+}$  and  $\text{Xe}^{8+}$  are both in closed-shell configurations, the CSF basis sets used for the calculations can be generated by allowing SD excitations from all the core electrons starting with the  $1s$  orbitals. This gives a contribution from the SD electron correlation energy of 25.6 eV. The contributions from the Breit interactions and QED effects are 4.0 and 0.5 eV, respectively.

For the calculation of  $\text{Pb}^{41+}$ , however, due to its open  $4d^5$  configuration, the number of CSFs for  $J = 5/2$  easily grows above 4 million even for the SD exchanges of the  $4s^2 4p^6 4d^5$  electrons and becomes not tractable. Therefore, to access  $E_{\text{Pb}^{04-41}}$ , one needs to construct an ion chain in the calculation to reduce the errors. We first calculate the binding-energy difference between  $\text{Pb}^{4+}$  and  $\text{Pb}^{22+}$  via SD excitations from core electrons down to the  $3p$  subshell, and then calculate the binding-energy difference between  $\text{Pb}^{22+}$  and  $\text{Pb}^{36+}$  by allowing SD excitations of all the core electrons. Finally, the connection between  $\text{Pb}^{36+}$  and  $\text{Pb}^{41+}$  is bridged over  $\text{Pb}^{42+}$  via SD excitations from the  $4s$  orbitals. In total, the SD electron correlation effects contribute 58.1 eV to  $E_{\text{Pb}^{04-41}}$ . The Breit interactions and QED terms give rise to corrections of 9.3 and  $-0.6$  eV, respectively, to the binding energy difference.

Until now, only the SD correlation energies are included in the calculations. Considering that the uncertainties in Breit and QED terms are small, the neglected higher-order correlations will account for the systematic errors. To estimate these errors, we make use of the accurate ionization data of the outermost 8 and 4 electrons in Xe and Pb, respectively. The estimations are based on three observations. First, as a self-consistent theory, the MCDHF always approaches the real ground-state energy from above. Thus, the MCDHF binding energy of a given ionic ground state is always smaller than its real value. Second, for a given element, the contributions from higher-order correlation terms scale with the number of bound electrons. Therefore, the differences between the MCDHF binding energy and its real value is more likely to be smaller in highly charged ions. Lastly, within the same isoelectronic sequence, the contributions from higher-order correlations are always smaller for highly charged ions. This is because, perturbatively, in the denominator of each perturbation term, the energy differences between atomic states in highly charged ions are much larger than those in lower charged ions. As a result, for closed-shell ions, the calculated

binding-energy differences based on the SD excitations are always smaller than their real values, but their deviations become narrower when the charge states become larger.

For the case of Xe, we find that the calculated binding-energy difference between  $\text{Xe}^{8+}$  and Xe is 3.5 eV smaller than the experimentally measured value of 424.7(7) eV, with the single-electron ionization energies of Xe,  $\text{Xe}^{7+}$ , and  $\text{Xe}^{8+}$  being 0.32 eV, 0.22 eV and 0.10 eV, respectively, smaller than their experimental measurements. Though the deviations of the single-electron ionization energies for some open-shell ions between  $\text{Xe}^{8+}$  and  $\text{Xe}^{26+}$  may be larger than the 0.22 eV deviation of that in  $\text{Xe}^{7+}$ , one can still conservatively expect that the average deviation of the 16 electrons will not be larger than 0.22 eV. This indicates that the systematic shift of  $E_{\text{Xe}^{08-26}}$  shall be within 4.0 eV. To cover the range between 0 to 4.0 eV, one can add a systematic correction of 2.0(2.0) eV, with both systematic shift and uncertainty being 2.0 eV. This leads to  $E_{\text{Xe}^{08-26}} = 8546.5(2.0)$  eV and  $E_{\text{Xe}} = 8971.2(2.1)$  eV.

With a similar procedure, the ionization energy of  $\text{Pb}^{2+}$  and  $\text{Pb}^{3+}$  are found to be 1.26 and 0.95 eV smaller than their experimental measured values when SD excitation from the  $3p$  subshells are considered. This indicates an average deviation of  $< 1.0$  eV for the single-electron ionization energies for  $\text{Pb}^{4+}$  to  $\text{Pb}^{22+}$ , and a systematic correction of 9.0(9.0) eV to the binding energy of the corresponding 18 electrons. For the ions between  $\text{Pb}^{22+}$  and  $\text{Pb}^{41+}$ , since they are close to the isoelectronic systems of Xe ions, one can conservatively assume a  $< 0.22$  eV average deviation of the corresponding single-electron ionization energies. After the summation, we obtain  $E_{\text{Pb}^{04-41}} = 28633.9(9.1)$  eV and  $E_{\text{Pb}} = 28730.6(9.1)$  eV.

### 3 Results

After calculating the free cyclotron frequencies during each PnP loop, the interpolation method [34] is applied to calculate the frequency ratios, see Fig. 3. This method uses two consecutive cyclotron frequencies of one trap in position 1 and interpolates them to the time the cyclotron frequency of the position 2 in the same trap was measured. Then the frequency ratio of the interpolated value of position 1 and the matching value of position 2 can be formed cancelling out in first order the magnetic field drift over time. The linear drift of the magnetic field is  $\Delta B/B = -2.3 \times 10^{-10} / \text{h}$ . The impact of the non-linear drifts of the B-field was thoroughly investigated and found insignificant on the level of the achieved statistical uncertainty. The final measured ion frequency ratio is

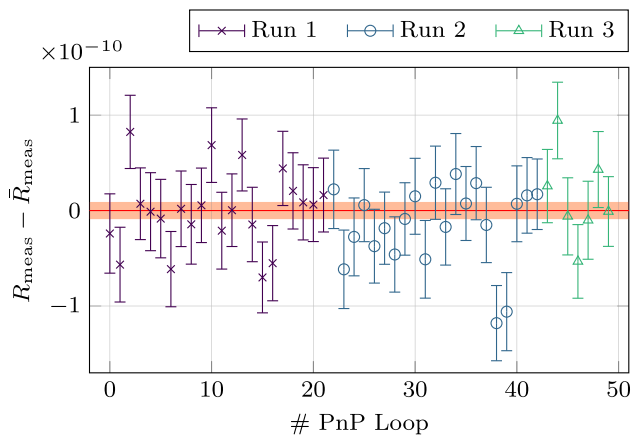


**Fig. 3** The plot shows the frequency ratios for the different PnP loops. Each color represents a different measurement run. The  $1\sigma$  error band of the averaged ratio  $\bar{R}_{\text{meas}}$  is visualized in red

**Table 1** Systematic shifts and their uncertainties on the measured modified-cyclotron frequency ratio  $R_{\text{meas}}$ . For more details see text

Effect	Correction to $R_{\text{meas}}$ ( $10^{-12}$ )	Uncertainty ( $10^{-12}$ )
Image charge shift	185	9
Relativistic shift	0	4
Total	185	10

$$\begin{aligned}
 R_{\text{meas}} - 1 &= \frac{\nu(^{208}\text{Pb}^{41+})}{\nu(^{132}\text{Xe}^{26+})} - 1 \\
 &= 1.252\,194\,24(9) \times 10^{-4}, \tag{7}
 \end{aligned}$$

with a relative statistical uncertainty of  $9 \times 10^{-12}$ .

The measured ratio is then corrected for known systematic shifts and their respective uncertainties. An overview of the relevant systematic effects and their size is listed in Table 1.

The largest systematic shift comes from the image charge shift (ICS) [35]. The highly charged ions induce an oscillating image charge in the trap electrodes. While this is necessary for detection, it causes a shift of the ions' frequencies by generating a counteracting electric field. The image charge shift depends strongly on the mass difference of the ions and on the radius of the trap, the latter being in the case of PENTATRAP 5.000(5) mm. The ICS was determined to be  $R_{\text{meas}} - \tilde{R} = \Delta(R_{\text{meas}})_{\text{ICS}} = 1.85(9) \times 10^{-10}$ , with  $\tilde{R}$  being the corrected ratio. In addition to this, the relativistic shift due to relativistic mass increase [36] leads to another systematic uncertainty related to the size of the excited radii during the PnP measurement scheme:  $\Delta(R_{\text{meas}})_{\text{rel}} = 0(4) \times 10^{-12}$ .

All other known systematic effects, due to e.g. trap potential anharmonicity, are on the order of  $10^{-13}$  and below and are therefore neglected. Thus, the final  $\omega_c$ -ratio is  $R - 1 =$

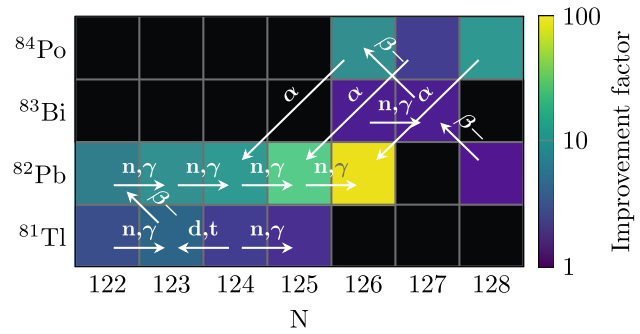


**Fig. 4** This colormap depicts a cutout of the nuclide chart. The color corresponds to the improvement factor (with 1 being no improvement) in mass precision after including the new mass value of  $^{208}\text{Pb}$  in the AME [6]. The labeled arrows show the relevant connections for the mass determination of the different nuclides via different forms of decays from which the energy is known

$1.252\,192\,39(9)(10)(13) \times 10^{-4}$ , where the number in the first, second, and third brackets indicate the statistical, systematic, and total uncertainty, respectively.

Combining the binding energies of the missing electrons calculated by theory, the experimentally determined mass ratio, and the mass excess of the reference isotope of  $^{132}\text{Xe}$  [13, 14] as listed in the AME2020, the mass excess of  $^{208}\text{Pb}$  is determined to be  $-21749.855(13)$  keV, which amounts to a neutral atomic mass of  $207.976\,650\,571(14)$  u. The new value improves the mass uncertainty of neutral  $^{208}\text{Pb}$  by a factor of 88 to a relative uncertainty of  $\delta m/m = 7 \times 10^{-11}$  and shifts the mass excess value by  $-1.4(1.1)$  keV.

#### 4 Discussion and conclusion

In addition to the improvement of precision of the mass of  $^{208}\text{Pb}$  itself, our measurement also improves the masses of a series of lead isotopes, connected by  $(n, \gamma)$  reactions. So far, their mass precision was limited by the precision of  $^{208}\text{Pb}$ , but is now limited by the precision of the energy of the  $(n, \gamma)$  reactions. Furthermore, Fig. 4 shows the improvement in precision of, in total, 14 neighbouring nuclides' masses connected to the mass of  $^{208}\text{Pb}$  via different decays, e.g.  $\alpha$  decay, for which the energy is well known. Since the new value of the mass excess of  $^{208}\text{Pb}$  is shifted downward, all these connected nuclides will be shifted down by 1.4 keV. Table 2 lists the new mass values for all nuclides which were significantly improved. With the reported measurement we have established a new region in the nuclear chart with reference masses for experiments on heavy and superheavy nuclides. When measuring masses around  $m = 200$  u the error due to the reference mass will be as low as a few  $10^{-10}$  and therefore negligible for mass determinations on radionuclides.

Furthermore, with the new mass precision of  $^{208}\text{Pb}$  of  $7 \times 10^{-11}$  the g-factor of the bound electron can be determined

**Table 2** New mass values of affected nuclides, when including the new mass value of  $^{208}\text{Pb}$  in the AME2020 [6]

Z	A	el.	$T_{1/2}$ [37]	AME2020 mass ( $\mu\text{u}$ )	Improved mass ( $\mu\text{u}$ )	Improvement factor
81	203	Tl	Stable	202,972,344.1 (1.3)	202,972,342.7 (0.4)	3.2
81	204	Tl	3.783(12) y	203,973,863.4 (1.2)	203,973,862.01 (0.26)	4.8
82	204	Pb	$1.4(6) \times 10^{17}$ y	203,973,043.5 (1.2)	203,973,042.09 (0.18)	7.0
81	205	Tl	Stable	204,974,427.3 (1.3)	204,974,425.9 (0.6)	2.4
82	205	Pb	$1.70(9) \times 10^7$ y	204,974,481.7 (1.2)	204,974,480.26 (0.13)	9.2
81	206	Tl	4.202(11) min	205,976,110.1 (1.4)	205,976,108.7 (0.7)	2.1
82	206	Pb	Stable	205,974,465.2 (1.2)	205,974,463.79 (0.12)	10.6
82	207	Pb	Stable	206,975,896.8 (1.2)	206,975,895.39 (0.06)	21.6
82	208	Pb	Stable	207,976,652.0 (1.2)	207,976,650.571 (0.014)	88.0
83	209	Bi	$2.01(8) \times 10^{19}$ y	208,980,398.6 (1.5)	208,980,397.2 (0.8)	1.8
82	210	Pb	22.20(22) y	209,984,188.4 (1.6)	209,984,187 (1.0)	1.6
83	210	Bi	5.012(5) d	209,984,120.2 (1.5)	209,984,118.9 (0.8)	1.8
84	210	Po	138.376(2) d	209,982,873.7 (1.2)	209,982,872.27 (0.14)	8.8
84	211	Po	0.516(3) s	210,986,653.2 (1.3)	210,986,651.7 (0.6)	2.4
84	212	Po	294.3(8) ns	211,988,868.0 (1.2)	211,988,866.55 (0.12)	10.1

to the same level of precision. It therefore allows to carry out the experiments on  $^{208}\text{Pb}^{81+}$  at Alphatrap and Artemis without having a large mass dependent error limiting their  $g$ -factor determination.

**Acknowledgements** This work is supported by the Max-Planck-Gesellschaft and the International Max-Planck Research School for Precision Tests of Fundamental Symmetries, the German Research Foundation (DFG) Collaborative Research Centre “SFB 1225 (ISO-QUANT)”. The project received funding from the European Research Council (ERC) under the European Union’s Horizon 2020 research and innovation programme under Grant agreement number 832848 - FunI. Furthermore, we acknowledge funding and support by the Max Planck, RIKEN, PTB Center for Time, Constants and Fundamental Symmetries.

**Funding Information** Open Access funding enabled and organized by Projekt DEAL.

**Data Availability Statement** This manuscript has no associated data or the data will not be deposited. [Authors’ comment: The datasets analysed in this study are available from the corresponding author.]

**Open Access** This article is licensed under a Creative Commons Attribution 4.0 International License, which permits use, sharing, adaptation, distribution and reproduction in any medium or format, as long as you give appropriate credit to the original author(s) and the source, provide a link to the Creative Commons licence, and indicate if changes were made. The images or other third party material in this article are included in the article’s Creative Commons licence, unless indicated otherwise in a credit line to the material. If material is not included in the article’s Creative Commons licence and your intended use is not permitted by statutory regulation or exceeds the permitted use, you will need to obtain permission directly from the copyright holder. To view a copy of this licence, visit <http://creativecommons.org/licenses/by/4.0/>.

## References

1. Y.T. Oganessian, V.K. Utyonkov, Y.V. Lobanov, F.S. Abdullin, A.N. Polyakov, R.N. Sagaidak, I.V. Shirokovsky, Y.S. Tsyganov, A.A. Voinov, G.G. Gulbekian, S.L. Bogomolov, B.N. Gikal, A.N. Mezentsev, S. Iliev, V.G. Subbotin, A.M. Sukhov, K. Subotic, V.I. Zagrebaev, G.K. Vostokin, M.G. Itkis, K.J. Moody, J.B. Patin, D.A. Shaughnessy, M.A. Stoyer, N.J. Stoyer, P.A. Wilk, J.M. Kenneally, J.H. Landrum, J.F. Wild, R.W. Loughheed, *Phys. Rev. C* **74**(4), 044602 (2006). <https://doi.org/10.1103/PhysRevC.74.044602>
2. M. Block, D. Ackermann, K. Blaum, C. Droese, M. Dworschak, S. Eliseev, T. Fleckenstein, E. Haettner, F. Herfurth, F.P. Heßberger, S. Hofmann, J. Ketelaer, J. Ketter, H.J. Kluge, G. Marx, M. Mazzocco, Y.N. Novikov, W.R. Plaß, A. Popeko, S. Rahaman, D. Rodríguez, C. Scheidenberger, L. Schweikhard, P.G. Thirolf, G.K. Vorobyev, C. Weber, *Nature* **463**(7282), 785 (2010). <https://doi.org/10.1038/nature08774>
3. M. Dworschak, M. Block, D. Ackermann, G. Audi, K. Blaum, C. Droese, S. Eliseev, T. Fleckenstein, E. Haettner, F. Herfurth, F.P. Heßberger, S. Hofmann, J. Ketelaer, J. Ketter, H.J. Kluge, G. Marx, M. Mazzocco, Y.N. Novikov, W.R. Plaß, A. Popeko, S. Rahaman, D. Rodríguez, C. Scheidenberger, L. Schweikhard, P.G. Thirolf, G.K. Vorobyev, M. Wang, C. Weber, *Phys. Rev. C* **81**(6), 064312 (2010). <https://doi.org/10.1103/PhysRevC.81.064312>
4. E.M. Ramirez, D. Ackermann, K. Blaum, M. Block, C. Droese, C.E. Düllmann, M. Dworschak, M. Eibach, S. Eliseev, E. Haettner, F. Herfurth, F.P. Heßberger, S. Hofmann, J. Ketelaer, G. Marx, M. Mazzocco, D. Nesterenko, Y.N. Novikov, W.R. Plaß, D. Rodríguez, C. Scheidenberger, L. Schweikhard, P.G. Thirolf, C. Weber, *Science* **337**(6099), 1207 (2012). <https://doi.org/10.1126/science.1225636>
5. M. Eibach, T. Beyer, K. Blaum, M. Block, C.E. Düllmann, K. Eberhardt, J. Grund, S. Nagy, H. Nitsche, W. Nörtershäuser, D. Renisch, K.P. Rykaczewski, F. Schneider, C. Smorra, J. Vieten, M. Wang, K. Wendt, *Phys. Rev. C* **89**(6), 064318 (2014). <https://doi.org/10.1103/PhysRevC.89.064318>
6. M. Wang, W.J. Huang, F.G. Kondev, G. Audi, S. Naimi, *Chin. Phys. C* **45**(3), 030003 (2021). <https://doi.org/10.1088/1674-1137/abddaf>

7. A. Kellerbauer, K. Blaum, G. Bollen, F. Herfurth, H.J. Kluge, M. Kuckein, E. Sauvan, C. Scheidenberger, L. Schweikhard, *Eur. Phys. J. D* **22**(1), 53 (2003). <https://doi.org/10.1140/epjd/e2002-00222-0>
8. J. Ketelaer, J. Krämer, D. Beck, K. Blaum, M. Block, K. Eberhardt, G. Eitel, R. Ferrer, C. Geppert, S. George, F. Herfurth, J. Ketter, S. Nagy, D. Neidherr, R. Neugart, W. Nörtershäuser, J. Repp, C. Smorra, N. Trautmann, C. Weber, *Nuclear instruments and methods in physics research section a: accelerators. Spectromet. Detect. Assoc. Equip.* **594**(2), 162 (2008). <https://doi.org/10.1016/j.nima.2008.06.023>
9. J. Grund, M. Asai, K. Blaum, M. Block, S. Chenmarev, C.E. Düllmann, K. Eberhardt, S. Lohse, Y. Nagame, S. Nagy, P. Naubereit, J.J.W. van de Laar, F. Schneider, T.K. Sato, N. Sato, D. Simonovski, K. Tsukada, K. Wendt, *Nuclear instruments and methods in physics research section a: accelerators. Spectromet. Detect. Assoc. Equip.* **972**, 164013 (2020). <https://doi.org/10.1016/j.nima.2020.164013>
10. S. Sturm, F. Köhler, J. Zatorski, A. Wagner, Z. Harman, G. Werth, W. Quint, C.H. Keitel, K. Blaum, *Nature* **506**(7489), 467 (2014). <https://doi.org/10.1038/nature13026>
11. M. Vogel, M.S. Ebrahimi, Z. Guo, A. Khodaparast, G. Birkl, W. Quint, *Annalen der Physik* **531**(5), 1800211 (2019). <https://doi.org/10.1002/andp.201800211>
12. F. Köhler, K. Blaum, M. Block, S. Chenmarev, S. Eliseev, D.A. Glazov, M. Goncharov, J. Hou, A. Kracke, D.A. Nesterenko, Y.N. Novikov, W. Quint, E. Minaya Ramirez, V.M. Shabaev, S. Sturm, A.V. Volotka, G. Werth, *Nat. Commun.* **7**(1), 10246 (2016). <https://doi.org/10.1038/ncomms10246>
13. M. Redshaw, B.J. Mount, E.G. Myers, *Phys. Rev. A* **79**(1), 012506 (2009)
14. A. Rischka, H. Cakir, M. Door, P. Filianin, Z. Harman, W.J. Huang, P. Indelicato, C.H. Keitel, C.M. König, K. Kromer, M. Müller, Y.N. Novikov, R.X. Schüssler, C. Schweiger, S. Eliseev, K. Blaum, *Phys. Rev. Lett.* **124**(11), 113001 (2020). <https://doi.org/10.1103/PhysRevLett.124.113001>
15. J. Repp, C. Böhm, J.R. Crespo López-Urrutia, A. Dörr, S. Eliseev, S. George, M. Goncharov, Y.N. Novikov, C. Roux, S. Sturm, S. Ulmer, K. Blaum, *Appl. Phys. B* **107**(4), 983 (2012). <https://doi.org/10.1007/s00340-011-4823-6>
16. C. Roux, C. Böhm, A. Dörr, S. Eliseev, S. George, M. Goncharov, Y.N. Novikov, J. Repp, S. Sturm, S. Ulmer, K. Blaum, *Appl. Phys. B* **107**(4), 997 (2012). <https://doi.org/10.1007/s00340-011-4825-4>
17. J. Zatorski, B. Sikora, S.G. Karshenboim, S. Sturm, F. Köhler-Langes, K. Blaum, C.H. Keitel, Z. Harman, *Phys. Rev. A* **96**(1), 012502 (2017). <https://doi.org/10.1103/PhysRevA.96.012502>
18. L.S. Brown, G. Gabrielse, *Phys. Rev. A* **25**(4), 2423 (1982). <https://doi.org/10.1103/PhysRevA.25.2423>
19. V.P. Ovsyannikov, G. Zschornack, *Rev. Sci. Instrum.* **70**(6), 2646 (1999). <https://doi.org/10.1063/1.1149822>
20. Startseite » DREEBIT GmbH - DREEBIT Company | DE. <https://www.dreebit.com/de/>
21. P. Micke, S. Kühn, L. Buchauer, J.R. Harries, T.M. Bücking, K. Blaum, A. Cieluch, A. Egl, D. Hollain, S. Kraemer, T. Pfeifer, P.O. Schmidt, R.X. Schüssler, C. Schweiger, T. Stöhlker, S. Sturm, R.N. Wolf, S. Bernitt, J.R. Crespo López-Urrutia, *Rev. Sci. Instrum.* **89**(6), 063109 (2018). <https://doi.org/10.1063/1.5026961>
22. C. Schweiger, C.M. König, J.R. Crespo López-Urrutia, M. Door, H. Dorrer, C.E. Düllmann, S. Eliseev, P. Filianin, W. Huang, K. Kromer, P. Micke, M. Müller, D. Renisch, A. Rischka, R.X. Schüssler, K. Blaum, *Rev. Sci. Instrum.* **90**(12), 123201 (2019). <https://doi.org/10.1063/1.5128331>
23. C. Schweiger, et al., in preparation (2021)
24. N.E. Bradbury, R.A. Nielsen, *Phys. Rev.* **49**(5), 388 (1936). <https://doi.org/10.1103/PhysRev.49.388>
25. A.G. Marshall, C.L. Hendrickson, G.S. Jackson, *Mass Spectrom. Rev.* **17**(1), 1 (1998). [https://doi.org/10.1002/\(SICI\)1098-2787\(1998\)17:1<1::AID-MAS1>3.0.CO;2-K](https://doi.org/10.1002/(SICI)1098-2787(1998)17:1<1::AID-MAS1>3.0.CO;2-K)
26. E.A. Cornell, R.M. Weisskoff, K.R. Boyce, R.W. Flanagan, G.P. Lafyatis, D.E. Pritchard, *Phys. Rev. Lett.* **63**(16), 1674 (1989). <https://doi.org/10.1103/PhysRevLett.63.1674>
27. E.A. Cornell, R.M. Weisskoff, K.R. Boyce, D.E. Pritchard, *Phys. Rev. A* **41**(1), 312 (1990). <https://doi.org/10.1103/PhysRevA.41.312>
28. X. Feng, M. Charlton, M. Holzscheiter, R.A. Lewis, Y. Yamazaki, *J. Appl. Phys.* **79**(1), 8 (1996). <https://doi.org/10.1063/1.360947>
29. F. Harris, *Proc. IEEE* **66**(1), 51 (1978). <https://doi.org/10.1109/PROC.1978.10837>
30. I.P. Grant, *Adv. Phys.* **19**, 747 (1970)
31. J.P. Desclaux, D.F. Mayers, F. O'Brien, *J. Phys. B* **4**, 631 (1971)
32. C.F. Fischer, G. Gaigalas, P. Jönsson, J. Bieroń, *Comput. Phys. Commun.* **237**, 184 (2019)
33. A. Kramida, Yu. Ralchenko, J. Reader, and NIST ASD Team. NIST Atomic Spectra Database (ver. 5.8), [Online]. Available: <https://physics.nist.gov/asd> [2021, August 11]. National Institute of Standards and Technology, Gaithersburg, MD (2020)
34. M. Door, et al., in preparation (2021)
35. M. Schuh, F. Heiße, T. Eronen, J. Ketter, F. Köhler-Langes, S. Rau, T. Segal, W. Quint, S. Sturm, K. Blaum, *Phys. Rev. A* **100**(2), 023411 (2019). <https://doi.org/10.1103/PhysRevA.100.023411>
36. L.S. Brown, G. Gabrielse, *Rev. Mod. Phys.* **58**(1), 233 (1986). <https://doi.org/10.1103/RevModPhys.58.233>
37. IAEA Nuclear Data Services. <https://www.nds.iaea.org/>



## Erratum to: High-precision mass measurement of doubly magic $^{208}\text{Pb}$

Kathrin Kromer<sup>1,a</sup>, Chunhai Lyu<sup>1</sup>, Menno Door<sup>1</sup>, Pavel Filianin<sup>1</sup>, Zoltán Harman<sup>1</sup>, Jost Herkenhoff<sup>1</sup>, Wenjia Huang<sup>2</sup>, Christoph H. Keitel<sup>1</sup>, Daniel Lange<sup>1,3</sup>, Yuri N. Novikov<sup>4,5</sup>, Christoph Schweiger<sup>1</sup>, Sergey Eliseev<sup>1</sup>, Klaus Blaum<sup>1</sup>

<sup>1</sup> Max-Planck-Institut für Kernphysik, 69117 Heidelberg, Germany

<sup>2</sup> Advanced Energy Science and Technology Guangdong Laboratory, Huizhou 516007, China

<sup>3</sup> Ruprecht-Karls-Universität Heidelberg, 69117 Heidelberg, Germany

<sup>4</sup> Department of Physics, St Petersburg State University, Saint Petersburg 198504, Russia

<sup>5</sup> NRC “Kurchatov Institute”-Petersburg Nuclear Physics Institute, Gatchina 188300, Russia

Received: 17 January 2024 / Accepted: 19 February 2024

© The Author(s), under exclusive licence to Società Italiana di Fisica and Springer-Verlag GmbH Germany, part of Springer Nature 2024

Communicated by Navin Alahari

**Erratum to: Eur. Phys. J. A (2022) 58:202**  
<https://doi.org/10.1140/epja/s10050-022-00860-1>

We found that the image charge shift (ICS) had an incorrect sign in the original paper. It should have been negative:  $R_{\text{meas}} - \tilde{R} = \Delta(R_{\text{meas}})_{\text{ICS}} = -1.85(9) \times 10^{-10}$ . This shifts the final mass value as well as the masses of the connected isotopes see Table 1. With the correct sign of the ICS, the systematically corrected cyclotron frequency ratio is:  $R - 1 = 1.252\,196\,10(9)(10)(13) \times 10^{-4}$ , where the number in the first, second, and third brackets indicate the statistical, systematic, and total uncertainty, respectively. This value is shifted by  $3.7 \times 10^{-10}$  in comparison to the original publication. As a result, the final atomic mass value of  $^{208}\text{Pb}$  is shifted by  $0.077\,\mu\text{u}$  to

$$m(^{208}\text{Pb}) = 207.976\,650\,494(14)\,\text{u}, \quad (1)$$

and the correct mass excess should be shifted by  $71\,\text{eV}$  in comparison to the originally published value and amounts to  $-21,749.927(13)\,\text{keV}$ .

Moreover, in the original paper,  $R$  was defined as the mass ratio. However, the value given later in the paper is the ratio

of the cyclotron frequencies of the ions. To be consistent, we now change the definition of  $R$  in Eq. (3) of the original paper to be the ratio of cyclotron frequencies:

$$R = \frac{\omega_c(^{208}\text{Pb}^{41+})}{\omega_c(^{132}\text{Xe}^{26+})}. \quad (2)$$

In consequence, Eq. (4) should be changed as well

$$m(^{208}\text{Pb}) = \frac{41}{26R} m(^{132}\text{Xe}^{26+}) + 41m_e - E_{\text{Pb}}. \quad (3)$$

Furthermore, the  $q/m$  ratios given in the original publication were calculated using the atomic mass of the nuclides instead of the ionic mass. The correct ratios should be:  $^{208}\text{Pb}^{41+}$ :  $q/m = 0.197\,159\,e/\text{u}$  and  $^{132}\text{Xe}^{26+}$ :  $q/m = 0.197\,134\,e/\text{u}$ . These values were not used in the analysis and therefore have no further impact on the results.

Lastly, in the original publication, there was an incorrect citation for the experiment Alphatrap at the MPIK in Heidelberg. The correct citation should have been [3].

**Open Access** This article is licensed under a Creative Commons Attribution 4.0 International License, which permits use, sharing, adaptation, distribution and reproduction in any medium or format, as long as you give appropriate credit to the original author(s) and the source, provide a link to the Creative Commons licence, and indicate if changes were made. The images or other third party material in this article are included in the article's Creative Commons licence, unless indicated otherwise in a credit line to the material. If material is not included in the article's Creative Commons licence and your intended use is not permitted by statutory regulation or exceeds the permitted use, you will need to obtain permission directly from the copyright holder. To view a copy of this licence, visit <http://creativecommons.org/licenses/by/4.0/>.

The original article can be found online at <https://doi.org/10.1140/epja/s10050-022-00860-1>.

<sup>a</sup> e-mail: [kathrin.kromer@mpi-hd.mpg.de](mailto:kathrin.kromer@mpi-hd.mpg.de) (corresponding author)

**Table 1** New mass values of affected nuclides, when including the new mass value of this erratum of  $^{208}\text{Pb}$  in the AME2020 [1]

Z	A	el.	$T_{1/2}$ [2]	AME2020 mass ( $\mu\text{u}$ )		Mass value this erratum ( $\mu\text{u}$ )	
81	203	Tl	Stable	202,972,344.1	(1.3)	202,972,342.5	(0.4)
81	204	Tl	3.783(12) y	203,973,863.4	(1.2)	203,973,861.88	(0.26)
82	204	Pb	$1.4(6) \times 10^{17}$ y	203,973,043.5	(1.2)	203,973,041.98	(0.18)
81	205	Tl	Stable	204,974,427.3	(1.3)	204,974,425.7	(0.5)
82	205	Pb	$1.70(9) \times 10^7$ y	204,974,481.7	(1.2)	204,974,480.17	(0.13)
81	206	Tl	4.202(11) min	205,976,110.1	(1.4)	205,976,108.5	(0.7)
82	206	Pb	Stable	205,974,465.2	(1.2)	205,974,463.70	(0.12)
82	207	Pb	Stable	206,975,896.8	(1.2)	206,975,895.31	(0.06)
82	208	Pb	Stable	207,976,652.0	(1.2)	207,976,650.494	(0.014)
83	209	Bi	$2.01(8) \times 10^{19}$ y	208,980,398.6	(1.5)	208,980,396.9	(0.7)
82	210	Pb	22.20(22) y	209,984,188.4	(1.6)	209,984,186.7	(0.9)
83	210	Bi	5.012(5) d	209,984,120.2	(1.5)	209,984,118.6	(0.7)
84	210	Po	138.376(2) d	209,982,873.7	(1.2)	209,982,872.17	(0.14)
84	211	Po	0.516(3) s	210,986,653.2	(1.3)	210,986,651.7	(0.6)
84	212	Po	294.3(8) ns	211,988,868.0	(1.2)	211,988,866.48	(0.12)

## References

1. M. Wang, W.J. Huang, F.G. Kondev, G. Audi, S. Naimi, Chin. Phys. C **45**(3), 030003 (2021). <https://doi.org/10.1088/1674-1137/abddaf>
2. IAEA Nuclear Data Services. <https://www-nds.iaea.org/>
3. S. Sturm, I. Arapoglou, A. Egl, M. Höcker, S. Kraemer, T. Sailer, B. Tu, A. Weigel, R. Wolf, J.C. López-Urrutia, K. Blaum, Eur. Phys. J. Spec. Top. **227**(13), 1425 (2019). <https://doi.org/10.1140/epjst/e2018-800225-2>



## 4.2 Atomic mass determination of uranium-238

In this letter the mass measurement of the atomic mass of uranium-238 is described. The article has been published in *Physical Review C*.

**Authors:** [Kathrin Kromer](#), Chunhai Lyu, Jacek Bieroń, Menno Door, Lucia Enzmann, Pavel Filianin, Gediminas Gaigalas, Zoltán Harman, Jost Herkenhoff, Wenjia Huang, Christoph H. Keitel, Sergey Eliseev, and Klaus Blaum

**Publication status:** Published 06 February 2024











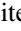


**Journal reference:** Kromer *et al.* *Phys. Rev. C* **109**, L021301

**Digital Object Identifier:** [10.1103/PhysRevC.109.L021301](https://doi.org/10.1103/PhysRevC.109.L021301)

**Authors' contributions:** [KK](#), MD, LE, PF, JH, and SE conducted the experiment and took the data. [KK](#), MD, LE, and SE analyzed the data. JB, GG, and CL worked on the code for the theoretical binding energies. CL and ZH calculated and discussed the theory. WH calculated the influence of the new mass on other nuclides. CL wrote the theory part of the manuscript and of the Supplemental Material. [KK](#) wrote the remaining parts: the introduction, the experimental part, analysis, results and the systematics part of the Supplemental Material and prepared all figures. All authors took part in the critical review of the manuscript before and after submission.

**Abstract:** The atomic mass of uranium-238 has been determined to be  $238.050\,787\,618(15)$  u, improving the literature uncertainty by two orders of magnitude. It is obtained from a measurement of the mass ratio of  $^{238}\text{U}^{47+}$  and  $^{132}\text{Xe}^{26+}$  ions with an uncertainty of  $3.5 \times 10^{-12}$ . The measurement was carried out with the Penning-trap mass spectrometer PENTATRAP and was accompanied by a calculation of the binding energies  $E_{\text{U}}$  and  $E_{\text{Xe}}$  of the 47 and 26 missing electrons of the two highly charged ions, respectively. These binding energies were determined using an *ab initio* multiconfiguration Dirac–Hartree–Fock (MCDHF) method to be  $E_{\text{U}} = 39\,927(10)$  eV and  $E_{\text{Xe}} = 8\,971.2(21)$  eV. The new mass value will serve as a reference for high-precision mass measurements in the heavy mass region of the nuclear chart up to transuranium nuclides.

**Atomic mass determination of uranium-238**

Kathrin Kromer <sup>1,\*</sup>, Chunhai Lyu <sup>1</sup>, Jacek Bieroń <sup>2</sup>, Menno Door <sup>1</sup>, Lucia Enzmann <sup>1,3</sup>, Pavel Filianin <sup>1</sup>,  
Gediminas Gaigalas <sup>4</sup>, Zoltán Harman <sup>1</sup>, Jost Herkenhoff <sup>1</sup>, Wenjia Huang <sup>5</sup>, Christoph H. Keitel <sup>1</sup>,  
Sergey Eliseev <sup>1</sup> and Klaus Blaum <sup>1</sup>

<sup>1</sup>Max-Planck-Institut für Kernphysik, 69117 Heidelberg, Germany

<sup>2</sup>Institute of Theoretical Physics, Jagiellonian University, 30-348 Kraków, Poland

<sup>3</sup>Ruprecht-Karls-Universität Heidelberg, 69117 Heidelberg, Germany

<sup>4</sup>Institute of Theoretical Physics and Astronomy, Vilnius University, 10222 Vilnius, Lithuania

<sup>5</sup>Advanced Energy Science and Technology Guangdong Laboratory, Huizhou 516007, China



(Received 27 November 2023; accepted 8 January 2024; published 6 February 2024)

The atomic mass of uranium-238 has been determined to be  $238.050\,787\,618(15)$  u, improving the literature uncertainty by two orders of magnitude. It is obtained from a measurement of the mass ratio of  $^{238}\text{U}^{47+}$  and  $^{132}\text{Xe}^{26+}$  ions with an uncertainty of  $3.5 \times 10^{-12}$ . The measurement was carried out with the Penning-trap mass spectrometer PENTATRAP and was accompanied by a calculation of the binding energies  $E_{\text{U}}$  and  $E_{\text{Xe}}$  of the 47 and 26 missing electrons of the two highly charged ions, respectively. These binding energies were determined using an *ab initio* multiconfiguration Dirac-Hartree-Fock method to be  $E_{\text{U}} = 39\,927(10)$  eV and  $E_{\text{Xe}} = 8\,971.2(21)$  eV. The new mass value will serve as a reference for high-precision mass measurements in the heavy mass region of the nuclear chart up to transuranium nuclides.

DOI: [10.1103/PhysRevC.109.L021301](https://doi.org/10.1103/PhysRevC.109.L021301)

Understanding the nuclear structure of heavy and super-heavy elements provides clues about the mechanisms involved in synthesizing them and the reasons for their finite lifetimes [1,2]. Facilities measuring the masses of actinides and transactinides contribute to our understanding of the nuclear structure by examining binding energies and derivative values such as nucleon pairing strengths, two-nucleon separation energies, and shell gap parameters [3]. This experimental data benchmarks nuclear models which are essential for predicting properties of nuclides not accessible through experiments. It is imperative to test these models in regions where experimental data are becoming available, such as the region of the  $N = 152$  subshell [4], to predict the next “doubly magic” nuclei after  $^{208}\text{Pb}$  or the center and extent of the “island of stability” [5,6].

For high-precision mass measurements, Penning-trap mass spectrometry (PTMS) has nowadays become one of the leading methods of choice. PTMS now routinely achieves relative mass uncertainties in the range of  $10^{-11}$  on stable or long-lived species [7–9] and in the range of  $10^{-9}$  on radionuclides [10–12]. Ideally, carbon-12 is used as the reference mass, since the unified atomic mass unit  $u$  is defined

as  $1/12$  of the mass of carbon-12 in its ground state. However, in reality it is often favorable to measure against a reference nuclide similar in mass to the nuclide of interest, so that many systematic uncertainties can be minimized. It is therefore desirable to have a network of nuclides with well-known masses that covers a wide mass range. The most precisely measured nuclides are sometimes referred to as the “mass backbone” [13,14]. This mass backbone and other known masses are evaluated in form of the Atomic Mass Evaluation (AME) [15], which considers all kinds of connections, from inertial to energy measurements.

The heavy mass region beyond uranium relies heavily on measurements relating them to the mass of a few uranium isotopes, whose masses are currently known to a precision of at best  $5 \times 10^{-9}$  [15]. In order to further research into nuclear structure, it is imperative to surpass this precision to benchmark advanced nuclear models. To overcome the limitation set by the reference, we have performed an ultraprecise mass measurement on uranium-238, thereby providing a significantly improved reference mass in the heavy mass region above lead, which contributes to the AME mass backbone.

In addition to serving as a reliable mass reference, an improved atomic mass value of uranium-238 is also needed for the planned investigation of the magnetic moment, and with it the  $g$ -factor of the bound-electron of hydrogenlike uranium at the experiment ALPHATRAP [16,17]. Electron  $g$  factors of heavy, highly charged ions provide stringent tests of bound-state quantum electrodynamics (QED) in strong fields as the size of the QED contribution to the  $g$  factor increases with the proton number  $Z$  [18]. However, the precision of a

\*Corresponding author: [kromer@mpi-hd.mpg.de](mailto:kromer@mpi-hd.mpg.de)

Published by the American Physical Society under the terms of the [Creative Commons Attribution 4.0 International](https://creativecommons.org/licenses/by/4.0/) license. Further distribution of this work must maintain attribution to the author(s) and the published article’s title, journal citation, and DOI. Open access publication funded by the Max Planck Society.

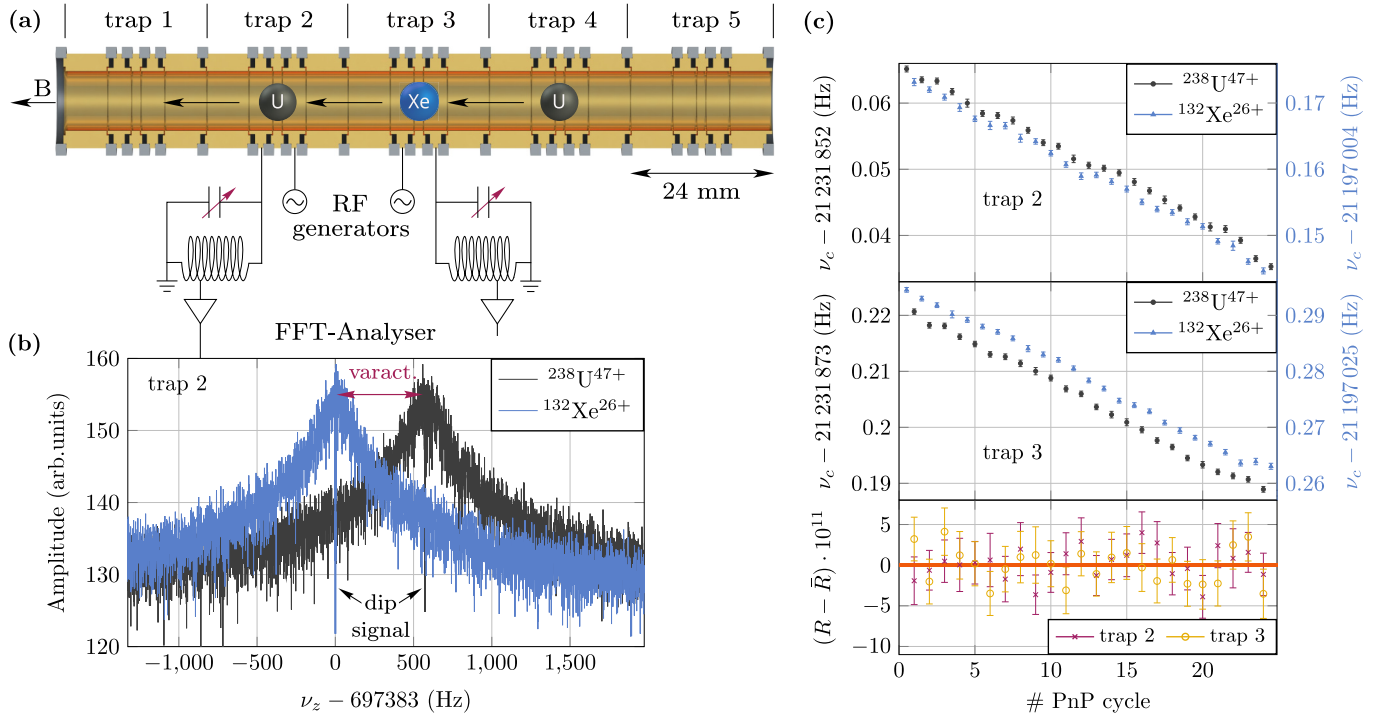


FIG. 1. (a) Sectional view of the Penning-trap tower with three ions in configuration 1. Configuration 2 is indicated by arrows. (b) Axial spectrum of trap 2 showing an overlay of a resonator with dip signal of the Xe ion and of the U ion at their respectively different resonator frequencies varied by the varactor. (c) Exemplary measurement run showing the determined cyclotron frequencies of both ions (y axis of the xenon ion is on the right in blue) and the ratios that can be formed by interpolation in time of the cyclotron frequencies (lower panel).

$g$ -factor measurement is directly limited by the knowledge of the mass of the ion of interest. In order to achieve a determination of the electron  $g$  factor with a precision on the level of  $10^{-9}$ , the mass of the ion has to be known to the same precision.

In this Letter, we will combine a Penning-trap mass ratio measurement and *ab initio* multiconfiguration Dirac-Hartree-Fock (MCDHF) binding-energy calculations to determine the atomic mass of uranium-238.

A determination of the mass of an ion  $m$  with charge  $q$  in a Penning trap is based on the measurement of the free cyclotron frequency  $\nu_c = qB/(2\pi m)$  of the ion in a static homogeneous magnetic field  $B$ . In order to confine the particle's motion in all three dimensions, a Penning trap is composed of an electrostatic quadrupolar field in addition to the magnetic field. The combination of both fields forces the ion on a trajectory consisting of three independent eigenmotions (small to large in order of the size of the eigenfrequency): the magnetron motion with frequency  $\nu_-$ , the axial motion with frequency  $\nu_z$ , and the modified cyclotron motion with frequency  $\nu_+$ . In order to obtain the free cyclotron frequency, the relation

$$\nu_c^2 = \nu_-^2 + \nu_z^2 + \nu_+^2 \quad (1)$$

can be used [19]. Since the magnetic field is not known precisely enough, one measures the cyclotron frequency of the ion of interest (subscripted ioi) with respect to the cyclotron frequency of a reference ion (subscripted ref) with well-known mass  $m_{\text{ref}}$  [15]. The measured ratio  $R$  of the cyclotron frequencies is just proportional to the ratio of the

ions' masses, since the magnetic field cancels to first order:

$$R = \frac{\nu_{c,\text{ioi}}}{\nu_{c,\text{ref}}} = \frac{m_{\text{ref}} q_{\text{ioi}}}{m_{\text{ioi}} q_{\text{ref}}}. \quad (2)$$

Usually, systematic effects increase with a larger mass difference, however, most systematic effects stemming from various trap imperfections and  $B$ -field inhomogeneities are minimized when using a similar charge-to-mass ( $q/m$ ) ratio of the ion of interest and the reference ion. For this reason, mass measurements at PENTATRAP are carried out on a broad range of ion masses and charge states with the flexibility of choosing any reference ion that is most suited for each specific measurement [20,21]. For the determination of the absolute mass of uranium-238, the near  $q/m$  doublet  $^{238}\text{U}^{47+}$  and  $^{132}\text{Xe}^{26+}$  was chosen with a difference in  $q/m$  of  $3.24 \times 10^{-4} e/u$ .

Highly charged ions are delivered to the mass spectrometer via a time-of-flight selective beamline [22] from a Heidelberg compact EBIT [23], equipped with a laser-desorption setup [24]. A small uranium laser target was used for the uranium ion production and a collimating gas-inlet system introduces xenon gas into the EBIT. The desired charge states of U and Xe were guided through the beamline by electrostatic lenses and a bender, time-of-flight selected by a pulsed operation of a Bradbury-Nielson gate [25] and slowed down by two pulsed drift tubes. For further information on the beamline, see [22]. Afterward, the slow ions can be captured inside the Penning trap tower made up of five individual traps. Two of the inner Penning traps are used for frequency measurements, and the other three are used for ion storage. There are in total three ions loaded in alternating sequence [see Fig. 1(a)]. This way,

the three ions can be moved up or down from configuration 1 to 2 between frequency determinations, effectively swapping the ion species in each of the measurement traps. On the one hand, this double measurement scheme allows for a doubling of measurement statistics since traps two and three are used in parallel to measure a cyclotron frequency ratio each. On the other hand, the two traps have different electric and magnetic field parameters, thus allowing for the cyclotron frequency ratio comparison to ensure a reliable evaluation of systematic shifts.

To determine the frequencies of the eigenmotions of the ions, cryogenic RLC resonators are connected to the axially offset electrodes in each measurement trap [see Fig. 1(a)]. The ion interacts with the resonator via the image current induced inside the trap electrodes by the axial motion of the ion. The ion's axial frequency can be brought into resonance with the center frequency of the resonator by tuning the trap depth. Once  $\nu_z \approx \nu_{\text{res}}$ , the ion's axial motional amplitude will be damped to equilibrium with the thermal Johnson-Nyquist noise of the resonator, effectively cooling the ion's axial motion to around 4 K. Once the ion is cold, the resonator spectrum will show a "dip" signal at the ion's axial frequency [see Fig. 1(b)]. This nondestructive detection technique is called Fourier-transform ion-cyclotron resonance (FT-ICR) [26]. In order to determine the radial frequencies and reduce the radial amplitudes, one can couple each of them to the axial frequency, causing a "double-dip" from which the frequency of the coupled motion can be deduced [27]. The coupling drive can be induced by a frequency generator connected to a segmented, axially offset electrode.

In each trap, the potential is set to the same trap depth for both ion species, in order to minimize the potential systematic shifts of the measured cyclotron-frequency ratios due to the different ion positions in the traps. However, this results in different axial frequencies of the Xe and U ions due to their different  $q/m$  ratios. Variable GaAs capacitors (varactors) were recently implemented into the cryogenic RLC circuits of the traps [28] in order to adjust the resonance frequency of the detection circuit with respect to the axial frequency of the ions [see Figs. 1(a) and 1(b)].

The largest of the three eigenfrequencies, the modified cyclotron frequency  $\nu_+$ , is measured phase-sensitively using the pulse-and-phase (PnP) method [29]. A PnP sequence consists of an excitation pulse at the modified cyclotron frequency to set the initial phase, then a wait period called phase accumulation time  $t_{\text{acc}}$ , and finally a radiofrequency (rf)  $\pi$  pulse at the sideband frequency  $\nu_{\text{rf}} = \nu_+ - \nu_z$  to couple the modified cyclotron motion to the axial motion. The  $\pi$  pulse transfers not only the energy from the modified cyclotron motion to the axial motion but also its phase information, which can then be read out via the axial resonator, two amplification stages, a subsequent analog to digital converter, and by applying a Fourier transform. In order to subtract the starting phase and any shifts to the phase by the excitation and readout electronics, a "short" phase measurement with  $t_{\text{acc}} = 0.1$  s precedes the actual "long" measurement phase with an accumulation time of  $t_{\text{acc}} = 70$  to 100 s. To reduce the influence of electric field drifts in the trap, the axial frequency is measured during the long PnP phase measurement

TABLE I. The systematic shifts and their uncertainties of the cyclotron frequency ratio determination. A shift  $\Delta R$  is given as  $\Delta R = \tilde{R} - R$  with  $R$  being the unperturbed frequency ratio and  $\tilde{R}$  the measured value. The errors of the last three shifts are correlated due to their dependence on the uncertainty of the excitation radii. All values are given in  $10^{-12}$ .

	Trap 2	Trap 3
ICS	-253.1(21)	-257.1(43)
Dip lineshape	0.0(11)	0.0(64)
Nonlinear phase	0.0(6)	0.00(22)
Relativistic	0.69(26)	0.5(6)
Electrost. anharmon. $C_4$	0.00(23)	0.00(8)
Magnetic inhom. $B_2$	-0.042(12)	0.014(8)
Total systematic	-252.5(25)	-256.6(77)

of the modified cyclotron frequency  $\nu_+$  via the dip technique. The magnetron frequency, being the smallest frequency, is only measured once in the beginning of every measurement run via the double dip method. The magnetron frequency of the reference ion is, however, calculated with the help of the magnetron frequency difference measurement, which was performed for the image charge shift measurement campaign (see Supplemental Material Sec. A [30]). The reason for using the calculated magnetron frequency instead of the measured absolute frequency is, that the cyclotron frequency ratio is more sensitive to the difference of the magnetron frequencies than the absolute frequencies. With measuring the difference instead of using the absolutely measured frequency for the reference ion, we avoid an unnecessarily large uncertainty of the magnetron frequency due to the double dip measurement. Figure 1(c) shows the cyclotron frequencies and ratios in both traps of a measurement run of  $\approx 12$  h. The ratios are formed by interpolating the cyclotron frequency of one ion to the point in time of the other ion's cyclotron frequency measurement. With the described measurement scheme, we were able to demonstrate determinations of relative mass ratios with uncertainties of a few  $10^{-12}$  [31–33].

The measured cyclotron frequency ratio  $\tilde{R} = \nu_c(^{238}\text{U}^{47+})/\nu_c(^{132}\text{Xe}^{26+})$  is  $\tilde{R}_2 = 1.001\,644\,000\,787\,9(30)$  and  $\tilde{R}_3 = 1.001\,644\,000\,785\,5(25)$  for trap 2 and trap 3, respectively. This measured ratio was corrected for several systematic effects, see Table I, which are described in detail in the Supplemental Material [30]. The largest systematic correction comes from the image charge shift (ICS). This effect originates in the interaction between the ion and its image charge on the trap electrodes. The dip lineshape uncertainty originates from the fact that the analytical fit function of the dip spectrum [26] does not describe the spectrum comprehensively. In this case, the fit can yield an axial-frequency value shifted with respect to the true value. The nonlinear phase systematic is caused by a nonlinear transfer function of the ion's phase during the PnP phase readout. The uncertainty of the difference in motional radii between the uranium and the xenon ion, especially in the excited modified cyclotron motion, adds three correlated systematic effects, namely the relativistic

shift, the  $C_4$ , and the  $B_2$  term. The relativistic effect describes the relativistic mass increase of the moving particles. The  $C_4$  term approximates the effect that different motional radii have on the trap eigenfrequencies due to electrostatic anharmonicities, in leading order described by the coefficient  $C_4$ . Similarly, a quadratic inhomogeneity  $B_2$  of the magnetic trapping field will also shift the frequencies of the two ions depending on their radii. With these corrections the cyclotron frequency ratios (with the statistical, systematic, and total error in first, second, and third bracket) were determined to be  $R_2 = 1.001\,644\,001\,040\,4(30)(25)(38)$  and  $R_3 = 1.001\,644\,001\,042\,1(25)(77)(81)$  for trap 2 and trap 3, respectively. The weighted average of the cyclotron frequency ratio is:  $R = 1.001\,644\,001\,040\,7(35)$ .

The absolute mass of uranium-238 can be determined via the following formula:

$$m(^{238}\text{U}) = \frac{47}{26R}m(^{132}\text{Xe}^{26+}) + 47m_e - E_U/c^2$$

$$\text{with } m(^{132}\text{Xe}^{26+}) = m(^{132}\text{Xe}) - 26m_e + E_{\text{Xe}}/c^2. \quad (3)$$

Here,  $R$  is the systematically corrected frequency ratio determined above,  $m_e$  signifies the mass of an electron [34],  $c$  is the speed of light, and  $E_{\text{Xe}} = 8\,971.2(21)$  eV is the binding-energy difference between  $\text{Xe}^{26+}$  and neutral Xe atom determined in our previous work [22,35]. The term  $E_U = 39.7(16)$  keV represents the binding-energy difference between  $\text{U}^{47+}$  and neutral U atom, with the 1.6-keV error bar mainly coming from the large uncertainties in the theoretical ionization potentials (IPs) listed in the NIST atomic database [36]. To improve the accuracy of  $E_U$ , in this work, we will calculate it via the *ab initio* fully relativistic MCDHF and relativistic configuration interaction (RCI) methods [37–39] implemented in the GRASP2018 code [40–42]. For the sake of computational efficiency, we perform a full calculation for the binding-energy difference  $E_U^{6-46}$  between  $\text{U}^{46+}$  and  $\text{U}^{6+}$  ions that bear closed-shell ground states, with the IPs of the outermost six electrons and the IP of  $\text{U}^{46+}$  being treated separately.

In the calculation, the atomic state functions (ASFs) are expanded as linear combinations of configuration state functions (CSFs), which are *jj*-coupled Slater determinants of one-electron orbitals, with appropriate angular symmetry and parity. We first solve the MCDHF equations self-consistently [37–39] to optimize the radial wave functions of the one-electron orbital under the Dirac-Coulomb Hamiltonian. Then, the RCI method is employed to calculate the contributions from frequency-dependent and frequency-independent transverse photon interactions, the mass shift, and QED effects. Different from previous calculations for  $\text{Pb}^{4+}$ , where the intermediately charged ion  $\text{Pb}^{22+}$  had been used to bridge the calculations of the correlation energy of the 78 electrons, in this work, we have modified the GRASP2018 code such that we can directly account for the full single and double (SD) electron exchange correlations of the 86 electrons in  $\text{U}^{6+}$ . The results are summarized in Table IV of the Supplemental Materials [30]. We find that the term  $E_U^{6-46}$  is dominated by the single-configuration Dirac-Hartree-Fock binding-energy difference. Such single-configuration calculations give rise to

a value of  $37\,110.01(8)$  eV with a contribution of  $-0.47(1)$ ,  $-0.02(1)$ , and  $-0.65(6)$  eV from the finite nuclear size, the mass shift, and the QED effects, respectively. The Breit interaction and the frequency-dependent transverse-photon interaction together contribute  $-16.26$  eV whose uncertainty will be examined later in the correlation energies. To account for the correlation effects, we systematically expand the size of the CSF basis set by allowing SD excitation of electrons from all the occupied orbitals to the systematically increasing set of correlation orbitals. These correlation orbitals are added and optimized with the layer-by-layer approach [41] up to  $n = 11$  ( $n$  is the principal quantum number), where all orbitals with orbital angular momentum from 0 up to  $n - 1$  are included. By extrapolating to  $n = \infty$  [35] we obtain a contribution of  $64.7(17)$  eV to  $E_U^{6-46}$ . The contribution from correlation effects beyond the SD electron excitations are conservatively constrained to be of  $6.3(63)$  eV [22,35]. Finally, we arrive at  $E_U^{6-46} = 37\,164(8)$  eV, with the uncertainty being dominated by higher-order correlation effects (see Supplemental Material Sec. E for more details [30]).

To derive  $E_U$ , one has to add up the IP of  $\text{U}^{46+}$  as well as the IPs of the outermost 6 electrons of the uranium atom. For the IP of  $\text{U}^{46+}$ , it is calculated to be  $2580.9(1)$  eV based on CSF basis set generated via SD excitations from the  $4s$  orbital. For low charged uranium, the first three IPs are known experimentally [36]. There is also an experimental value for the IP of  $\text{U}^{3+}$ , but it is around 4 eV larger than that from a recent theoretical calculation based on the multireference configuration interaction method [43]. Nevertheless, our calculations are in good agreement with the values presented in Ref. [43]: with CSFs generated via SD excitation of electrons starting from the  $6s$  orbital, we arrive at values of  $33.12(42)$ ,  $48.14(42)$  and  $63.15(42)$  eV for the IPs of  $\text{U}^{3+}$ ,  $\text{U}^{4+}$ , and  $\text{U}^{5+}$ , respectively. In total, we obtain  $E_U^{0-6} = 182.0(20)$  eV for the total binding energy of the outermost six electrons. Thus, the binding-energy difference between neutral uranium and  $\text{U}^{47+}$  is calculated to be  $E_U = 39\,927(10)$  eV which is more than two orders of magnitude more accurate than the NIST value [36].

By combining the measured cyclotron frequency ratio with the calculated electron binding energies and the literature xenon-132 mass [15], the atomic mass of uranium-238 was calculated using Eq. (3) which yields the final value of  $m(^{238}\text{U}) = 238.050\,787\,618(15)$  u. This value represents an improvement of two orders of magnitude compared to the current literature value of  $m(^{238}\text{U}) = 238.050\,786\,9(16)$  u [15]. The associated mass excess is correspondingly determined to be  $47\,308.367(14)$  keV. With the reduced mass uncertainty of uranium-238, the atomic mass of uranium-239 which is connected to the 238 mass via a neutron capture process and plutonium-242 connected via a well-known  $\alpha$  decay energy will be improved as well by a factor of 9 and 1.5, respectively [15]. The mass excess of  $^{239}\text{U}$  is readjusted to be  $50\,573.31(17)$  keV and the one of  $^{242}\text{Pu}$  is  $54\,717.3(8)$  keV.

With the new relative mass precision of  $6 \times 10^{-11}$  achieved in this work, heavy mass determinations on short-lived nuclei, using the uranium mass as a reference, will not be limited by reference precision for the foreseeable future. A future  $g$ -factor determination of the bound electron of  $^{238}\text{U}^{91+}$  for

tests of bound-state quantum electrodynamics can now be carried out with the same precision as that of the mass [17].

This work comprises parts of the Ph.D. thesis work of K.K. to be submitted to Heidelberg University, Germany. This work is part of and funded by the Max-Planck-Gesellschaft and the DFG (German Research Foundation) - Project-ID No. 273811115 - SFB 1225 ISOQUANT. The project

received funding from the European Research Council (ERC) under the European Union's Horizon 2020 research and innovation programme under Grant Agreement No. 832848 - FunI. Furthermore, we acknowledge funding and support by the International Max-Planck Research School for Precision Tests of Fundamental Symmetries and the Max Planck, RIKEN, PTB Center for Time, Constants and Fundamental Symmetries.

- 
- [1] A. Sobiczewski and K. Pomorski, Description of structure and properties of superheavy nuclei, *Prog. Part. Nucl. Phys.* **58**, 292 (2007).
- [2] J. Hamilton, S. Hofmann, and Y. Oganessian, Search for superheavy nuclei, *Annu. Rev. Nucl. Part. Sci.* **63**, 383 (2013).
- [3] G. Audi, The Evaluation of Atomic Masses, in *Atomic Physics at Accelerators: Mass Spectrometry*, edited by D. Lunney, G. Audi, and H.-J. Kluge (Springer Netherlands, Dordrecht, 2001), pp. 7–34.
- [4] M. Block, F. Giacompo, F.-P. Heßberger, and S. Raeder, Recent progress in experiments on the heaviest nuclides at SHIP, *Riv. Nuovo Cim.* **45**, 279 (2022).
- [5] A. Poves and F. Nowacki, The Nuclear Shell Model, in *An Advanced Course in Modern Nuclear Physics*, edited by J. M. Arias and M. Lozano, Lecture Notes in Physics (Springer, Berlin, Heidelberg, 2001), pp. 70–101.
- [6] S. A. Giuliani, Z. Matheson, W. Nazarewicz, E. Olsen, P.-G. Reinhard, J. Sadhukhan, B. Schuettrumpf, N. Schunck, and P. Schwerdtfeger, Colloquium: Superheavy elements: Oganesson and beyond, *Rev. Mod. Phys.* **91**, 011001 (2019).
- [7] D. J. Fink and E. G. Myers, Deuteron-to-proton mass ratio from the cyclotron frequency ratio of  $H_2^+$  to  $D^+$  with  $H_2^+$  in a resolved vibrational state, *Phys. Rev. Lett.* **124**, 013001 (2020).
- [8] S. Sasidharan, O. Bezrodnova, S. Rau, W. Quint, S. Sturm, and K. Blaum, Penning-trap mass measurement of helium-4, *Phys. Rev. Lett.* **131**, 093201 (2023).
- [9] P. Filianin, C. Lyu, M. Door, K. Blaum, W. J. Huang, M. Haverkort, P. Indelicato, C. H. Keitel, K. Kromer, D. Lange, Y. N. Novikov, A. Rischka, R. X. Schüssler, C. Schweiger, S. Sturm, S. Ulmer, Z. Harman, and S. Eliseev, Direct  $Q$ -value determination of the  $\beta^-$  decay of  $^{187}\text{Re}$ , *Phys. Rev. Lett.* **127**, 072502 (2021).
- [10] M. Dworschak, M. Block, D. Ackermann, G. Audi, K. Blaum, C. Droese, S. Eliseev, T. Fleckenstein, E. Haettner, F. Herfurth, F. P. Heßberger, S. Hofmann, J. Ketelaer, J. Ketter, H.-J. Kluge, G. Marx, M. Mazzocco, Yu. N. Novikov, W. R. Plaß, A. Popeko *et al.*, Penning trap mass measurements on nobelium isotopes, *Phys. Rev. C* **81**, 064312 (2010).
- [11] M. Hukkanen, W. Ryssens, P. Ascher, M. Bender, T. Eronen, S. Grévy, A. Kankainen, M. Stryczyk, L. Al Ayoubi, S. Ayet, O. Beliuskina, C. Delafosse, W. Gins, M. Gerbaux, A. Husson, A. Jokinen, D. A. Nesterenko, I. Pohjalainen, M. Reponen, S. Rinta-Antila *et al.*, Odd-odd neutron-rich rhodium isotopes studied with the double Penning trap JYFLTRAP, *Phys. Rev. C* **107**, 014306 (2023).
- [12] J. Karthein, D. Atanasov, K. Blaum, S. Eliseev, P. Filianin, D. Lunney, V. Manea, M. Mougeot, D. Neidherr, Y. Novikov, L. Schweikhard, A. Welker, F. Wienholtz, and K. Zuber, Direct decay-energy measurement as a route to the neutrino mass, *Hyperfine Interact.* **240**, 61 (2019).
- [13] G. Audi, M. Wang, A. H. Wapstra, F. G. Kondev, M. MacCormick, and B. Pfeiffer, The AME2012 atomic mass evaluation, *Chin. Phys. C* **36**, 1287 (2012).
- [14] C. Guénaut, G. Audi, D. Beck, K. Blaum, G. Bollen, P. Delahaye, F. Herfurth, A. Kellerbauer, H. J. Kluge, D. Lunney, S. Schwarz, L. Schweikhard, and C. Yazidjian, Extending the mass “backbone” to short-lived nuclides with ISOLTRAP, *Eur. Phys. J. A* **25**, 35 (2005).
- [15] M. Wang, W. J. Huang, F. G. Kondev, G. Audi, and S. Naimi, The AME 2020 atomic mass evaluation (II). Tables, graphs and references, *Chin. Phys. C* **45**, 030003 (2021).
- [16] S. Sturm, I. Arapoglou, A. Egl, M. Höcker, S. Kraemer, T. Sailer, B. Tu, A. Weigel, R. Wolf, J. C. López-Urrutia, and K. Blaum, The ALPHATRIP experiment, *Eur. Phys. J. Spec. Top.* **227**, 1425 (2019).
- [17] J. Morgner, B. Tu, C. M. König, T. Sailer, F. Heiße, H. Bekker, B. Sikora, C. Lyu, V. A. Yerokhin, Z. Harman, J. R. Crespo López-Urrutia, C. H. Keitel, S. Sturm, and K. Blaum, Stringent test of QED with hydrogen-like tin, *Nature (London)* **622**, 53 (2023).
- [18] T. Beier, The  $g_j$  factor of a bound electron and the hyperfine structure splitting in hydrogenlike ions, *Phys. Rep.* **339**, 79 (2000).
- [19] L. S. Brown and G. Gabrielse, Precision spectroscopy of a charged particle in an imperfect Penning trap, *Phys. Rev. A* **25**, 2423 (1982).
- [20] J. Repp, C. Böhm, J. R. Crespo López-Urrutia, A. Dörr, S. Eliseev, S. George, M. Goncharov, Y. N. Novikov, C. Roux, S. Sturm, S. Ulmer, and K. Blaum, PENTATRIP: A novel cryogenic multi-Penning-trap experiment for high-precision mass measurements on highly charged ions, *Appl. Phys. B* **107**, 983 (2012).
- [21] C. Roux, C. Böhm, A. Dörr, S. Eliseev, S. George, M. Goncharov, Y. N. Novikov, J. Repp, S. Sturm, S. Ulmer, and K. Blaum, The trap design of PENTATRIP, *Appl. Phys. B* **107**, 997 (2012).
- [22] K. Kromer, C. Lyu, M. Door, P. Filianin, Z. Harman, J. Herkenhoff, W. Huang, C. H. Keitel, D. Lange, Y. N. Novikov, C. Schweiger, S. Eliseev, and K. Blaum, High-precision mass measurement of doubly magic  $^{208}\text{Pb}$ , *Eur. Phys. J. A* **58**, 202 (2022).
- [23] P. Micke, S. Kühn, L. Buchauer, J. R. Harries, T. M. Bücking, K. Blaum, A. Cieluch, A. Egl, D. Hollain, S. Kraemer, T. Pfeifer, P. O. Schmidt, R. X. Schüssler, Ch. Schweiger, T. Stöhlker, S. Sturm, R. N. Wolf, S. Bernitt, and J. R. Crespo López-Urrutia, The Heidelberg compact electron beam ion traps, *Rev. Sci. Instrum.* **89**, 063109 (2018).
- [24] Ch. Schweiger, C. M. König, J. R. Crespo López-Urrutia, M. Door, H. Dorrer, Ch. E. Düllmann, S. Eliseev, P. Filianin, W. Huang, K. Kromer, P. Micke, M. Müller, D. Renisch, A.

- Rischka, R. X. Schüssler, and K. Blaum, Production of highly charged ions of rare species by laser-induced desorption inside an electron beam ion trap, *Rev. Sci. Instrum.* **90**, 123201 (2019).
- [25] N. E. Bradbury and R. A. Nielsen, Absolute values of the electron mobility in hydrogen, *Phys. Rev.* **49**, 388 (1936).
- [26] X. Feng, M. Charlton, M. Holzscheiter, R. A. Lewis, and Y. Yamazaki, Tank circuit model applied to particles in a Penning trap, *J. Appl. Phys.* **79**, 8 (1996).
- [27] E. A. Cornell, R. M. Weisskoff, K. R. Boyce, and D. E. Pritchard, Mode coupling in a Penning trap:  $\pi$  pulses and a classical avoided crossing, *Phys. Rev. A* **41**, 312 (1990).
- [28] F. Heiße, F. Köhler-Langes, S. Rau, J. Hou, S. Junck, A. Kracke, A. Mooser, W. Quint, S. Ulmer, G. Werth, K. Blaum, and S. Sturm, High-precision measurement of the proton's atomic mass, *Phys. Rev. Lett.* **119**, 033001 (2017).
- [29] E. A. Cornell, R. M. Weisskoff, K. R. Boyce, R. W. Flanagan, G. P. Lafyatis, and D. E. Pritchard, Single-ion cyclotron resonance measurement of  $M(\text{CO}^+)/M(\text{N}_2^+)$ , *Phys. Rev. Lett.* **63**, 1674 (1989).
- [30] See Supplemental Material at <http://link.aps.org/supplemental/10.1103/PhysRevC.109.L021301> for details on the systematic uncertainties and on the theoretical binding energy calculations.
- [31] K. Kromer, C. Lyu, M. Door, P. Filianin, Z. Harman, J. Herkenhoff, P. Indelicato, C. H. Keitel, D. Lange, Y. N. Novikov, C. Schweiger, S. Eliseev, and K. Blaum, Observation of a low-lying metastable electronic state in highly charged lead by Penning-trap mass spectrometry, *Phys. Rev. Lett.* **131**, 223002 (2023).
- [32] C. Schweiger, M. Braß, V. Debierre, M. Door, H. Dorrer, C. E. Düllmann, C. Enss, P. Filianin, L. Gastaldo, Z. Harman *et al.*, Direct high-precision Penning-trap measurement of the  $Q$ -value of the electron capture in  $^{163}\text{Ho}$  for the determination of the electron neutrino mass, *Nat. Phys.* (to be published).
- [33] F. Heiße, M. Door, T. Sailer, P. Filianin, J. Herkenhoff, C. König, K. Kromer, D. Lange, J. Morgner, A. Rischka, C. Schweiger, B. Tu, Y. Novikov, S. Eliseev, S. Sturm, and K. Blaum, High-precision determination of  $g$  factors and masses of  $^{20}\text{Ne}^{9+}$  and  $^{22}\text{Ne}^{9+}$ , *Phys. Rev. Lett.* **131**, 253002 (2023).
- [34] J. Zatorski, B. Sikora, S. G. Karshenboim, S. Sturm, F. Köhler-Langes, K. Blaum, C. H. Keitel, and Z. Harman, Extraction of the electron mass from  $g$ -factor measurements on light hydrogenlike ions, *Phys. Rev. A* **96**, 012502 (2017).
- [35] C. Lyu, B. Sikora, Z. Harman, and C. H. Keitel, Extreme field calculations for Penning ion traps and corresponding strong laser field scenarios, *Mol. Phys.* e2252105 (2023).
- [36] A. Kramida, Yu. Ralchenko, J. Reader, and NIST ASD Team, NIST Atomic Spectra Database (version 5.8), [Online], <https://physics.nist.gov/asd> (National Institute of Standards and Technology, Gaithersburg, MD, 2021).
- [37] I. P. Grant, Relativistic calculation of atomic structures, *Adv. Phys.* **19**, 747 (1970).
- [38] J. P. Desclaux, D. F. Mayers, and F. O'Brien, Relativistic atomic wave functions, *J. Phys. B* **4**, 631 (1971).
- [39] I. P. Grant, *Relativistic Quantum Theory of Atoms and Molecules*, Springer Series on Atomic, Optical, and Plasma Physics, Vol. 40 (Springer, Berlin, 2007).
- [40] C. Froese Fischer, G. Gaigalas, P. Jönsson, and J. Bieroń, GRASP2018—A FORTRAN 95 version of the General Relativistic Atomic Structure Package, *Comput. Phys. Commun.* **237**, 184 (2019).
- [41] P. Jönsson, G. Gaigalas, C. Froese Fischer, J. Bieroń, I. P. Grant, T. Brage, J. Ekman, M. Godefroid, J. Grumer, J. Li, and W. Li, GRASP manual for users, *Atoms* **11**, 68 (2023).
- [42] P. Jönsson, M. Godefroid, G. Gaigalas, J. Ekman, J. Grumer, W. Li, J. Li, T. Brage, I. P. Grant, J. Bieroń, and C. Froese Fischer, An introduction to relativistic theory as implemented in GRASP, *Atoms* **11**, 7 (2023).
- [43] D. H. Bross, P. Parmar, and K. A. Peterson, Multireference configuration interaction calculations of the first six ionization potentials of the uranium atom, *J. Chem. Phys.* **143**, 184308 (2015).

## Supplemental material to the paper on the uranium-238 atomic mass determination

This Supplemental Material describes in more detail the relevant systematic measurements and estimations as well as the contributions to the theoretical binding energy of the missing electrons of  $^{238}\text{U}^{47+}$  for the determination of the atomic mass of uranium-238.

### A. SYSTEMATIC MEASUREMENT: THE IMAGE CHARGE SHIFT

The image charge induced by an ion inside a Penning trap can be used for a non-destructive measurement of the ion's eigenfrequencies and for cooling of the ion's motions. However, the image charge also forms an electric field acting back on the ion and shifting its trap-motion frequencies and hence the free cyclotron frequency. This effect is called image charge shift (ICS) [1]. In the case of mass ratio determinations at PENTATRAP with large mass differences such as Xe and U, this causes the dominating systematic shift and the leading systematic error since the analytical calculation of the ICS in Penning traps was, so far, only tested experimentally with an uncertainty of 5% [2]. Measurements of the ICS are based on a precise determination of the magnetron frequency  $\nu_-$  because this motion has the least sensitivity to magnetic field fluctuations compared to the modified cyclotron frequency and it has a larger ICS compared to the axial frequency. In order to test the ICS to below 5%, it was necessary to measure the magnetron frequency difference between reference and ion of interest with an uncertainty of  $< 0.25$  mHz. This was achieved by optimizing the pulse sequence by pulse shaping, making it possible to measure the magnetron frequency phase sensitively by the use of the pulse and phase (PnP) method [3]. Only with this phase sensitive method was it possible to determine the magnetron frequency difference  $\Delta\nu_-^{\text{exp}}$  between Xe and U to a precision of 40 or 90  $\mu\text{Hz}$ , corresponding to an uncertainty of the ICS determination of 0.8% or 1.7%, in trap 2 or 3, respectively.

The PnP scheme for the magnetron motion follows the same principles as for the modified cyclotron motion described in the paper. First, the magnetron motion is excited with a radio-frequency (RF) pulse at frequency  $\nu_-$  to set an initial phase. Then, the magnetron motion evolves freely for a time  $t_{\text{acc}}$ , accumulating its phase. The final magnetron phase is then read out by coupling the magnetron motion to the axial motion, transferring its phase information by an RF  $\pi$ -pulse at the sideband frequency  $\nu_{\text{rf}} = \nu_z + \nu_-$ . Finally, the phase can be measured with the axial detection system. In order to subtract any offset phase caused by the RF electronics of the excitation and detection system, this PnP scheme always includes a "short" reference phase ( $t_{\text{acc}} = 0.1$  s) which is subtracted from a "long" phase ( $t_{\text{acc}} = 80$  s) to calculate the measurement phase. The experimental magnetron frequency differences between a U and a Xe ion are given in Tab. I as  $\Delta\nu_-^{\text{exp}}$ .

The systematic uncertainty of  $\Delta\nu_-^{\text{exp}}$  stems from a non-linearity in readout phase originating from the  $\pi$ -pulse

TABLE I. The magnetron frequency difference between a U and a Xe ion is calculated as  $\Delta\nu_- = \nu_-(^{238}\text{U}^{47+}) - \nu_-(^{132}\text{Xe}^{26+})$ .  $\Delta\nu_-^{\text{exp}}$  is the experimentally measured frequency difference, while  $\Delta\nu_-^{\text{id}}$  is the calculated one and its uncertainty is due to the systematic shifts except for the ICS. With the resulting difference between these two values due to the image charge shift  $\Delta\Delta\nu_-^{\text{ICS}}$ , an effective trap radius  $r_{\text{eff}}$  can be calculated. For the experimental value the uncertainty is given as statistical, systematic, and total uncertainty in the first, second, and third bracket, respectively. Other than that only the total uncertainty is noted.

	Trap 2	Trap 3
$\Delta\nu_-^{\text{exp}}$ (mHz)	-4.83(4)(2)(4)	3.23(4)(8)(9)
$\Delta\nu_-^{\text{id}}$ (mHz)	-10.212(20)	-2.235(20)
$\Delta\Delta\nu_-^{\text{ICS}}$ (mHz)	5.38(4)	5.46(9)
$r_{\text{eff}}$ (mm)	5.036(14)	5.010(28)

when transferring the phase information from the magnetron to the axial motion. This means that the readout phase is not precisely equal to the phase that the magnetron motion had before coupling but has an additional non-linear (sinusoidal with amplitude  $A$ ) transfer function dependent on the ion's phase, see Fig. 1. The amplitude of the effect was measured to be for trap 2:  $A_2 = 0.0073(29)$  rad and for trap 3:  $A_3 = 0.0236(48)$  rad.

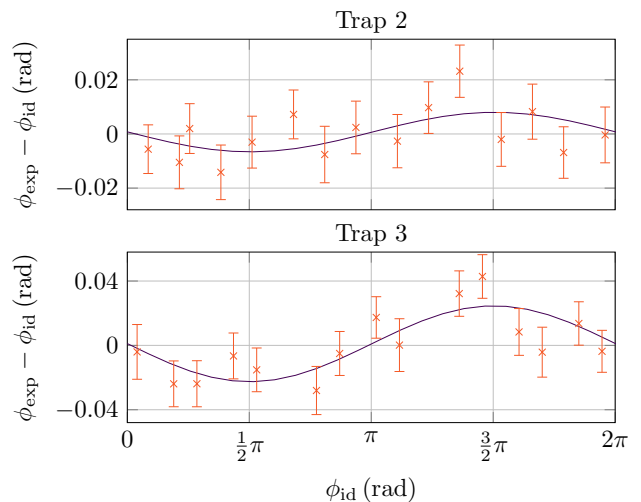


FIG. 1. Measurement data (orange) and sine fit (purple) of the nonlinearity measurement of the magnetron phase. The ideal reference phase  $\phi_{\text{id}}$  is calculated from the magnetron frequency. The deviation of the measured phase  $\phi_{\text{exp}}$  from the ideal phase is plotted on the y axis.



The largest effect on the magnetron frequency by this phase modulation will come from the short reference phase because the long (80 s) phases fluctuate over time due to voltage instabilities, so the modulation will cause an increase in statistical phase uncertainty but no systematic shift. The reference phase, however, with an accumulation time of only 0.1 s, does not fluctuate because it is insensitive to small changes in voltage due to its low frequency resolution. By combining the amplitude with the reference phase difference between the U and Xe ions  $\Delta\phi_{\text{short}} \approx 1.1$  rad in trap 2 and  $\Delta\phi_{\text{short}} \approx 2.2$  rad in trap 3, one can calculate an upper limit of the systematic uncertainty by considering the steepest phase gradient:

$$\Delta\nu_- = \frac{2 \sin(\Delta\phi_{\text{short}}/2) A}{2\pi \Delta t_{\text{acc}}}, \quad (1)$$

with  $\Delta t_{\text{acc}}$  representing the difference of the phase accumulation times of the short and the long phase. The uncertainty is calculated to be  $20 \mu\text{Hz}$  for trap 2 and  $80 \mu\text{Hz}$  for trap 3.

The analysis of the image charge shift follows the principles described in detail in [2]. First, one has to determine the ideal magnetron frequencies of Xe and U without any systematic shifts by:

$$\nu_-^{\text{id}} = \frac{\nu_c}{2} - \sqrt{\frac{\nu_c^2}{4} - \frac{\nu_z^2}{2}}. \quad (2)$$

These ideal frequencies  $\nu_-^{\text{id}}$  are calculated by using the measured frequencies for uranium, taken from one of the measurement runs of the uranium mass determination and then calculating the frequencies for Xe using the values of the magnetic and electrostatic field one can extract from the uranium frequencies. Although the measured frequencies are altered by systematic shifts, the influence of these shifts on the calculation of the magnetron frequency by Eq. (2) is only on the order of a few  $\mu\text{Hz}$ , so we can still consider this an ideal magnetron frequency difference  $\Delta\nu_-^{\text{id}}$  for this purpose. The difference of the ideal magnetron frequencies can be found in Tab. I. This ideal magnetron frequency difference has to be corrected for different frequency shifts of a “real” Penning trap and the remaining difference to the measured magnetron frequency can then be identified as the image charge shift. Effects that shift the magnetron frequency away from the ideal value include the quadratic magnetic inhomogeneity  $B_2$ , electrostatic anharmonicities terms like  $C_4$  and the tilting angle between magnetic and electrostatic trapping fields as well as an ellipticity of the otherwise harmonic electric field due to e.g. manufacturing tolerances or patch potentials on the trap electrodes. A list of the relevant trap parameters can be found in Tab. II. The shift of  $\Delta\nu_-$  due to  $B_2$  scales mainly with the difference in thermal cyclotron radii of the two ion species which for the heavy ions used in this measurement resulted in a negligible shift of  $< 1 \times 10^{-4}$  mHz with respect to the total error of  $\Delta\nu_-^{\text{id}}$  (see Tab. I) [7]. Anharmonicities in the electrostatic field  $C_k$ , see Tab. II, will not shift the

TABLE II. Trap parameters relevant in the analysis of the systematic effects. If there are two values given, the first one concerns  $^{238}\text{U}^{47+}$  and the second one  $^{132}\text{Xe}^{26+}$ . The magnetic field was calculated using the cyclotron frequency  $\nu_c$  from a dip/double dip measurement of  $^{132}\text{Xe}^{26+}$  using the literature value for the atomic mass of Xe [4]. For numbers that were determined or simulated prior to this work, the source is given.

	Trap 2	Trap 3	source
$r_0$ (mm)	5.000(5)	5.000(5)	[5, 6]
$TR$	0.87987(18)	0.87966(7)	
$U_0$ (V)	-33.9	-15.85	
$Q$ -factor	$\approx 3800$	$\approx 9400$	
$\nu_+$ MHz	$\approx 21.22/21.19$	$\approx 21.22/21.19$	
$\nu_z$ kHz	$\approx 698.0/697.4$	$\approx 477.5/477.1$	
$\nu_-$ kHz	$\approx 11.5$	$\approx 5.4$	
$B_0$ (T)	7.002 147 55(33)	7.002 155 20(33)	
$B_2$ ( $\frac{\text{mT}}{\text{m}^2}$ )	27.7(1.9)	-4.7(2.1)	
$C_4$ ( $\frac{1}{\text{mm}^4}$ )	$0.0(15) \times 10^{-7}$	$0.0(06) \times 10^{-7}$	[6]
$C_6$ ( $\frac{1}{\text{mm}^6}$ )	$0.0(19) \times 10^{-7}$	$0.0(19) \times 10^{-7}$	[6]

the magnetron frequency difference on a relevant level. The uncertainty on the leading anharmonicity term  $C_4$  causes an uncertainty on the magnetron difference calculations of  $7 \times 10^{-3}$  and  $3 \times 10^{-3}$  mHz in trap 2 and trap 3, respectively [7].

The impact of an angle  $\theta$  between magnetic field and trap axis, as well as an ellipticity  $\epsilon$  on the calculated magnetron frequency difference between uranium and xenon has to be determined without knowing a priori the tilt and ellipticity of our traps. The systematic shift of the magnetron frequency difference  $\Delta\Delta\nu_-$  can be described by [8]

$$\Delta\Delta\nu_- \approx \Delta\nu_- \left( \frac{3}{4}\theta^2 \left( 1 + \frac{1}{3}\epsilon \cos(2\phi) \right) + \frac{1}{2}\epsilon^2 \right), \quad (3)$$

in which the angle  $\phi$  can be set to  $0^\circ$ . Both, the ellipticity and the angle  $\theta$  manifest as a mismatch  $\Delta\nu_c^{\text{sb},i}$  between the cyclotron frequency measured using the invariance theorem vs. using the sideband relation ( $\nu_c = \nu_+ + \nu_-$ ) [9]:

$$\Delta\nu_c^{\text{sb},i} = \nu_c^{\text{sb}} - \nu_c^{\text{inv}} = \nu_- \left( \frac{9}{4}\theta^2 - \frac{1}{2}\epsilon^2 \right). \quad (4)$$

While  $\Delta\nu_c^{\text{sb},i}$  was measured during the measurement campaign, this is insufficient to solve for the two unknowns angle  $\theta$  and ellipticity  $\epsilon$ . We have therefore conservatively estimated that the tilting angle of our traps will not exceed  $\theta < 0.0262$  rad  $\approx 1.5^\circ$ . Using the estimated worst-case value of the angle  $\theta$ , the measured value for  $\Delta\nu_c^{\text{sb},i}$ , Eq. (3), and Eq. (4), one can calculate an upper limit of the ellipticity of our traps and the systematic shift to be  $\epsilon < 0.055$  and  $\Delta\Delta\nu_- < 0.02$  mHz, respectively. To be sure this angle estimation is large enough one can compare the calculated ellipticity of  $\epsilon < 0.055$  to an ellipticity purely due to the electrode’s machining tolerances of  $5 \mu\text{m}$  [5], which would give a limit of

$\epsilon < 1 \times 10^{-3}$ . This value lies comfortably below the one in our estimation. Since these are estimates, no shift was subtracted from the ideal magnetron frequency difference but its error was increased to a value of 0.02 mHz.

The differential ICS  $\Delta\Delta\nu_-^{\text{ICS}}$  can now be calculated as the difference between the experimental and the ideal magnetron difference:

$$\Delta\Delta\nu_-^{\text{ICS}} = \Delta\nu_-^{\text{exp}} - \Delta\nu_-^{\text{id}} \quad (5)$$

The ICS can be analytically calculated in case of an infinitely long cylinder with radius  $r_0$ . However, the real Penning trap electrodes are not infinitely long and they have slits between them which are necessary to apply the electrostatic trapping field and excitation pulses. The deviation from the ideal case of an infinitely long cylinder can be approximated by calculating an effective trap radius  $r_{\text{eff}} = r_0 + \delta$ . From the differential ICS in the magnetron mode one can calculate back to these effective trap radii  $r_{\text{eff}}$  for each trap, see Tab. I, which we then used to determine the ICS of the free cyclotron frequencies during the mass measurements, see Tab. III. This is done with the following equations, which are the analytical solutions for the case of an infinitely long cylinder but substituting  $r_{\text{eff}}$  for  $r_0$  [10]:

$$\Delta\Delta\nu_-^{\text{ICS}} = \frac{q_U - q_{\text{Xe}}}{8\pi^2\epsilon_0 r_{\text{eff}}^3 B_0} \quad (6)$$

$$\frac{\Delta\nu_c}{\nu_c} = \left( -\frac{\nu_+}{\nu_c} + \frac{\nu_-}{\nu_c} \right) \frac{m}{4\pi\epsilon_0 r_{\text{eff}}^3 B_0^2}. \quad (7)$$

TABLE III. The systematic shifts and their uncertainties of the cyclotron frequency ratio determination. A shift  $\Delta R$  is given as  $\Delta R = \tilde{R} - R$  with  $R$  being the unperturbed frequency ratio and  $\tilde{R}$  the measured value. The errors of the last three shifts are correlated due to their dependence on the uncertainty of the excitation radii. All values are given in  $10^{-12}$ .<sup>a</sup>

	Trap 2	Trap 3
ICS	-253.1(21)	-257.1(43)
Dip lineshape	0.0(11)	0.0(64)
Non-linear phase	0.0(6)	0.00(22)
Relativistic	0.69(26)	0.5(6)
Electrostatic. anharm. $C_4$	0.00(23)	0.00(8)
Magnetic inhom. $B_2$	-0.042(12)	0.014(8)
Total systematic	-252.5(25)	-256.6(77)

<sup>a</sup> This table can also be found in the main paper.

## B. SYSTEMATIC EFFECT: THE DIP LINESHAPE EFFECT

The thermalized ion's axial motion coupled to a cryogenic tank circuit reveals itself in the Johnson-Nyquist-noise frequency spectrum of the tank circuit (further: resonator spectrum) as a dip at the frequency of the ion's

axial motion (further: dip spectrum). A plot of an exemplary dip spectrum in trap 2 can be found in the main article. The analytical fit function of the dip spectrum is described in [11]. The fit of an ideal dip spectrum yields the same, 'true', value of the axial frequency regardless of the position of the dip with respect to the resonator spectrum. In practice, the dip spectrum might be subject to shape distortions due to various effects. In this case the ideal fit function does not correctly describe an experimental dip spectrum and hence can yield an axial-frequency value shifted with respect to the true value. Furthermore,  $\nu_z$  extracted from the dip-fit might depend on the position of the dip with respect to the resonator center frequency  $\nu_{\text{res}}$  and on the fit parameters.

The systematic effects not included in the uncertainty calculated by the covariance matrix of the axial dip-fit can be split into two highly correlated effects. The first effect is the influence of the fit parameters on the determination of  $\nu_{\text{res}}$ . The second effect comes from the use of the varactor, which we use to shift  $\nu_{\text{res}}$  to match with  $\nu_z$  of either Xe or U. Both effects, since highly correlated via  $\nu_{\text{res}}$ , will be summed up in the end.

In the following two sections, if there are two numbers given, the first always refers to trap 2 and the second to trap 3.

### a. Resonator center frequency uncertainty

The variation of the fit parameters of the resonator spectra in trap 2 and trap 3 yielded a variation of the fitted  $\nu_{\text{res}}$  within  $\pm 0.9$  Hz and  $\pm 1$  Hz, respectively. The size of the effect on the axial frequency by this  $\nu_{\text{res}}$  uncertainty can be determined by fitting the dip spectrum using different resonator center frequencies. The fit of the dip spectra in trap 2 and trap 3 yielded, for small detunings, a dependence of the axial frequency on the  $\nu_{\text{res}}$  of 0.001 2(6)/0.010 7(7) Hz per 1 Hz detuning for uranium ions and 0.000 70(25)/0.005 9(8) Hz per 1 Hz detuning for xenon ions. The effect varies between different traps and ion species due to the different  $Q$ -factors of the resonators and different dip widths. The resonator  $Q$ -factors can be found in Tab. II. This amounts to a systematic uncertainty on the cyclotron-frequency ratio of  $0.9 \times 10^{-12}/5.1 \times 10^{-12}$ .

### b. Axial and resonator center frequency differences

In order to adjust  $\nu_{\text{res}}$  to the dip frequency, we alter the capacitance of the resonant tank circuit by employing varactors in the circuit. A change of the varactor voltage not only shifts the resonant frequency of the tank circuit, but can also distort the shape of the resonator spectrum, e.g. by a different noise background at different frequencies. In order to determine the dependence of the axial frequency on the varactor voltage, we carried out a systematic measurement, moving  $\nu_{\text{res}}$  around the

axial frequency by a few Hz. The resulting uncertainty amounts to an axial shift of  $0.000\,15(8) / 0.001\,4(4)$  Hz per Hz resonator shift. The different orders of magnitude of the effect in trap 2 and 3 are due to the difference in  $Q$ -factor of the resonators in the respective traps, see Tab. II, and by extension the different dip widths. If both ions' axial frequencies are detuned from the center frequency of the resonator by the same amount, the systematic effect cancels out to first order when forming the cyclotron frequency ratio. If the axial frequencies of uranium and xenon relative to their respective resonator center frequencies are different:

$$\Delta_{\text{U/Xe}} = \Delta\nu_{\text{U}} - \Delta\nu_{\text{Xe}} \neq 0 \quad (8)$$

with  $\Delta\nu_{\text{ion}} = \nu_{\text{res,ion}} - \nu_{z,\text{ion}}$ , there will be a systematic uncertainty. The difference  $\Delta_{\text{U/Xe}}$  averaged over all measurement runs is  $0.83/0.88$  Hz. By multiplying this with the measured axial shifts one gets a systematic uncertainty of the cyclotron frequency ratio of  $2 \times 10^{-13}/1.3 \times 10^{-12}$ .

Overall, the conservative uncertainty due to the two dip lineshape effects described in Sect. B a and Sect. B b amounts to  $1 \times 10^{-12}$  in trap 2 and  $6 \times 10^{-12}$  in trap 3.

### C. NON-LINEAR PHASE EFFECT

As described in Sect. A, the  $\pi$ -pulse during the PnP sequence necessary to transfer the phase information from one mode to another can produce a shift of the ion's read-out phase. This modulation of the original modified cyclotron phase during transfer to the axial motion was measured and fitted with a sine function. The amplitudes for trap 2 and 3 were determined to be  $A_2 = 0.002\,9(26)$  rad and  $A_3 = 0.004\,5(44)$  rad. The long phases of the PnP cycle drift over time by several  $2\pi$  rad due to a slow loss of magnetic field due to the flux creep effect [12]. Therefore, the non-linear phase effect of the long phases presents itself as an increase in statistical uncertainty. However, the short cyclotron phases are stable over time and will have to be considered as a possible source of a systematic effect. Eq. (1) is also valid for the case of the modified cyclotron phase. The difference of the short phases  $\Delta\phi_{\text{short}}$  between the U and the Xe ions are  $\Delta\phi_{\text{short}} = 2.26(24)$  rad in trap 2 and  $\Delta\phi_{\text{short}} = 0.71(29)$  rad in trap 3. Since the systematic effect will be calculated as an uncertainty and not a shift, the sign of the phase difference does not play a role and the absolute values are given. With these values a worst-case systematic uncertainty can be calculated, using Eq. (1) and  $\Delta t_{\text{acc}} \geq 69.95$  s, resulting in  $6 \times 10^{-13}$  in trap 2 and  $2.2 \times 10^{-13}$  in trap 3. The non-linear phase effect depends strongly on the coupling time, pulse shape and frequency and will therefore have to be measured with every new measurement run at PENTATRAP. In the future, it is planned to randomize the phase of the excitation pulse which will randomize the effect as well,

thereby omitting the systematic shift in favor of a larger statistical error.

### D. SYSTEMATIC EFFECTS DUE TO DIFFERENT CYCLOTRON RADII

Several systematic shifts can be caused by a difference in the radius of the cyclotron motion between reference and ion of interest during the pulse and phase (PnP) cycle. The difference in excitation radius occurs if the transfer function of the excitation pulse to the trap electrodes is frequency-dependent. Since  $^{132}\text{Xe}^{26+}$  and  $^{238}\text{U}^{47+}$  have a significant difference in the modified cyclotron frequency of  $\approx 35\,850$  Hz, we cannot exclude a different amplitude of the excitation pulse at the position of the ion. In order to determine the size of this effect, we measured the difference in radius of the excited cyclotron motion  $\Delta\rho_{+, \text{exc}}$  between the two different ion species in each trap. In order to do so, we shifted the voltages of the correction electrodes away from the optimized voltage to create a strongly anharmonic potential and then measured the difference in axial frequency between the ion with an excited cyclotron motion versus with a cooled cyclotron motion. This difference in axial frequency contains the information of the excited cyclotron radius, which can then be compared between the two ion species [7]. With this method we determined the ion radius after the excitation pulse used during the measurement for trap 2/trap 3 respectively:  $13.6(4)/19.6(5)$   $\mu\text{m}$  for  $^{132}\text{Xe}^{26+}$  and  $13.4(4)/19.4(5)$   $\mu\text{m}$  for  $^{238}\text{U}^{47+}$ . Thus, the cyclotron radii of U and Xe might differ on a level of 1-2 percent.

For calculating the excitation radii and the following systematic shifts, a few necessary trap parameters are summarized in Tab. II.

#### a. The relativistic shift

Every moving particle will have a relativistic mass increase of its rest mass  $m_0$  of:

$$m = \frac{m_0}{\sqrt{1 - (v/c)^2}}, \quad (9)$$

with  $v$  representing the particle's velocity and  $c$  the speed of light. During a PnP cycle the radius of the modified cyclotron motion  $\rho_+$  is excited to define the starting phase. As described above, this excitation radius  $\rho_{+, \text{exc}}$  might not be identical for both ions, and the relativistic mass increase might, therefore, not cancel out completely when forming the cyclotron frequency ratio. The remaining systematic ratio shift arising from the relativistic mass increase can, due to the strong frequency hierarchy, be approximated, using just the modified cy-

clotron frequency  $\nu_+$ :

$$\frac{\Delta\nu_c}{\nu_c} = 1 - \frac{m_0}{m} \approx -\frac{v_+^2}{2c^2} = -\frac{\omega_+^2 \rho_{+,exc}^2}{2c^2} = -\frac{2\pi^2 \nu_+^2 \rho_{+,exc}^2}{c^2}. \quad (10)$$

This approximation has been shown to be valid in [13]. The resulting systematic frequency ratio shifts were calculated to be:  $6.9(26) \times 10^{-13}$  and  $5(6) \times 10^{-13}$  for trap 2 and 3, respectively.

### b. Electrostatic imperfections: $C_4$

PENTATRAP uses the typical cylindrical trap geometry with 5 electrodes with different lengths but the same radius. The lengths of the trap electrodes are chosen such that the potential best resembles a harmonic potential in the trap center when applying a certain compensation voltage  $V_c$  to the correction electrodes [6]. The traps are mirror symmetric with respect to the plane of the central ring electrode. This allows to describe the potential  $\Phi$  in the trap center as a series of Legendre polynomials  $P_k$  with purely even orders [14]:

$$\Phi(z, \rho) = V_0 \sum_{k=1}^{\infty} C_k (z^2 + \rho^2)^{k/2} P_k \left( \frac{z}{\sqrt{z^2 + \rho^2}} \right) \quad (11)$$

in cylindrical coordinates  $z, \rho$ . The coefficients  $C_k$  depend on the geometrical structure and the applied voltages. Before each measurement campaign  $C_4$  is optimized via the tuning ratio  $TR = U_c/U_0$  to be as small as possible. The optimized values for the uranium campaign can be found in Tab. II. The remaining uncertainty of  $C_4$  causes an uncertainty of the cyclotron frequency ratio of 2.3 and  $0.8 \times 10^{-13}$  in trap 2 and 3, respectively. For the individual shifts of each of the eigenmodes, see [7].

Other systematic shifts dependent on the different cyclotron radii such as higher order electrostatic imperfections e.g.  $C_6$  lie far below  $10^{-13}$  and can therefore be set to zero.

### c. Magnetic inhomogeneity $B_2$

The magnetic field of the PENTATRAP magnet is not perfectly homogeneous. The remaining quadratic magnetic inhomogeneity  $B_2$  at the center of the traps causes small shifts of the eigenmotions. The first order of these shifts is described in [7]. With this, the  $B_2$  shift can be calculated to be  $-4.2(1.2) \times 10^{-14}$  for trap 2 and  $1.4(8) \times 10^{-14}$  for trap 3.

## E. CONTRIBUTIONS TO THE BINDING ENERGY DIFFERENCE BETWEEN $U^{6+}$ AND $U^{46+}$

For  $U^{6+}$  with a ground state of  $[\text{Hg}]6p^6 \ ^1S_0$ , the Dirac-Hartree-Fock calculation based on this

single-configuration gives rise to a binding energy of 763 659.36 eV for a point-like nuclear charge. However, with a finite-size nucleus, one obtains a correction of 488.16(40) eV under a Fermi model [15, 16], with the uncertainty coming from the inaccurate nuclear radius [17]. In the following, all calculations are based on such an extended nuclear potential. First, the corresponding mass shift (MS) is  $-1.39(24)$  eV with an accuracy to the order of  $(m_e/M)(\alpha Z)^4 m_e c^2$  ( $M$  is the mass of the nucleus). Then, the transverse photon interaction contributes an energy of  $-1 023.22$  eV from the frequency-independent terms (Breit interaction), with the frequency-dependent terms adding 27.33 eV to the total binding energy. Furthermore, the vacuum polarization (VP) and self-energy (SE) effects are accounted for via a screened-hydrogenlike model [18] in the GRASP2018 package [19–21]. With values  $-231.41$  and  $931.63$  eV, respectively, these QED effects reduce the binding energy of  $U^{6+}$  by 700.22 eV. To estimate its accuracy, the QED effects of  $U^{88+}$  are calculated with the GRASP2018 code as well. With a value of 625.02 eV, it is 8.61-eV larger than the accurate *ab initio* result [22, 23]. Assuming a similar systematic error, we obtain a QED contribution of  $-690.6(96)$  eV to the total binding energy of  $U^{6+}$ . Nevertheless, all of the above corrections are significant only for inner-shell electrons such that most of their effects in  $U^{6+}$  cancel with the corresponding effects in  $U^{46+}$ . As a consequence, as shown in the third row of Table IV, the term  $E_U^{6-46}$  is dominated by the 37.1-keV DHF energy difference, with contributions of  $-0.47(1)$ ,  $-0.02(1)$ , and  $-0.65(6)$  eV from the finite nuclear size (FNS), the MS and the QED effects, respectively. While the uncertainties of the differential FNS and MS terms are assumed to bear the same relative uncertainties as those in individual ions, the uncertainty of the QED correction is conservatively given as 10% of the differential QED contribution. For the energies of the DHF and the transverse photon interactions, their values depend on the basis employed in the calculation. Such a basis dependency is resolved after fully taking into account the correlation effect. Therefore, their uncertainties will be accounted for in the correlation energies discussed below.

To account for the correlation energies, we systematically expand the size of the CSF basis set by allowing single and double (SD) excitation of electrons, in both  $U^{46+}$  and  $U^{6+}$  ions, from all the occupied orbitals of the ground-state configuration to high-lying correlation orbitals. These correlation orbitals are added and optimized via the layer-by-layer approach [20] up to  $n = 11$  ( $n$  is the principal quantum number), where all orbitals with orbital angular momentum from 0 up to  $n - 1$  are included. At each layer, the increment of the correlation energy decreases exponentially as a function of  $n$  [24]. Thus, via extrapolating to  $n = \infty$ , we obtain a SD correlation energy of 93.57(37) and 158.2(15) eV for  $U^{46+}$  and  $U^{6+}$ , respectively. The uncertainties are the differences between extrapolation results based on different number of data points.

TABLE IV. Different contributions to the total binding energies of  $^{238}\text{U}^{46+}$  and  $^{238}\text{U}^{6+}$ : DHF<sub>0</sub> the DHF energy assuming a point-like nuclear charge; FNS, the finite nuclear size effect; MS, the mass shift; Breit, the frequency-independent transverse photon interaction;  $\omega$ TP, the frequency-dependent transverse photon interaction; QED, the QED contribution based on screened-hydrogenic model; SDC, the correlation energies arising from single and double electron excitations; HOc, the systematic effect from all unaccounted correlation effects. The uncertainties of DHF<sub>0</sub>, Breit and  $\omega$ TP terms are accounted for as a whole in the SDC and HOc terms. The final results are round up to integer values. All entries are shown in units of eV.

ions	ground state	DHF <sub>0</sub>	FNS	MS	Breit	$\omega$ TP	QED	SDc	HOc	total
$\text{U}^{6+}$	$[\text{Hg}]6p^6\ ^1S_0$	763 659.36	488.16(40)	-1.39(24)	-1 023.22	27.33	-690.6(96)	158.3(15)	8.6(86)	761 650(20)
$\text{U}^{46+}$	$[\text{Kr}]4d^{10}\ ^1S_0$	726 549.35	487.68(40)	-1.38(24)	-1 007.03	27.41	-689.9(96)	93.57(37)	2.3(23)	724 487(13)
$E_{\text{U}}^{6-46}$		37 110.01	-0.47(1)	-0.02(1)	-16.18	-0.08	-0.65(6)	64.7(17)	6.3(63)	37 164(8)

Furthermore, there are correlation effects beyond the SD electron exchanges. These effects are difficult to evaluate, but can be constrained from the theoretical and experimental IPs of low charged ions. To achieve this aim, we calculated the IP of Fr-like  $\text{Th}^{3+}$ , which has a 5*f* valence electron outside of the  $[\text{Hg}]6p^6$  core (the IP of Fr-like  $\text{U}^{5+}$  is not experimentally known to high accuracy). Based on the SD excitations from the 5*s* orbital to virtual orbitals up to  $n = 10$ , the calculated IP of  $\text{Th}^{3+}$  is 0.42 eV smaller than the experimental value of 28.648(25) eV. Though SD excitations starting from the 4*s* orbital generate 4 million CSFs at  $n = 8$  for the expansion of the ground state of  $\text{Th}^{3+}$  with  $J = 5/2$ , the calculated IP is projected to be 0.94 eV smaller than the experimental values. Further inclusion of core orbitals below the 4*s* orbital in the calculation of  $\text{Th}^{3+}$  would generate CSF basis sets intractable with the computer cluster we used.

In order to detect the systematic effects arising from

the 1*s* – 3*d* orbitals, the binding-energy difference between  $\text{U}^{6+}$  and  $\text{U}^{24+}$ , noted as  $E_{\text{U}}^{6-24}$ , are calculated based on three schemes – containing CSFs generated via SD excitations starting from the 1*s*, 4*s* and 5*s* orbitals, respectively. With an average value of 5 725.72 eV, the three results agree with each other within 1.4 eV, indicating that the SD core–core correlation contributions to  $E_{\text{U}}^{6-24}$  bear a significant cross cancellation between the two ions. Nevertheless, to account for the uncertainties arising from higher-order correlation effects, we conservatively assume the corresponding systematic shift decreases linearly from 1.0 eV for  $\text{U}^{6+}$  to 0.1 eV for  $\text{U}^{24+}$ , and then assume a maximum shift of 0.1 eV for all ions with higher charges [24]. With this, the total higher-order correlation effect is constrained to be less than 12.65 eV. To cover this effect, we add a correction of 6.3(63) eV to the binding-energy difference and obtain  $E_{\text{U}}^{6-46} = 37 164(8)$  eV.

- 
- |   |   |
|---|---|
| <p>[1] R. S. Van Dyck, F. L. Moore, D. L. Farnham, and P. B. Schwinberg, Number dependency in the compensated Penning trap, <i>Phys. Rev. A</i> <b>40</b>, 6308 (1989).</p> <p>[2] M. Schuh, F. Heiße, T. Eronen, J. Ketter, F. Köhler-Langes, S. Rau, T. Segal, W. Quint, S. Sturm, and K. Blaum, Image charge shift in high-precision Penning traps, <i>Phys. Rev. A</i> <b>100</b>, 023411 (2019).</p> <p>[3] E. A. Cornell, R. M. Weisskoff, K. R. Boyce, R. W. Flanagan, G. P. Lafyatis, and D. E. Pritchard, Single-ion cyclotron resonance measurement of <math>M(\text{CO}^+)/M(\text{N}_2^+)</math>, <i>Phys. Rev. Lett.</i> <b>63</b>, 1674 (1989).</p> <p>[4] M. Wang, W. J. Huang, F. G. Kondev, G. Audi, and S. Naimi, The AME 2020 atomic mass evaluation (II). Tables, graphs and references, <i>Chin. Phys. C</i> <b>45</b>, 030003 (2021).</p> <p>[5] J. Repp, C. Böhm, J. R. Crespo López-Urrutia, A. Dörr, S. Eliseev, S. George, M. Goncharov, Y. N. Novikov, C. Roux, S. Sturm, S. Ulmer, and K. Blaum, PENTATRAN: A novel cryogenic multi-Penning-trap experiment for high-precision mass measurements on highly charged ions, <i>Appl. Phys. B</i> <b>107</b>, 983 (2012).</p> <p>[6] C. Roux, C. Böhm, A. Dörr, S. Eliseev, S. George, M. Goncharov, Y. N. Novikov, J. Repp, S. Sturm, S. Ulmer, and K. Blaum, The trap design of PENTATRAN, <i>Appl. Phys. B</i> <b>107</b>, 997 (2012).</p> | <p>[7] J. Ketter, T. Eronen, M. Höcker, S. Streubel, and K. Blaum, First-order perturbative calculation of the frequency-shifts caused by static cylindrically-symmetric electric and magnetic imperfections of a Penning trap, <i>Int. J. Mass Spectrom.</i> <b>358</b>, 1 (2014).</p> <p>[8] S. Rau, <i>High-Precision Measurement of the Deuteron's Atomic Mass</i>, Ph.D. thesis, Ruperto-Carola University, Heidelberg (2020).</p> <p>[9] G. Gabrielse, Why Is Sideband Mass Spectrometry Possible with Ions in a Penning Trap?, <i>Phys. Rev. Lett.</i> <b>102</b>, 172501 (2009).</p> <p>[10] H. Häffner, <i>Präzisionsmessung des magnetischen Moments des Elektrons in wasserstoffähnlichem Kohlenstoff</i>, Ph.D. thesis, Johannes Gutenberg-Universität Mainz (2000).</p> <p>[11] X. Feng, M. Charlton, M. Holzscheiter, R. A. Lewis, and Y. Yamazaki, Tank circuit model applied to particles in a Penning trap, <i>J. Appl. Phys.</i> <b>79</b>, 8 (1996).</p> <p>[12] P. W. Anderson, Theory of Flux Creep in Hard Superconductors, <i>Phys. Rev. Lett.</i> <b>9</b>, 309 (1962).</p> <p>[13] J. Ketter, T. Eronen, M. Höcker, M. Schuh, S. Streubel, and K. Blaum, Classical calculation of relativistic frequency-shifts in an ideal Penning trap, <i>Int. J. Mass Spectrom.</i> <b>361</b>, 34 (2014).</p> <p>[14] G. Gabrielse, L. Haarsma, and S. Rolston, Open-endcap</p> |
|---|---|

- Penning traps for high precision experiments, *Int. J. Mass Spectrom.* **88**, 319 (1989).
- [15] K. G. Dyall, I. P. Grant, C. T. Johnson, F. A. Parpia, and E. P. Plummer, GRASP: A general-purpose relativistic atomic structure program, *Comput. Phys. Commun.* **55**, 425 (1989).
- [16] F. A. Parpia and A. K. Mohanty, Relativistic basis-set calculations for atoms with Fermi nuclei, *Phys. Rev. A* **46**, 3735 (1992).
- [17] I. Angeli and K. P. Marinova, Table of experimental nuclear ground state charge radii: An update, *At. Data Nucl. Data Tables* **99**, 69 (2013).
- [18] I. P. Grant, *Relativistic Quantum Theory of Atoms and Molecules*, Springer Series on Atomic, Optical, and Plasma Physics, Vol. 40 (Springer, 2007).
- [19] C. Froese Fischer, G. Gaigalas, P. Jönsson, and J. Bieroń, GRASP2018—A Fortran 95 version of the General Relativistic Atomic Structure Package, *Comput. Phys. Commun.* **237**, 184 (2019).
- [20] P. Jönsson, G. Gaigalas, C. Froese Fischer, J. Bieroń, I. P. Grant, T. Brage, J. Ekman, M. Godefroid, J. Grumer, J. Li, and W. Li, GRASP Manual for Users, *Atoms* **11**, 68 (2023).
- [21] P. Jönsson, M. Godefroid, G. Gaigalas, J. Ekman, J. Grumer, W. Li, J. Li, T. Brage, I. P. Grant, J. Bieroń, and C. Froese Fischer, An Introduction to Relativistic Theory as Implemented in GRASP, *Atoms* **11**, 7 (2023).
- [22] A. V. Malyshev, A. V. Volotka, D. A. Glazov, I. I. Tupitsyn, V. M. Shabaev, and G. Plunien, QED calculation of the ground-state energy of berylliumlike ions, *Phys. Rev. A* **90**, 062517 (2014).
- [23] A. V. Malyshev, D. A. Glazov, Y. S. Kozhedub, I. S. Anisimova, M. Y. Kaygorodov, V. M. Shabaev, and I. I. Tupitsyn, Ab initio Calculations of Energy Levels in Be-Like Xenon: Strong Interference between Electron-Correlation and QED Effects, *Phys. Rev. Lett.* **126**, 183001 (2021).
- [24] C. Lyu, B. Sikora, Z. Harman, and C. H. Keitel, Extreme field calculations for Penning ion traps and corresponding strong laser field scenarios, *Mol. Phys.* , e2252105 (2023).

## 4.3 Observation of a low-lying metastable electronic state in highly charged lead by Penning-trap mass spectrometry

In this letter the energy of a metastable electronic state in  $\text{Pb}^{41+}$  was measured and calculated. The article has been published in *Physical Review Letters*.

**Authors:** [Kathrin Kromer](#), Chunhai Lyu, Menno Door, Pavel Filianin, Zoltán Harman, Jost Herkenhoff, Paul Indelicato, Christoph H. Keitel, Daniel Lange, Yuri N. Novikov, Christoph Schweiger, Sergey Eliseev, and Klaus Blaum

**Publication status:** Published 29 November 2023

**Journal reference:** Kromer *et al.* *Phys. Rev. Lett.* **131**, 223002

**Digital Object Identifier:** [10.1103/PhysRevLett.131.223002](https://doi.org/10.1103/PhysRevLett.131.223002)

**Authors' contributions:** [KK](#), MD, PF, CS, and SE conducted the experiment and took the data. [KK](#), MD, and SE analyzed the data. CL, ZH, and PI calculated the theoretical values. CL wrote the theory part of the manuscript and the part about future applications in XUV spectroscopy. [KK](#) wrote the remaining parts: the introduction, the experimental part, analysis and discussion and prepared all figures. All authors took part in the critical review before and after submission.

**Abstract:** Highly charged ions (HCIs) offer many opportunities for next-generation clock research due to the vast landscape of available electronic transitions in different charge states. The development of XUV frequency combs has enabled the search for clock transitions based on shorter wavelengths in HCIs. However, without initial knowledge of the energy of the clock states, these narrow transitions are difficult to be probed by lasers. In this Letter, we provide experimental observation and theoretical calculation of a long-lived electronic state in Nb-like  $\text{Pb}^{41+}$  which could be used as a clock state. With the mass spectrometer PENTATRAN, the excitation energy of this metastable state is directly determined as a mass difference at an energy of 31.2(8) eV, corresponding to one of the most precise relative mass determinations to date with a fractional uncertainty of  $4 \times 10^{-12}$ . This experimental result agrees within  $1 \sigma$  with two partially different *ab initio* multi-configuration Dirac-Hartree-Fock calculations of 31.68(13) eV and 31.76(35) eV, respectively. With a calculated lifetime of 26.5(5.3) days, the transition from this metastable state to the ground state bears a quality factor of  $1.1 \times 10^{23}$  and allows for the construction of a HCI clock with a fractional frequency instability of  $< 10^{-19}/\sqrt{\tau}$ .

## Observation of a Low-Lying Metastable Electronic State in Highly Charged Lead by Penning-Trap Mass Spectrometry

Kathrin Kromer<sup>1,\*</sup>, Chunhai Lyu<sup>1</sup>, Menno Door<sup>1</sup>, Pavel Filianin<sup>1</sup>, Zoltán Harman<sup>1</sup>, Jost Herkenhoff<sup>1</sup>, Paul Indelicato<sup>2</sup>, Christoph H. Keitel<sup>1</sup>, Daniel Lange<sup>1</sup>, Yuri N. Novikov<sup>3,4</sup>, Christoph Schweiger<sup>1</sup>, Sergey Eliseev<sup>1</sup>, and Klaus Blaum<sup>1</sup>

<sup>1</sup>Max-Planck-Institut für Kernphysik, 69117 Heidelberg, Germany

<sup>2</sup>Laboratoire Kastler Brossel, Sorbonne Université, CNRS, ENS-PSL Research University, Collège de France, Paris, France

<sup>3</sup>Department of Physics, St Petersburg State University, St. Petersburg 198504, Russia

<sup>4</sup>NRC “Kurchatov Institute”-Petersburg Nuclear Physics Institute, Gatchina 188300, Russia

 (Received 21 April 2023; revised 9 October 2023; accepted 17 October 2023; published 29 November 2023)

Highly charged ions (HCIs) offer many opportunities for next-generation clock research due to the vast landscape of available electronic transitions in different charge states. The development of extreme ultraviolet frequency combs has enabled the search for clock transitions based on shorter wavelengths in HCIs. However, without initial knowledge of the energy of the clock states, these narrow transitions are difficult to be probed by lasers. In this Letter, we provide experimental observation and theoretical calculation of a long-lived electronic state in Nb-like Pb<sup>41+</sup> that could be used as a clock state. With the mass spectrometer PENTATRAN, the excitation energy of this metastable state is directly determined as a mass difference at an energy of 31.2(8) eV, corresponding to one of the most precise relative mass determinations to date with a fractional uncertainty of  $4 \times 10^{-12}$ . This experimental result agrees within  $1\sigma$  with two partially different *ab initio* multiconfiguration Dirac-Hartree-Fock calculations of 31.68(13) eV and 31.76(35) eV, respectively. With a calculated lifetime of 26.5(5.3) days, the transition from this metastable state to the ground state bears a quality factor of  $1.1 \times 10^{23}$  and allows for the construction of a HCI clock with a fractional frequency instability of  $< 10^{-19}/\sqrt{\tau}$ .

DOI: [10.1103/PhysRevLett.131.223002](https://doi.org/10.1103/PhysRevLett.131.223002)

The invention of the frequency comb [1,2] opened up the possibility to use optical transitions as frequency standards, called optical atomic clocks. These clocks, using single ions in Paul traps [3,4] or arrays of atoms in optical lattices [5,6], have reached incredible fractional frequency instabilities of below  $2 \times 10^{-16}/\sqrt{\tau}$  for individual optical clocks [7],  $\tau$  being the averaging time, and  $5 \times 10^{-18}/\sqrt{\tau}$  for spatially separated atomic ensembles [6]. This extremely high precision not only provides a standard for frequency measurements, it also enables the search for physics beyond the standard model, such as temporal or spatial variation of fundamental constants [8,9] or violations of Einstein’s equivalence principle through tests of local position invariance [10]. It is therefore of great importance to push this precision frontier even further to be able to limit the possible size of these effects. One way of achieving this

would be to go to strongly forbidden atomic transitions in the extreme ultraviolet (XUV) region.

With a new generation of frequency combs now spanning more than the optical range and reaching up to the XUV [11–16], research into matching transitions has intensified. Transitions in highly charged ions (HCIs) have become of interest for a new generation of clocks [17–19]. Though these clocks usually do not hold appropriate transitions for laser cooling and state readout, they can be interrogated via quantum logic spectroscopy [20], which has been demonstrated in highly charged Ar<sup>13+</sup> with a fractional instability of  $3 \times 10^{-14}/\sqrt{\tau}$  for an optical clock transition [21].

HCI transitions are widely shielded from field-induced frequency shifts. The remaining electrons of HCIs are bound orders of magnitude stronger than the corresponding electrons in a neutral atom or singly charged ion, making the influence of external fields as well as blackbody radiation minimal [22,23]. However, the frequency of a coherent laser usually has a limited tuning range, and a metastable state has a narrow transition. Without initial knowledge of the energy of the clock state, it is difficult to design a direct laser-spectroscopy experiment of the clock transition. High-precision mass spectrometry thus provides

---

Published by the American Physical Society under the terms of the Creative Commons Attribution 4.0 International license. Further distribution of this work must maintain attribution to the author(s) and the published article’s title, journal citation, and DOI. Open access publication funded by the Max Planck Society.



an alternative approach to infer the energy of a long-lived clock state and, at the same time, to test state-of-the-art theoretical calculations.

In this Letter, with the Penning-trap mass spectrometer PENTATRAP and the multiconfiguration Dirac-Hartree-Fock (MCDHF) theory, we present the experimental observation and the theoretical calculation of a low-lying metastable electronic state in Nb-like  $^{208}\text{Pb}^{41+}$ . The excitation energy is determined to be around 31 eV with sub-eV uncertainty. Unlike previous mass-spectroscopy measurements of a metastable state around 200 eV in  $\text{Re}^{29+}$  [24], this metastable state can be effectively probed via available XUV frequency combs, rendering it more feasible to construct an XUV clock. With a calculated lifetime of 26.5(5.3) days, such a clock bears a quality factor of  $1.1 \times 10^{23}$ . Assuming a clock interrogation linewidth of 1 mHz available for optical lasers [25], such an XUV clock could achieve a fractional frequency instability of around  $4 \times 10^{-20}/\sqrt{\tau}$ . Similar clock states can also be scaled to higher and lower transition energies by employing different elements of the Nb-like isoelectronic sequence [19].

To produce highly charged ions, a Heidelberg compact electron beam ion trap (EBIT) [26] equipped with an in-trap laser desorption setup is used [27]. Inside this tabletop-sized EBIT, a few-keV electron beam is produced and then guided and compressed by permanent magnets to ionize atoms and ions to high charge states by electron impact ionization. A target made of  $^{208}\text{Pb}$ , positioned next to the trap center, is used as a source of neutral material. By aiming a pulsed Nd:YAG laser with a pulse energy and duration of about 0.5 mJ and 8 ns, respectively, at the target, a small amount of target material is evaporated into the trap region. In a process called “charge breeding,” the ions remain trapped inside the central drift tube, which is set to a depth of 20 V compared to the neighboring drift tubes of the EBIT and reach higher and higher charge states by electron impact ionization until they arrive at an equilibrium charge distribution. During electron-ion interaction processes inside the EBIT’s ion plasma, such as electron impact excitation or radiative or dielectronic recombination, some of the ions’ electrons become highly excited [28]. After the short-lived excited states decay cascadingly, a fraction of the HCIs will remain in long-lived states for an extended period of time. This fortuitous population of the metastable state allows us to measure the excitation energy of the metastable state without having to actively drive the transition by using mass measurements. This method does not require prior knowledge of the state energies, which makes these measurements independent of theory or other experiments.

The HCIs are extracted from the EBIT and slowed down from 4 keV/ $q$  to a few eV/ $q$  to be able to trap them in a cryogenic Penning trap. The ion transport at the experiment PENTATRAP works via an electrostatic beamline in combination with a Bradbury Nielson gate [29] for charge

state selection. The ions are then decelerated by a set of two pulsed drift tubes, one of which is situated in the room temperature region (deceleration down to  $\approx 200$  eV/ $q$ ) and a second one in the cryogenic part of the beamline (down to a few eV/ $q$ ) and ultimately captured in the first Penning trap. For an overview of the beamline setup, see Ref. [30].

To determine mass ratios of stable or long-lived highly charged ions, five identical, aligned, cylindrical Penning traps are used in PENTATRAP’s trap tower [see Fig. 1(a)] [31,32]. The trap tower opens the possibility to conduct simultaneous measurements on two ions stored in Traps 2 and 3 while having two more traps for ion storage. The fifth trap is currently not in use. The measurement principle is based on a measurement of the frequencies of the ions’ three Penning-trap eigenmotions: the modified cyclotron frequency  $\nu_+$ , the axial frequency  $\nu_z$ , and the magnetron frequency  $\nu_-$  and calculating the free cyclotron frequency  $\nu_c = qB/(2\pi m)$  by applying the invariance theorem [33]

$$\nu_c = \sqrt{\nu_+^2 + \nu_z^2 + \nu_-^2}. \quad (1)$$

The free cyclotron frequency  $\nu_c$  is inversely proportional to the mass  $m$  of the ion and proportional to the exactly known charge  $q$  of the ion and the magnetic field  $B$ . In order to achieve a precise determination of the mass of the ion in the excited electronic state  $m_{\text{exc}}$ , the cyclotron frequency of an ion in the ground state  $\nu_{c,g}$  is measured alternately to that of an ion in the excited state  $\nu_{c,\text{exc}}$  in each of the measurement traps. When determining the ratio  $R = \nu_{c,g}/\nu_{c,\text{exc}}$  for Trap 2 or Trap 3 of the two cyclotron frequencies, the magnetic field, being the least precisely known quantity, cancels out to first order and the identical charge of both ions drops out of the ratio. The mass difference  $\Delta m$  between the ion in the ground state  $m_g$  and the excited state  $m_{\text{exc}}$  can then be determined with

$$\Delta m = m_{\text{exc}} - m_g = m_g(R - 1). \quad (2)$$

The individual ions in each measurement trap [see Fig. 1(a)] are detected nondestructively using the Fourier-transform ion-cyclotron-resonance technique [34]. This well-established method uses the ion’s image current, which is converted into a measurable voltage drop across a resonant tank circuit at cryogenic temperatures. When the cryogenic tank circuit is connected to an axially offset electrode, one can reduce the amplitude of the axial motion by thermalizing it, and measure its frequency as a “dip” in the resonance curve [34]. By coupling the modified cyclotron or the magnetron motion to the axial motion, the coupled motion is cooled and its frequency can be measured using the double-dip technique [35]. This technique is applied to determine the magnetron frequency and for estimating frequencies and coupling pulse times for the phase-sensitive pulse and phase (PnP) method used in the main measurements [36]. A PnP cycle works as follows: in

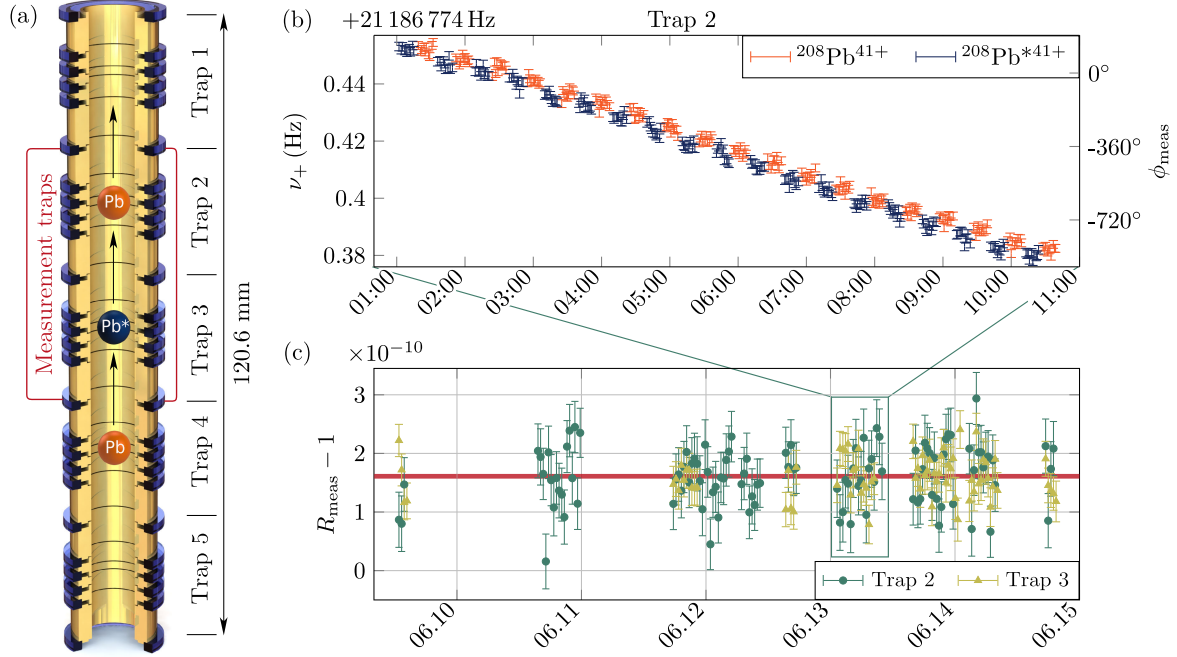


FIG. 1. (a) Schematic drawing of the Penning-trap tower with three ions in Configuration 1. The ion transport to Configuration 2 is implied by arrows. The phase measurements are carried out in Traps 2 and 3. Traps 1 and 4 are utilized as storage traps and Trap 5 is currently not in use. (b) Example of  $\nu_+$  data from a measurement in Trap 2 with  $^{208}\text{Pb}^{41+}$  ions, one being in the ground state (orange) and one in the metastable state (blue). On the left y axis, the resulting frequency is shown while on the right y axis, the unwrapped, measured phase  $\phi_{\text{meas}}$  is given. When combining the averaged modified cyclotron frequency with the axial and magnetron frequencies [see Eq. (1)], one can calculate the cyclotron frequencies and their ratios  $R$  plotted below in subfigure (c). This plot shows the ratios of all relevant measurement runs in both traps. The red line gives the average and its width corresponds to the combined statistical and systematic error band.

the beginning, the cyclotron motion is excited using a dipolar radio frequency (rf) pulse to set a specific starting phase; then the ion's cyclotron oscillation is left to evolve freely for a well-known time  $t_{\text{acc}}$ , called phase accumulation time. The energy and phase information of the cyclotron mode is then coupled to the axial mode using a  $\pi$  pulse at the sideband frequency  $\nu_{\text{rf}} = \nu_+ - \nu_z$ . Subsequently, the cyclotron phase information can be read out using the axial image-current detection system. With this method, one can distinguish between the ground state and low-lying metastable state in  $^{208}\text{Pb}^{41+}$  (see Fig. 2). At a phase accumulation time of  $t_{\text{acc}} = 40$  s the phase difference between metastable and ground state of about  $49^\circ$  at  $\nu_+ \approx 21.2$  MHz exceeds the phase stability of about  $12^\circ$  [see Fig. 1(b)].

Once there are three ions loaded and identified in the alternating configuration shown in Fig. 1(a), the PnP measurement loop is started. In addition to the prior mentioned phase measurement, this also includes an axial frequency measurement during the phase accumulation time of the modified cyclotron frequency and a single magnetron frequency measurement in the preparation phase of the measurement. During the continuous PnP measurement loop, the ions are moved up or down every 10 measurement points to alternate between Configurations 1

and 2 effectively swapping the ions in each measurement trap from the ion in the ground state to the ion in the excited state or vice versa (see Fig. 1). For further information on the measurement procedure, see Refs. [24,30,37,38].

In the analysis, all three measured eigenfrequencies are combined, following Eq. (1), and the cyclotron frequency

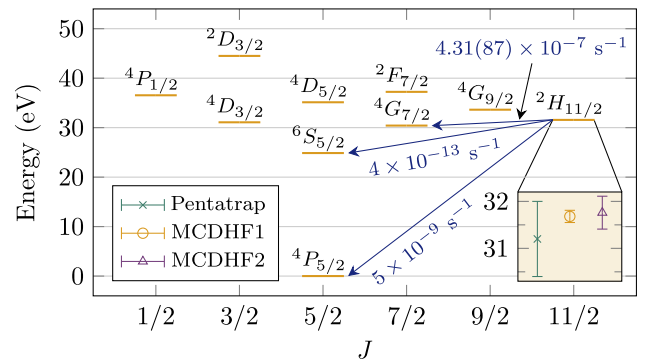


FIG. 2. Lowest energy levels of the Nb-like  $\text{Pb}^{41+}$  ion. The metastable  $[\text{Kr}]4d^5 2H_{11/2}$  state lies at around 31 eV above the  $[\text{Kr}]4d^5 4P_{5/2}$  state. It decays mainly via an  $E2$  transition to the short-lived state  $[\text{Kr}]4d^5 4G_{7/2}$ . The metastable state has a lifetime of 26.5(5.3) days.

ratio is formed by interpolation, whereby one of the ion's block of 10 cyclotron frequency measurements is averaged and interpolated to the time of the other ion's averaged cyclotron frequency measurement. In Fig. 1(b) it is clearly visible that the modified cyclotron frequency  $\nu_+$  drifts downward by  $\delta B/B = -2.3 \times 10^{-10}/h$  due to a loss of magnetic field of the superconducting magnet. With the interpolation, this magnetic field drift is canceled out to first order.

The resulting ratios of both traps can be found in Fig. 1(c). The average ratio of all measurement runs was determined to be  $R_{\text{stat}} - 1 = 1.609(32) \times 10^{-10}$ . Because of the almost identical charge-to-mass ratio of the ion in ground and metastable state, most known systematic effects, such as the image charge shift or the relativistic shift, cancel out to a large extent when forming the frequency ratio. Only one systematic uncertainty of relevant size remains, namely the dip line-shape uncertainty [39]. This systematic originates from the uncertainty of the axial dip frequency relative to the fitted resonator frequency. In Trap 3, the  $Q$  factor of the resonator is substantially larger and thus the dip width is substantially broader than in Trap 2, which increases the uncertainty of the resonator frequency because the center of the resonance spectrum is "covered" by the broad dip. As expected, the fit of the dip in Trap 3 yields a larger systematic error associated with the mismatch of the dip and resonator frequencies connected to the distortion of the dip shape due to the frequency pulling effect. These two effects in Trap 2 and Trap 3 result in an error of  $< 1 \times 10^{-12}$  and  $3.3 \times 10^{-12}$ , respectively. Including this systematic effect, the final experimental mass ratio is determined to be  $R - 1 = 1.61(4) \times 10^{-10}$ . The mass or energy difference of the two states can then be calculated using Eq. (2) to be 31.2(8) eV. This small energy difference was measured as a relative mass measurement against the total mass of the Pb ion of  $\approx 194 \text{ GeV}/c^2$ , reaching a relative precision of  $4 \times 10^{-12}$ .

The level structure and lifetimes of the low-lying states in  $\text{Pb}^{41+}$  (see Fig. 2), are calculated with the *ab initio* multiconfiguration Dirac-Hartree-Fock (MCDHF) and relativistic configuration interaction (RCI) methods in two partially different implementations, one of them being the GRASP2018 code [40–42] (referred to henceforth as MCDHF1) and the second one based on the Multiconfiguration Dirac-Fock with General Matrix Elements code [43] (referred to as MCDHF2). With a ground state of  $[\text{Kr}]4d^5 4P_{5/2}$ , the metastable state is determined to be  $^2H_{11/2}$ .

Within the calculations of MCDHF1, each many-electron atomic state function is expanded as a linear combination of configuration state functions (CSFs) with common total angular momentum ( $J$ ), magnetic ( $M$ ), and parity ( $P$ ) quantum numbers:  $|\Gamma P J M\rangle = \sum_k c_k |\gamma_k P J M\rangle$ . The CSFs  $|\gamma_k P J M\rangle$  are *jj*-coupled Slater determinants of

one-electron orbitals and  $\gamma_k$  summarizes all the remaining information needed to fully define the CSF, i.e., the orbital occupation and coupling of single-electron angular momenta.  $\Gamma$  collectively denotes all the  $\gamma_k$  included in the representation of the atomic state function.

In the calculation of the excitation energy of the  $J = 11/2$  metastable state, the CSF basis set is generated via single and double (SD) excitation of electrons from the  $4s^2 4p^6 4d^5$  reference configurations to high-lying virtual orbitals. After obtaining the radial wave functions from the self-consistent MCDHF calculations under the Dirac-Coulomb Hamiltonian, the RCI method is applied to derive the mixing coefficients  $c_k$  and excitation energies, as well as the approximate corrections arising from the mass shift, quantum electrodynamic (QED) terms, and Breit interaction.

To monitor the convergence of the result, we systematically added and optimized virtual orbitals layer by layer up to  $n = 8$  with all orbital quantum numbers ranging from 0 to  $n - 1$  being included ( $n$  is the principal quantum number). Through extrapolation to  $n = \infty$ , one obtains an energy of 31.672 eV within the calculation of MCDHF1 with  $8.92 \times 10^6$  CSFs, which includes a 837 meV contribution from the Breit interaction, 47.2 meV from the self-energy correction, 0.07 meV from the vacuum polarization, 1.72 meV from the field shift, and 0.24 meV from the mass shift. The RCI calculations based on different radial wave functions lead to a correction of 6 meV. By varying the fine-structure constant in the calculation, this transition is found to have an  $\alpha$ -variation sensitivity of  $K = (\Delta E/E)/(\Delta\alpha/\alpha) = -1.74$ . Considering the 10 times greater transition energy, the absolute frequency change due to  $\alpha$  variations is comparable to other HCI candidates.

Furthermore, to account for the core-core correlations, the CSFs generated via SD excitations from the  $1s$  orbital up to  $5g$  orbital are added to the RCI calculations. This gives rise to a correction of  $-20$  meV to the previous value. Then, through further inclusion of SD excitations from multireference  $\{4s4p^6 4d^6, 4p^6 4d^7, 4s^2 4p^4 4d^7\}$  configurations up to the  $6h$  orbital, the contribution from dominant triple and quadruple electron exchanges is considered in the RCI procedure with  $13.7 \times 10^6$  CSFs. This gives a correction of 14 meV from high-order electron correlations. The final excitation energy is determined to be 31.68(13) eV. The uncertainty is conservatively given as the absolute summation of the corrections from the core-core and high-order correlations, the radial wave function dependence, plus 10% uncertainty from the Breit and QED terms.

The approach of MCDHF2 deviates from the above described calculations in the following way: in contrast to the perturbative approach of MCDHF1, the calculation within MCDHF2 includes the Breit and retardation term of the electron-electron interaction to all order by adding it directly to the many-body Hamiltonian. A smaller set of configurations is used compared to MCDHF1, but

including a full relaxation of all orbitals. Single, double, and triple excitations were limited to excitations from the  $n = 4$  shell:  $4s$ ,  $4p$ ,  $4d$  to  $4d$ ,  $4f$ ,  $5s$ ,  $5p$ ,  $5d$ ,  $6s$ ,  $6p$  with approximately 29 000 configurations for the  ${}^2H_{11/2}$  state and 24 000 configurations for the ground state. For the self-energy screening, two different methods are used [44–46] and more high-order QED corrections are included; however, the contribution of this is minimal for the case of transition energies in  $\text{Pb}^{41+}$ . The MCDHF2 method reaches a final value for the excitation energy of 31.76(35) eV, in excellent agreement with the MCDHF1 result.

While the metastable state decays to the ground state via a magnetic octupole ( $M3$ ) transition under a rate of  $A_1 = 4.95(5) \times 10^{-9} \text{ s}^{-1}$ , its lifetime is mainly determined by the electric quadrupole ( $E2$ ) decay channel to the  $J = 7/2$  state (see Fig. 2). The decay rates were calculated with the MCDHF1 method. Under the above mentioned multireference scheme, we expanded the CSF basis set to  $n = 8$  and obtained a rate of  $5.18 \times 10^{-7} \text{ s}^{-1}$  and  $4.31 \times 10^{-7} \text{ s}^{-1}$  in the Coulomb and Babushkin gauge, respectively. Since both rates show decreasing trends with  $n$  and the rate in the Babushkin gauge is already close to convergent, the value  $A_2 = 4.31(87) \times 10^{-7} \text{ s}^{-1}$  is used to represent the decay rate of this channel. The uncertainty is given as the difference between the rates in the two gauges. As a result, the lifetime of the metastable state is determined to be 26.5(5.3) days.

The resonant photon-excitation cross section [47] from the ground state to this metastable state is calculated to be  $8.3 \times 10^{-14} \text{ cm}^2$  per photon. Current XUV frequency combs at such photon energy would have a repetition rate of 100 MHz and a pulse duration of 24 fs [48]. With proper phase-matching schemes, XUV combs with powers at the mW level are achievable [49]. Assuming an average power of 5 mW per harmonic or 25.5 nW per tooth and a focal size of  $10 \mu\text{m}^2$ , they bear a photon flux of  $5.0 \times 10^{16} \text{ ph/s/cm}^2$  per tooth. Assuming a comb coherence time of 1 s [50], i.e., a tooth width of 160 mHz, the resonant photon flux would be  $2.2 \times 10^{10} \text{ ph/s/cm}^2$ . Thus, one would obtain  $1.8 \times 10^{-3}$  excitations per second (or an effective Rabi frequency of  $\Omega/2\pi = 6.8 \text{ mHz}$ ) at resonance [18], rendering future XUV resonant spectroscopy of this clock state promising. Nevertheless, before direct excitation of the metastable state, further spectroscopy of the nearby fast transitions such as  ${}^4P_{5/2} \rightarrow {}^4G_{7/2}$ ,  ${}^4G_{7/2} \rightarrow {}^4G_{9/2}$ , and  ${}^4G_{9/2} \rightarrow {}^2H_{11/2}$  is necessary to improve the accuracy of the clock transition energy to around 21 kHz. For the quantum logic scheme, however, one needs to be able to drive a sideband coupling in the HCI, whose Rabi frequency is typically smaller by a factor of  $\eta = kz_0$ . Here,  $\eta$  is the Lamb-Dicke parameter,  $k$  the wave number of the laser, and  $z_0$  the spatial spread of the ground state motional wave function along the laser propagation direction [51]. Therefore, in order to realize the full ability of quantum logic, one needs to either increase the laser power or the coherence time of the XUV comb.

We have shown the experimental determination and theoretical calculation of the excitation energy of a low-lying metastable state in  $\text{Pb}^{41+}$ . The metastable  $[\text{Kr}]4d^5 {}^2H_{11/2}$  state and its most probable decay channels including the transition rates, calculated with the MCDHF1 method, are shown in Fig. 2, and the region of interest around the metastable state is enlarged to show the different values of experiment (PENTATRAP) and theory (MCDHF1 and 2). As can be seen, the calculation of MCDHF1 and MCDHF2 agree with the experimental data within  $1\sigma$ . This comparison verifies the theoretical multi-electron correlation studies and excitation energy estimations described in this Letter. It also shows the ability of Penning-trap mass measurements to help in the search for transitions usable in future HCI clocks and to determine their energy at a sub-eV precision.

As described, the energy of the metastable state falls into the range of current XUV combs, allowing resonant spectroscopy of this metastable state using a high flux, high repetition rate XUV comb [16]. The orders-of-magnitude higher transition energy of XUV in comparison to optical clocks could enable the construction of an ultrastable clock with a fractional frequency instability around  $4 \times 10^{-20}/\sqrt{\tau}$ .

This work comprises parts of the Ph.D. thesis work of K. K. to be submitted to Heidelberg University, Germany. This work is part of and funded by the Max-Planck-Gesellschaft and the DFG (German Research Foundation)—Project-ID 273811115—SFB 1225 ISOQUANT. The project received funding from the European Research Council (ERC) under the European Union’s Horizon 2020 research and innovation programme under grant agreement No. 832848—FunI. P. I., Y. N., and K. B. are members of the Allianz Program of the Helmholtz Association, Contract No. EMMI HA-216 “Extremes of Density and Temperature: Cosmic Matter in the Laboratory.” Furthermore, we acknowledge funding and support by the International Max-Planck Research School for Precision Tests of Fundamental Symmetries and the Max Planck, RIKEN, PTB Center for Time, Constants and Fundamental Symmetries. The authors thank J. R. Crespo López-Urrutia and his team for insightful discussions and support. P. I. acknowledges support from CNRS and from the “Programme Hubert Curien PESSOA 47863UE.”

\*Corresponding author: kromer@mpi-hd.mpg.de

- [1] J. L. Hall, Nobel Lecture: Defining and measuring optical frequencies, *Rev. Mod. Phys.* **78**, 1279 (2006).
- [2] T. W. Hänsch, Nobel Lecture: Passion for precision, *Rev. Mod. Phys.* **78**, 1297 (2006).
- [3] N. Huntemann, C. Sanner, B. Lipphardt, C. Tamm, and E. Peik, Single-ion atomic clock with  $3 \times 10^{-18}$  systematic uncertainty, *Phys. Rev. Lett.* **116**, 063001 (2016).

- [4] S. Brewer, J.-S. Chen, A. Hankin, E. Clements, C. Chou, D. Wineland, D. Hume, and D. Leibbrandt,  $^{27}\text{Al}^+$  quantum-logic clock with a systematic uncertainty below  $10^{-18}$ , *Phys. Rev. Lett.* **123**, 033201 (2019).
- [5] X. Zheng, J. Dolde, V. Lochab, B. N. Merriman, H. Li, and S. Kolkowitz, Differential clock comparisons with a multiplexed optical lattice clock, *Nature (London)* **602**, 425 (2022).
- [6] T. Bothwell, C. J. Kennedy, A. Aeppli, D. Kedar, J. M. Robinson, E. Oelker, A. Staron, and J. Ye, Resolving the gravitational redshift across a millimetre-scale atomic sample, *Nature (London)* **602**, 420 (2022).
- [7] E. R. Clements, M. E. Kim, K. Cui, A. M. Hankin, S. M. Brewer, J. Valencia, J.-S. Chen, C.-W. Chou, D. R. Leibbrandt, and D. B. Hume, Lifetime-limited interrogation of two independent  $^{27}\text{Al}^+$  clocks using correlation spectroscopy, *Phys. Rev. Lett.* **125**, 243602 (2020).
- [8] J. D. Prestage, R. L. Tjoelker, and L. Maleki, Atomic clocks and variations of the fine structure constant, *Phys. Rev. Lett.* **74**, 3511 (1995).
- [9] R. Godun, P. Nisbet-Jones, J. Jones, S. King, L. Johnson, H. Margolis, K. Szymaniec, S. Lea, K. Bongs, and P. Gill, Frequency ratio of two optical clock transitions in  $^{171}\text{Yb}^+$  and constraints on the time variation of fundamental constants, *Phys. Rev. Lett.* **113**, 210801 (2014).
- [10] R. Lange, N. Huntemann, J. M. Rahm, C. Sanner, H. Shao, B. Lipphardt, Chr. Tamm, S. Weyers, and E. Peik, Improved limits for violations of local position invariance from atomic clock comparisons, *Phys. Rev. Lett.* **126**, 011102 (2021).
- [11] C. Gohle, T. Udem, M. Herrmann, J. Rauschenberger, R. Holzwarth, H. A. Schuessler, F. Krausz, and T. W. Hänsch, A frequency comb in the extreme ultraviolet, *Nature (London)* **436**, 234 (2005).
- [12] R. J. Jones, K. D. Moll, M. J. Thorpe, and J. Ye, Phase-coherent frequency combs in the vacuum ultraviolet via high-harmonic generation inside a femtosecond enhancement cavity, *Phys. Rev. Lett.* **94**, 193201 (2005).
- [13] I. Pupeza, C. Zhang, M. Högner, and J. Ye, Extreme-ultraviolet frequency combs for precision metrology and attosecond science, *Nat. Photonics* **15**, 175 (2021).
- [14] H. Carstens, M. Högner, T. Saule, S. Holzberger, N. Lilienfein, A. Guggenmos, C. Jocher, T. Eidam, D. Esser, V. Tosa, V. Pervak, J. Limpert, A. Tünnermann, U. Kleineberg, F. Krausz, and I. Pupeza, High-harmonic generation at 250 MHz with photon energies exceeding 100 eV, *Optica* **3**, 366 (2016).
- [15] I. Pupeza, S. Holzberger, T. Eidam, H. Carstens, D. Esser, J. Weitenberg, P. Rußbüldt, J. Rauschenberger, J. Limpert, T. Udem, A. Tünnermann, T. W. Hänsch, A. Apolonski, F. Krausz, and E. Fill, Compact high-repetition-rate source of coherent 100 eV radiation, *Nat. Photonics* **7**, 608 (2013).
- [16] T. Saule, S. Heinrich, J. Schötz, N. Lilienfein, M. Högner, O. deVries, M. Plötner, J. Weitenberg, D. Esser, J. Schulte, P. Russbüldt, J. Limpert, M. F. Kling, U. Kleineberg, and I. Pupeza, High-flux ultrafast extreme-ultraviolet photoemission spectroscopy at 18.4 MHz pulse repetition rate, *Nat. Commun.* **10**, 458 (2019).
- [17] J. R. Crespo López-Urrutia, Frequency metrology using highly charged ions, *J. Phys. Conf. Ser.* **723**, 012052 (2016).
- [18] C. Lyu, S. M. Cavaletto, C. H. Keitel, and Z. Harman, Interrogating the temporal coherence of EUV frequency combs with highly charged ions, *Phys. Rev. Lett.* **125**, 093201 (2020).
- [19] C. Lyu, Z. Harman, and C. H. Keitel, Ultrastable optical, XUV and soft-x-ray clock transitions in open-shell highly charged ions, [arXiv:2305.09603](https://arxiv.org/abs/2305.09603).
- [20] P. Micke, T. Leopold, S. A. King, E. Benkler, L. J. Spieß, L. Schmöger, M. Schwarz, J. R. Crespo López-Urrutia, and P. O. Schmidt, Coherent laser spectroscopy of highly charged ions using quantum logic, *Nature (London)* **578**, 60 (2020).
- [21] S. A. King, L. J. Spieß, P. Micke, A. Wilzewski, T. Leopold, E. Benkler, R. Lange, N. Huntemann, A. Surzhykov, V. A. Yerokhin, J. R. Crespo López-Urrutia, and P. O. Schmidt, An optical atomic clock based on a highly charged ion, *Nature (London)* **611**, 43 (2022).
- [22] M. G. Kozlov, M. S. Safronova, J. R. Crespo López-Urrutia, and P. O. Schmidt, Highly charged ions: Optical clocks and applications in fundamental physics, *Rev. Mod. Phys.* **90**, 045005 (2018).
- [23] V. I. Yudin, A. V. Taichenachev, and A. Derevianko, Magnetic-dipole transitions in highly charged ions as a basis of ultraprecise optical clocks, *Phys. Rev. Lett.* **113**, 233003 (2014).
- [24] R. X. Schüssler, H. Bekker, M. Braß, H. Cakir, J. R. Crespo López-Urrutia, M. Door, P. Filianin, Z. Harman, M. W. Haverkort, W. J. Huang, P. Indelicato, C. H. Keitel, C. M. König, K. Kromer, M. Müller, Y. N. Novikov, A. Rischka, C. Schweiger, S. Sturm, S. Ulmer, S. Eliseev, and K. Blaum, Detection of metastable electronic states by Penning trap mass spectrometry, *Nature (London)* **581**, 42 (2020).
- [25] D. Matei, T. Legero, S. Häfner, C. Grebing, R. Weyrich, W. Zhang, L. Sonderhouse, J. Robinson, J. Ye, F. Riehle, and U. Sterr, 1.5  $\mu\text{m}$  lasers with Sub-10 mHz linewidth, *Phys. Rev. Lett.* **118**, 263202 (2017).
- [26] P. Micke, S. Kühn, L. Buchauer, J. R. Harries, T. M. Bücking, K. Blaum, A. Cieluch, A. Egl, D. Hollain, S. Kraemer, T. Pfeifer, P. O. Schmidt, R. X. Schüssler, Ch. Schweiger, T. Stöhlker, S. Sturm, R. N. Wolf, S. Bernitt, and J. R. Crespo López-Urrutia, The Heidelberg compact electron beam ion traps, *Rev. Sci. Instrum.* **89**, 063109 (2018).
- [27] Ch. Schweiger, C. M. König, J. R. Crespo López-Urrutia, M. Door, H. Dorrer, Ch. E. Düllmann, S. Eliseev, P. Filianin, W. Huang, K. Kromer, P. Micke, M. Müller, D. Renisch, A. Rischka, R. X. Schüssler, and K. Blaum, Production of highly charged ions of rare species by laser-induced desorption inside an electron beam ion trap, *Rev. Sci. Instrum.* **90**, 123201 (2019).
- [28] H. S. W. Massey and D. R. Bates, The properties of neutral and ionized atomic oxygen and their influence on the upper atmosphere, *Rep. Prog. Phys.* **9**, 62 (1942).
- [29] N. E. Bradbury and R. A. Nielsen, Absolute values of the electron mobility in hydrogen, *Phys. Rev.* **49**, 388 (1936).
- [30] K. Kromer, C. Lyu, M. Door, P. Filianin, Z. Harman, J. Herkenhoff, W. Huang, C. H. Keitel, D. Lange, Y. N. Novikov, C. Schweiger, S. Eliseev, and K. Blaum, High-precision mass measurement of doubly magic  $^{208}\text{Pb}$ , *Eur. Phys. J. A* **58**, 202 (2022).

- [31] J. Repp, C. Böhm, J. R. Crespo López-Urrutia, A. Dörr, S. Eliseev, S. George, M. Goncharov, Y. N. Novikov, C. Roux, S. Sturm, S. Ulmer, and K. Blaum, PENTATRAP: A novel cryogenic multi-Penning-trap experiment for high-precision mass measurements on highly charged ions, *Appl. Phys. B* **107**, 983 (2012).
- [32] C. Roux, C. Böhm, A. Dörr, S. Eliseev, S. George, M. Goncharov, Y. N. Novikov, J. Repp, S. Sturm, S. Ulmer, and K. Blaum, The trap design of PENTATRAP, *Appl. Phys. B* **107**, 997 (2012).
- [33] L. S. Brown and G. Gabrielse, Precision spectroscopy of a charged particle in an imperfect Penning trap, *Phys. Rev. A* **25**, 2423 (1982).
- [34] X. Feng, M. Charlton, M. Holzscheiter, R. A. Lewis, and Y. Yamazaki, Tank circuit model applied to particles in a Penning trap, *J. Appl. Phys.* **79**, 8 (1996).
- [35] E. A. Cornell, R. M. Weisskoff, K. R. Boyce, and D. E. Pritchard, Mode coupling in a Penning trap:  $\pi$  pulses and a classical avoided crossing, *Phys. Rev. A* **41**, 312 (1990).
- [36] E. A. Cornell, R. M. Weisskoff, K. R. Boyce, R. W. Flanagan, G. P. Lafyatis, and D. E. Pritchard, Single-ion cyclotron resonance measurement of  $M(\text{CO}^+)/M(\text{N}_2^+)$ , *Phys. Rev. Lett.* **63**, 1674 (1989).
- [37] A. Rischka, H. Cakir, M. Door, P. Filianin, Z. Harman, W. Huang, P. Indelicato, C. Keitel, C. König, K. Kromer, M. Müller, Y. Novikov, R. Schüssler, C. Schweiger, S. Eliseev, and K. Blaum, Mass-difference measurements on heavy nuclides with an  $\text{eV}/c^2$  accuracy in the PENTATRAP spectrometer, *Phys. Rev. Lett.* **124**, 113001 (2020).
- [38] P. Filianin, C. Lyu, M. Door, K. Blaum, W. Huang, M. Haverkort, P. Indelicato, C. Keitel, K. Kromer, D. Lange, Y. Novikov, A. Rischka, R. Schüssler, C. Schweiger, S. Sturm, S. Ulmer, Z. Harman, and S. Eliseev, Direct  $Q$ -value determination of the  $\beta^-$  decay of  $^{187}\text{Re}$ , *Phys. Rev. Lett.* **127**, 072502 (2021).
- [39] S. Rau, F. Heiße, F. Köhler-Langes, S. Sasidharan, R. Haas, D. Renisch, C. E. Düllmann, W. Quint, S. Sturm, and K. Blaum, Penning trap mass measurements of the deuteron and the  $\text{HD}^+$  molecular ion, *Nature (London)* **585**, 43 (2020).
- [40] I. P. Grant, Relativistic calculation of atomic structures, *Adv. Phys.* **19**, 747 (1970).
- [41] J. P. Desclaux, D. F. Mayers, and F. O'Brien, Relativistic atomic wave functions, *J. Phys. B* **4**, 631 (1971).
- [42] C. F. Fischer, G. Gaigalas, P. Jönsson, and J. Bieroń, GRASP2018—a fortran 95 version of the general relativistic atomic structure package, *Comput. Phys. Commun.* **237**, 184 (2019).
- [43] P. Indelicato and J. Desclaux, MCDFGME: A multiconfiguration Dirac-Fock and general matrix elements program (2005), <http://www.lkb.upmc.fr/metrologysimplesystems/mdfgme-a-general-purpose-multiconfiguration-dirac-foc-program/>.
- [44] P. Indelicato, O. Gorveix, and J. P. Desclaux, Multiconfigurational Dirac-Fock studies of two-electron ions. II. Radiative corrections and comparison with experiment, *J. Phys. B* **20**, 651 (1987).
- [45] P. Indelicato and J. P. Desclaux, Multiconfiguration Dirac-Fock calculations of transition energies with QED corrections in three-electron ions, *Phys. Rev. A* **42**, 5139 (1990).
- [46] V. M. Shabaev, I. I. Tupitsyn, and V. A. Yerokhin, Model operator approach to the Lamb shift calculations in relativistic many-electron atoms, *Phys. Rev. A* **88**, 012513 (2013).
- [47] C. J. Foot, *Atomic Physics* (Oxford University Press, Oxford, 2004), Vol. 7.
- [48] J. Nauta, J.-H. Oelmann, A. Borodin, A. Ackermann, P. Knauer, I. S. Muhammad, R. Pappenberger, T. Pfeifer, and J. R. C. López-Urrutia, XUV frequency comb production with an astigmatism-compensated enhancement cavity, *Opt. Express* **29**, 2624 (2021).
- [49] G. Porat, C. M. Heyl, S. B. Schoun, C. Benko, N. Dörre, K. L. Corwin, and J. Ye, Phase-matched extreme-ultraviolet frequency-comb generation, *Nat. Photonics* **12**, 387 (2018).
- [50] C. Benko, T. K. Allison, A. Cingöz, L. Hua, F. Labaye, D. C. Yost, and J. Ye, Extreme ultraviolet radiation with coherence time greater than 1 s, *Nat. Photonics* **8**, 530 (2014).
- [51] D. Wineland, C. Monroe, W. Itano, D. Leibfried, B. King, and D. Meekhof, Experimental issues in coherent quantum-state manipulation of trapped atomic ions, *J. Res. Natl. Inst. Stand. Technol.* **103**, 259 (1998).

# 5 Discussion

The presented publications in [Chap. 4](#) have shown the level of precision that mass measurements at PENTATRAP can achieve, including the most precise mass determination at the time of publication. In the following chapter, I will discuss the limitations and possible improvements for future measurements.

## 5.1 The mass of lead-208

The determination of the mass of lead-208 described in the publication in [Sec. 4.1](#) reached a relative mass uncertainty of  $7 \times 10^{-11}$ . This was an improvement of almost two orders of magnitude compared to the literature value [[Huan 21](#), [Wang 21](#)]. The Penning-trap mass ratio measurement reached a statistical uncertainty of  $9 \times 10^{-12}$  in just under 31 hours of data taking at which point the total error was dominated by systematic uncertainties. The lead-208 campaign was the first measurement campaign in which we used a pulse shaping (Tuckey window,  $\alpha = 0.5$ ) for the excitation and coupling pulses of PnP. Before the measurement campaign, a systematic investigation showed that the rf pulses applied to the trap electrodes caused an excitation of the resonator due to the abrupt switching of the rf pulses, thereby applying a broadband frequency excitation instead of only the desired sideband frequency. This resulted in a nonlinear response of the readout phase in the axial mode compared to the final phase in the cyclotron mode. This nonlinear effect had a size, peak to peak, of  $8^\circ$  in Trap 2 and  $4^\circ$  in Trap 3 and adds a systematic shift to the cyclotron frequency ratio. With the new pulse shaping, the non-linear phase effect on the ratio was reduced to below  $10^{-12}$ , as described in the Supplemental Material of [Sec. 4.2](#), so that this systematic uncertainty could be set to zero. The remaining systematic effects were the relativistic shift and the image charge shift (ICS), which has the largest contribution. The ICS can be approximately calculated by comparing the trap to an infinitely long cylinder. In this case, an analytical solution exists, see [Eq. \(2.15\)](#). This approximation has been tested to be accurate within

an uncertainty of 5% [Schu 19a]. In order to overcome this systematic limitation for any measurements with a large mass difference between the reference and ion of interest, one would have to measure the ICS explicitly. This was done during the next measurement campaign with a large mass difference  $\Delta m$ : the uranium-238 campaign.

## 5.2 The mass of uranium-238

The statistical uncertainty of  $1.9 \times 10^{-12}$  was achieved by increasing the phase accumulation time to up to 100 s, which was made possible by the exceptional stability of pressure and helium level inside the magnet's bore of  $\delta p < 5 \mu\text{bar/h}$  and  $\delta z_{\text{He}} < 0.5 \text{ mm/h}$ . The stability was improved between the lead and uranium campaigns by adding a 300 l buffer volume to the helium stabilization system. This system stabilizes the pressure of the helium gas and the level of liquid helium by adjusting the gas flow of the evaporating helium from the bore as well as the helium reservoir. By guiding the helium gas into the buffer volume, the pressure can be adjusted more precisely. The system is described in detail in [Risc 14, Krom 19].

The systematics of the uranium measurement campaign were described in detail in the Supplemental Material of Sec. 4.2. The systematic measurements included an extensive determination of the ICS by measuring the magnetron frequency difference. This was done by applying the PnP method to the magnetron mode, which is only possible with careful adjustment of the pulse shaping of the PnP coupling pulse. For a precise investigation of the ICS measurement, the ion pair  $^{238}\text{U}^{47+}$  and  $^{132}\text{Xe}^{26+}$  was an ideal case, since the large mass difference leads to a large magnitude of the ICS. At the same time, the magnetron frequencies of the two ions are very similar due to the similar  $q/m$  ratios, which minimizes all other systematic effects. This way, the ICS was determined with uncertainties of 0.8% in Trap 2 and 1.7% in Trap 3. For future measurement campaigns, especially measurements of heavy ions against carbon, this result is of great importance, since the precision of the ICS will be the limiting factor of mass determinations with a large mass difference  $\Delta m$  between the ion of interest and the reference ion.

Overall, a precision of the mass of uranium-238 of  $6 \times 10^{-11}$  was achieved, purely limited by the theoretical binding energy uncertainty, which is an improvement of two orders of magnitude compared to the current literature value [Huan 21, Wang 21]. The measurements of the mass of lead-208 and uranium-238 elongate the mass backbone into the heavy mass sector and improve the masses of several connected nuclides. In Fig. 5.1 the precision of nuclides from the AME2020 [Huan 21, Wang 21], including the measurements presented in this thesis, are depicted. This can be compared to the status from before this thesis work depicted in Fig. 1.2.



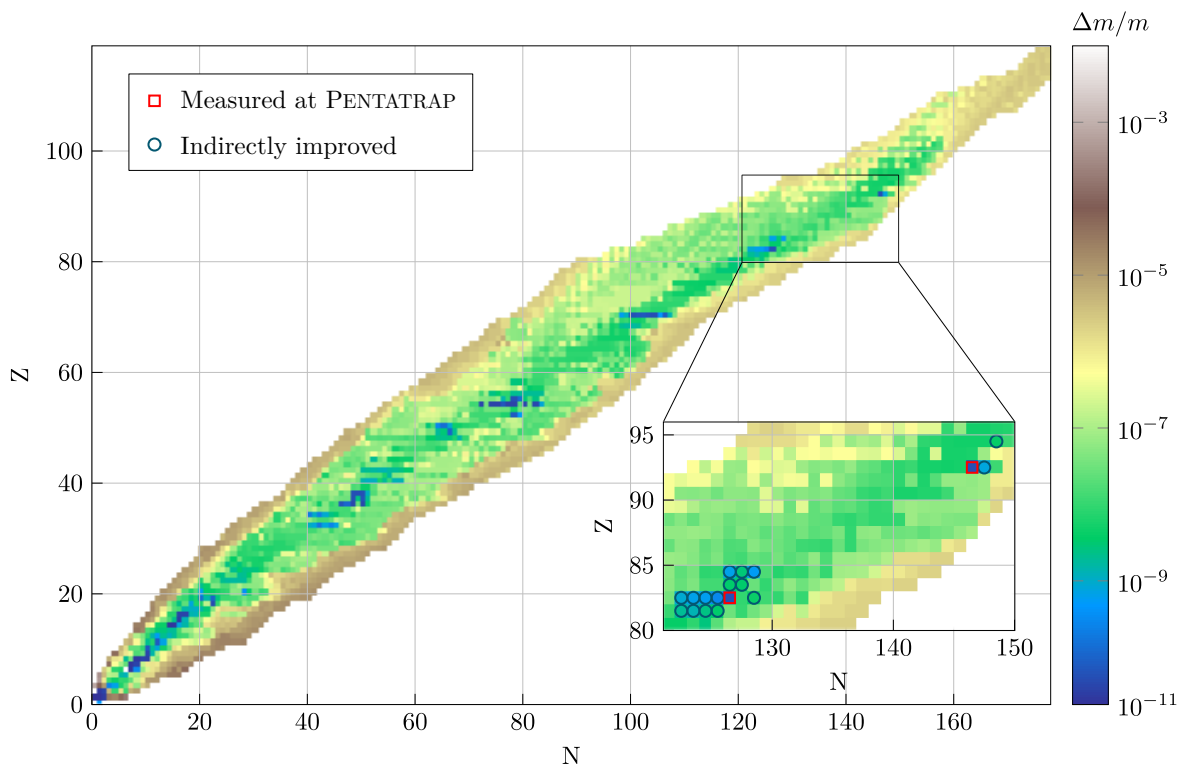


**Figure 5.1:** The nuclide chart indicating by color the mass precision of all nuclides that are listed in the AME2020 [Huan 21, Wang 21] including the improved values acquired during this thesis work. The inset shows the heavy mass region and indicates with red squares lead-208 and uranium-238 which were measured at PENTATRAP. The dark blue circles show the nuclides which were improved indirectly by measuring these two nuclides because they are connected via known decay energies.

### 5.3 Observation of a low-lying electronic state in $^{208}\text{Pb}^{41+}$

Sec. 4.3 describes the observation of a metastable state in  $^{208}\text{Pb}^{41+}$  and a measurement of its energy of 31.2(8) eV. By comparing the result to the theory values of the group of Priv. Doz. Zoltán Harman at the MPIK in Heidelberg and the theory group of Prof. Paul Indelicato at the Laboratoire Kastler Brossel in Paris, the publication signified an important step in benchmarking advanced atomic structure calculations on the path to an HCI clock in the XUV.

#### 5.3.1 Dip-lineshape uncertainty due to a shifting resonator

As described in the paper, there was a systematic uncertainty connected to the axial dip lineshape during the metastable-state measurement campaign. More specifically, the effect

was connected to the position of the center of the resonance spectrum of the tank circuit (further: resonator frequency) in relation to the axial frequency. NPO ceramic capacitors, which are used for coupling the tank circuit to the amplifier, have a small but finite voltage-dependent hysteresis effect of the capacitance that resulted in a small shift of the resonator frequency. This is most likely related to the transport of the ions. During a transport of the ion in the upward direction, the voltage adjustment of the correction electrode, to which the detection system is connected, is different to when the ion is moved downward, see Fig. 5.2. In the metastable-state measurement campaign, the ion in the metastable state

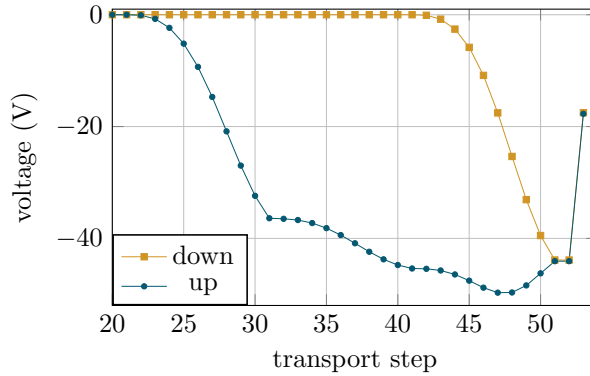


**Figure 5.2:** Voltage steps of the lower correction electrode of Trap 3, to which the axial detection tank circuit is connected. The two lines show the last voltage steps of the transport either in downward direction (yellow squares) or in the upward direction (blue circles). The transport sequence is optimized for an adiabatic transport of the ion.

was always located at the center position of the three ions. This means, it was always moved downwards before measuring its frequencies in Trap 3 and it was always moved upwards before measuring its frequencies in Trap 2. Due to the hysteresis effect, this resulted in a slightly higher resonator frequency of  $\nu_{\text{res}} = 0.15 \text{ Hz}$  in Trap 3 for the ion in the metastable state, compared to when the ion in the ground state was in Trap 3. When combining this with the broad axial dip in Trap 3, which is difficult to fit, the systematic uncertainty on the ratio was estimated to be  $3.3 \times 10^{-12}$ . In Trap 2 the hysteresis effect was an order of magnitude lower and the fit is more reliable due to a smaller dip width and thus does not represent a significant systematic effect.

To avoid this effect in the future, the voltage pattern used to transport the ion can be optimized to minimize the hysteresis and the ion sequence should be varied between A-B-A and B-A-B when reloading the ions. In addition, the transport depth should be just a few volt deep in order not to unnecessarily enlarge the hysteresis effect. The transport depth during the metastable campaign was set to  $U_t = -50 \text{ V}$ .

### 5.3.2 Improvement strategies of the axial frequency determination

The only relevant systematic uncertainty during the metastable-state measurement campaign was the dip line-shape of the axial frequency with the shifting resonator. In the following, two improvement strategies will be discussed. Firstly, a phase-sensitive measurement of the axial frequency will be described, which will omit using a dip fit for the axial frequency completely. Secondly, the possibility of improving the voltage stability and thereby making the axial frequency more stable is introduced. A more stable axial frequency will decrease the "smear-out" effect of the dip that happens when the axial frequency jitters during the collection of dip data.

#### Phase-sensitive measurement of the axial frequency

For an improvement of the axial frequency determination one could move away from the dip-detection technique, since the model based fit routine clearly has its limits once a cyclotron-frequency-ratio determination of a few  $10^{-12}$  is required, as can be seen in [Sec. 4.2](#) and [Sec. 4.3](#). One possibility of moving past a model-based fit would be to perform a phase-sensitive axial frequency measurement. However, since the axial motion is coupled to the tank circuit, any axial excitation will get dissipated and any phase information will eventually be overwritten by the tank-circuits incoherent thermal backaction. As a result, only very short phase measurements on the order of the cooling time constant ( $\approx 35$  ms in Trap 2 and  $\approx 15$  ms in Trap 3) would be possible. In order to measure the axial phase with longer phase accumulation times, one can shift away or suppress the noise spectrum of the axial tank circuit. This can be achieved by detuning the resonator frequency away from the axial frequency with the variable capacitance (varactor) or by using a feedback system e.g. the digital feedback system developed at PENTATRAP [[Herk 21](#)]. With the feedback system one can, among other things, actively suppress the noise of the tank circuit, which results in a detection system that seems colder than its actual temperature. With a suppressed resonance curve, the ion not only cools to a lower temperature but the cooling rate is lower, allowing a longer phase accumulation time.

First tests of axial phase measurements, called axial pulse and phase (APnP) in relation to the well known PnP scheme, showed promising results, see [Fig. 5.3](#). Within this test measurement, the resonator was moved to the side, using the feedback system in order to interact with the ion as little as possible. After the phase accumulation time, the resonator was switched back to where the resonator frequency matches the axial frequency and the axial phase was read out. Besides no longer being model dependent, the APnP technique relies on a coherent phase evolution, which makes it faster compared to the incoherent dip method. With the phase stability shown in [Fig. 5.3](#) for 2.4 s phase accumulation time, the

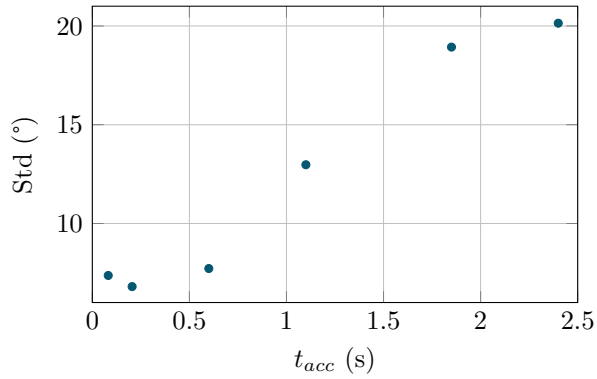


**Figure 5.3:** The stability of the APnP technique with phase accumulation times up to 2.4 s at PENTATRAP, tested using  $^{187}\text{Re}^{29+}$  ions. For each phase accumulation time, 20 phases in Trap 2 were measured and their standard deviations are plotted here.

axial frequency would be determined to  $\approx 3 \times 10^{-8}$  after only a few averages. A fit spectrum reaches a similar precision after a typical averaging time of around 500 s.

When implementing this technique in the usual PnP measurement routine, systematic checks will have to be carried out, as higher axial amplitudes and influence from the shifted resonator will cause perturbations to the ion frequencies [Kett 14]. The axial phase could be measured before and after the PnP  $\nu_+$  measurement and interpolated in time to the PnP measurement, in order to minimize these shifts. Furthermore, it is possible to cool the axial amplitude to smaller radii before the APnP measurement with the feedback system [Herk 21], lowering the necessary axial radius during the APnP cycle.

### Josephson voltage standards

A possibility to improve on the stability of the axial motion is to use Josephson voltage standards [Baue 22] as the voltage source for the ring electrode. This is being explored at PENTATRAP in collaboration with another Penning-trap group at the MPIK, the  $\mu\text{TEx}$  experiment [Dick 24], and with the PTB in Braunschweig [Door 24]. A Josephson junction has two superconducting layers coupled by a thin layer of a normal conducting or insulating material in between them. When applying a drive with a constant microwave frequency, the characteristic current-voltage curve will form regions of constant voltage due to the quantization of the voltage. Using the junction in this region will produce a very stable voltage that can be used as a precision voltage source. In order to reach the voltages necessary for supplying the ring electrode, one can make use of a Josephson array which combines over 100 000 junctions in series. The voltage standard that was employed for the tests was developed at the PTB in Braunschweig and outputs a programmable voltage up to 20 V [Mull 13]. In [Kais 24] the use

of the 20 V array is investigated in order to push the precision of mass-ratio determination below the  $10^{-12}$  level.

### 5.3.3 Further investigation of the clock state $^2H_{11/2}$ in $\text{Pb}^{41+}$

The detection of the metastable state, as shown in [Sec. 4.3](#), benchmarked the theoretical atomic structure calculations described in the paper as well as in [\[Lyu 23a\]](#) for similar open-shell systems. This signified a first major step towards the realization of an XUV clock using HCIs and warrants further investigation of the metastable state. Due to the narrow linewidth of the transition in combination with the available power in XUV frequency combs, further investigation of the transition is necessary before any direct excitation of the metastable state will be possible. As an intermediate step, the line position could be determined more precisely by measuring a succession of more probable transitions, see [Fig. 2](#) in [Sec. 4.3](#):

1.  $^4P_{5/2} \rightarrow ^4G_{7/2}$  transition probability  $1.3 \times 10^5 \text{ s}^{-1}$  (M1, 30.4 eV)
2.  $^4G_{7/2} \rightarrow ^4G_{9/2}$  transition probability  $180 \text{ s}^{-1}$  (M1, 3.33 eV)
3.  $^4G_{9/2} \rightarrow ^2H_{11/2}$  transition probability  $52 \text{ s}^{-1}$  (M1, 2.28 eV)

Theoretical transition energies and probabilities were provided by Chunhai Lyu from the MPIK in Heidelberg and P. Indelicato from the Laboratoire Kastler Brossel, CNRS, Paris, France. A measurement of these nearby levels could be done using emission spectroscopy in an EBIT. Using collisional-radiative modelling, the group around apl. Prof. José Crespo at the MPIK in Heidelberg verified that the mentioned transitions are strong enough to be measurable. With emission spectroscopy, one should be able to determine transition No. 1 with a precision of  $\approx 1 \text{ meV}$ . The other two transitions are in the visible spectrum and can be determined with a much higher precision, making the XUV transition No. 1 the limiting factor of this indirect measurement of the metastable state energy. When measuring these transitions, the indirect determination of the metastable state would be 2-3 orders of magnitude better than our current accuracy and the uncertainty will be within the 80-meV bandwidth of an XUV comb.

As an alternative, one could use XUV FEL lasers such as Fermi FEL in Trieste, Italy [\[Elet 20\]](#). XUV FEL spectroscopy can determine the transition energy with an uncertainty of  $\approx 10 \text{ meV}$ . After the emission spectroscopy or FEL spectroscopy, one would be able to go to XUV comb spectroscopy of the  $^4G_{7/2}$  state with an accuracy of around 21 kHz. Then, by adding two optical lasers, one could reach a similar accuracy for the clock transition by bridging over the  $^4G_{9/2}$  state [\[Lyu 23b\]](#). Since the  $^4G_{7/2}$  state decays very fast ( $1.3 \times 10^5 \text{ s}^{-1}$ ), all these procedures do not need to involve quantum logic schemes and will be very efficient. Another method could be to try to excite the metastable state:  $^2H_{11/2} \rightarrow ^4G_{9/2}$ . The

metastable state can be produced in the same way as it is described in the paper, see [Sec. 4.3](#), whereby one uses the population during HCI creation inside the EBIT with an approximate yield of 1/6 of the ions in the metastable state.

With these options one would get the transition energy of the metastable state  ${}^2H_{11/2}$  indirectly. With the improved value, the direct excitation would become more feasible. The rapid progress in XUV comb performance and coherence as well as ion trapping and cooling techniques will also benefit future experiments in this field.

### 5.3.4 Excited-state lifetime measurement

The duration of one contiguous measurement run at PENTATRAP is currently limited to roughly two days, after which one of the ions has usually undergone recombination with electrons from residual gas particles and is therefore no longer in the desired charge state. The metastable state in  ${}^{208}\text{Pb}^{41+}$  lives for 26.5(53) days which means it is highly unlikely to detect a decay inside the Penning traps at PENTATRAP before the ion recombines with an electron. However, using *ab initio* multiconfiguration Dirac-Hartree-Fock (MCDHF), one can find metastable states that have a shorter lifetime while still living long enough to load them into a Penning trap and determine their state, which can be done in the timescale of  $\approx 30$  min. For these states with lifetimes of around  $30 \text{ min} < \tau < 2 \text{ days}$  it would be possible to see a decay inside the Penning trap.

There is a new version of the cryogenic setup of PENTATRAP which will be tested soon and which is equipped with a cryogenic valve. These valves are known to improve the vacuum inside the Penning traps by orders of magnitude since they do not allow any residual molecular gas flow from the room temperature section into the cryogenic section [[Stur 19](#)]. With this valve, we should be able to see a decay in e.g. the metastable state in  ${}^{208}\text{Pb}^{41+}$ . Since there is currently no possibility to repump the ions into the excited state, a new ion in the metastable state would have to be loaded into the trap after every decay.

For testing a possible repumping scheme, a Penning-trap experiment is being set up: the Shanghai Penning trap (SH-Trap) [[Tu 23](#)]. To be able to repeatedly measure decays of the metastable state, an electron impact excitation is planned inside the Penning trap by the use of a field emission tip directly below the Penning trap. If the metastable state could be excited within the Penning trap with this method, one would have access to faster detection schemes and reach higher statistics for lifetime measurements. This would give insight into how hyperfine and magnetic quenching effects impact the metastable state lifetime [[Tu 23](#)].

# 6 Summary

This cumulative thesis, consisting of three peer reviewed publications, has demonstrated the unprecedented level of precision achievable with the Penning-trap mass spectrometer PENTATRAP. At the same time, the statistical and systematic limitations of the mass spectrometer were described and first promising tests of possible solutions were carried out.

In the first and second publication, the atomic masses of lead-208 and uranium-238 were determined to be

$$\begin{aligned} m(^{208}\text{Pb}) &= 207.976\,650\,494(14)\text{ u and} \\ m(^{238}\text{U}) &= 238.050\,787\,618(15)\text{ u,} \end{aligned}$$

which corresponds to a relative precision of 7 and  $6 \times 10^{-11}$ , respectively. These results improve the previously accepted values by around two orders of magnitude, which has a direct influence on the masses of 16 other nuclides related via different decays for which the energy is well known. As a result, new heavy mass references up to the actinide region of the nuclear chart are now available for nuclear structure studies of heavy and superheavy elements. A first determination of the image charge shift at PENTATRAP was successfully carried out during the measurement campaign of the uranium mass, improving the ICS precision to an uncertainty of 0.8% in Trap 2 and 1.7% in Trap 3. The total systematic uncertainty for this large  $\Delta m$  measurement was just  $2.5 \times 10^{-12}$  in Trap 2 and  $7.7 \times 10^{-12}$  in Trap 3. The atomic mass determination was therefore purely limited by the theoretical binding energy calculations of the missing electrons.

The new mass values also make it possible to determine the  $g$ -factor of the electron bound to a heavy nuclide to a high precision, which is planned to be examined at ALPHATRAP at the Max-Planck-Institute for Nuclear Physics in Heidelberg, Germany [Stur 19] and at ARTEMIS at the GSI in Darmstadt, Germany [Voge 19].  $g$ -factor measurements on hydrogen-like ions allow for stringent tests of bound-state QED in the strong field of the nucleus [Morg 23].

The third paper published within the scope of this thesis describes the detection of a

low-lying, metastable electronic state in  $^{208}\text{Pb}^{41+}$ . The energy of the metastable state was determined by measuring the motional frequencies of the highly charged lead ion in the metastable state and comparing them to the frequencies of the same ion in the electronic ground state. The energy was experimentally determined to be

$$E(^{208}\text{Pb}^{*41+}) = 31.2(8) \text{ eV}$$

which matches within  $1\sigma$  to the theoretical values of 31.68(13) eV and 31.76(35) eV. The *ab initio* multi-configuration Dirac Hartree Fock calculations of open shell ions could thereby be benchmarked and are being extended to similar systems in [Lyu 23a].

The metastable state in  $\text{Pb}^{41+}$ , measured within the scope of this thesis, as well as similar metastable states in [Lyu 23a] are promising candidates for future HCI clocks because they are widely shielded to external perturbations like black body radiation, and their extremely high quality factors would allow to build a very precise clock. The metastable state in  $\text{Pb}^{41+}$  lies in the XUV region in which several experimental groups are developing or have developed frequency combs [Pupe 21]. However, to find the transition with an XUV comb would require the transition energy to be known to higher precision. Due to the promising prospect of HCI clocks in the XUV, further investigation would be worthwhile and several possibilities for this have been described within this thesis. Lastly, the possibility of determining the lifetime of a metastable state in a Penning trap was discussed.

To decrease the downtime of the ion source during target exchanges and maintenance periods, a new TipEBIT was built and successfully commissioned, and the connecting beamline was designed and manufactured within the scope of this thesis. The new TipEBIT will be used as the second ion source for PENTATRAP so there will be no downtime during target change or EBIT maintenance.

At its current state and with the new techniques described in this thesis, PENTATRAP will continue to provide the world's most precise mass data in the future.



# Bibliography

- [Asto 27] F. W. Aston. [Atoms and their Packing Fractions](#). *Nature*, Vol. 120, No. 3035, pp. 956–959, Dec. 1927.
- [Audi 12] G. Audi, M. Wang, A. H. Wapstra, F. G. Kondev, M. MacCormick, and B. Pfeiffer. [The Ame2012 atomic mass evaluation](#). *Chin. Phys. C*, Vol. 36, No. 12, p. 1287, Dec. 2012.
- [Baue 22] S. Bauer, R. Behr, J. Herick, O. Kieler, M. Kraus, H. Tian, Y. Pimsut, and L. Palafox. [Josephson voltage standards as toolkit for precision metrological applications at PTB](#). *Meas. Sci. Technol.*, Vol. 34, No. 3, p. 032001, Dec. 2022.
- [Beie 00] T. Beier. [The  \$g\_j\$  factor of a bound electron and the hyperfine structure splitting in hydrogenlike ions](#). *Phys. Rep.*, Vol. 339, No. 2, pp. 79–213, Dec. 2000.
- [Bere 10] J. C. Berengut, V. A. Dzuba, and V. V. Flambaum. [Enhanced Laboratory Sensitivity to Variation of the Fine-Structure Constant using Highly Charged Ions](#). *Phys. Rev. Lett.*, Vol. 105, No. 12, p. 120801, Sep. 2010.
- [Bloc 22] M. Block, F. Giacoppo, F.-P. Heßberger, and S. Raeder. [Recent progress in experiments on the heaviest nuclides at SHIP](#). *Riv. Nuovo Cim.*, Vol. 45, No. 4, pp. 279–323, Apr. 2022.
- [Brad 36] N. E. Bradbury and R. A. Nielsen. [Absolute Values of the Electron Mobility in Hydrogen](#). *Phys. Rev.*, Vol. 49, No. 5, pp. 388–393, March 1936.
- [Brow 82] L. S. Brown and G. Gabrielse. [Precision spectroscopy of a charged particle in an imperfect Penning trap](#). *Phys. Rev. A*, Vol. 25, No. 4, pp. 2423–2425, Apr. 1982.
- [Brow 86] L. S. Brown and G. Gabrielse. [Geonium theory: Physics of a single electron or ion in a Penning trap](#). *Rev. Mod. Phys.*, Vol. 58, No. 1, pp. 233–311, Jan. 1986.
- [Cars 16] H. Carstens, M. Högner, T. Saule, S. Holzberger, N. Lilienfein, A. Guggenmos, C. Jocher, T. Eidam, D. Esser, V. Tosa, V. Pervak, J. Limpert, A. Tünnermann, U. Kleineberg, F. Krausz, and I. Pupeza. [High-harmonic generation at 250 MHz with photon energies exceeding 100 eV](#). *Optica*, Vol. 3, No. 4, pp. 366–369, Apr. 2016.
- [Corn 89] E. A. Cornell, R. M. Weisskoff, K. R. Boyce, R. W. Flanagan, G. P. Lafyatis, and D. E. Pritchard. [Single-ion cyclotron resonance measurement of  \$M\(\text{CO}^+\)/M\(\text{N}\_2^+\)\$](#) . *Phys. Rev. Lett.*, Vol. 63, No. 16, pp. 1674–1677, Oct. 1989.

- [Cres 16] J. R. Crespo López-Urrutia. [Frequency metrology using highly charged ions](#). *J. Phys.: Conf. Ser.*, Vol. 723, No. 1, p. 012052, June 2016.
- [Dick 24] S. Dickopf. *in preparation*. PhD thesis, Ruperto-Carola-University of Heidelberg, Germany, 2024.
- [Door 18] M. Door. *New control system and first trap characterization measurements at the high-precision Penning-trap mass spectrometer PENTATRAP*. Master thesis, Ruperto-Carola-University of Heidelberg, Germany, 2018.
- [Door 24] M. Door. *in preparation*. PhD thesis, Ruperto-Carola-University of Heidelberg, Germany, 2024.
- [Dorr 15] A. Dörr. *PENTATRAP: A novel Penning-trap system for high-precision mass measurements*. PhD thesis, Ruperto-Carola-University of Heidelberg, Germany, 2015.
- [DREE] [DREEBIT GmbH - DREEBIT Company | DE](https://www.dreebit.com/de/). <https://www.dreebit.com/de/>.
- [Dwor 10] M. Dworschak, M. Block, D. Ackermann, G. Audi, K. Blaum, C. Droese, S. Eliseev, T. Fleckenstein, E. Haettner, F. Herfurth, F. P. Heßberger, S. Hofmann, J. Ketelaer, J. Ketter, H.-J. Kluge, G. Marx, M. Mazzocco, Yu. N. Novikov, W. R. Plaß, A. Popeko, S. Rahaman, D. Rodríguez, C. Scheidenberger, L. Schweikhard, P. G. Thirolf, G. K. Vorobyev, M. Wang, and C. Weber. [Penning trap mass measurements on nobelium isotopes](#). *Phys. Rev. C*, Vol. 81, No. 6, p. 064312, June 2010.
- [Eddi 20] A. S. Eddington. [The Internal Constitution of the Stars](#). *The Scientific Monthly*, Vol. 11, No. 4, pp. 297–303, 1920.
- [Elet 20] [Elettra Sincrotrone Trieste](https://www.elettra.eu/lightsources/fermi/fermi-machine/general-description.html). <https://www.elettra.eu/lightsources/fermi/fermi-machine/general-description.html>, Nov. 2020.
- [Feng 96] X. Feng, M. Charlton, M. Holzscheiter, R. A. Lewis, and Y. Yamazaki. [Tank circuit model applied to particles in a Penning trap](#). *J. Appl. Phys.*, Vol. 79, No. 1, pp. 8–13, Jan. 1996.
- [Fili 21] P. Filianin, C. Lyu, M. Door, K. Blaum, W. Huang, M. Haverkort, P. Indelicato, C. Keitel, K. Kromer, D. Lange, Y. Novikov, A. Rischka, R. Schüssler, C. Schweiger, S. Sturm, S. Ulmer, Z. Harman, and S. Eliseev. [Direct  \$Q\$ -Value Determination of the  \$\beta^-\$  Decay of  \$^{187}\text{Re}\$](#) . *Phys. Rev. Lett.*, Vol. 127, No. 7, p. 072502, Aug. 2021.

- 
- [Fink 20] D. J. Fink and E. G. Myers. Deuteron-to-Proton Mass Ratio from the Cyclotron Frequency Ratio of  $\text{H}_2^+$  to  $\text{D}^+$  with  $\text{H}_2^+$  in a Resolved Vibrational State. *Phys. Rev. Lett.*, Vol. 124, No. 1, p. 013001, Jan. 2020.
- [Gabr 89] G. Gabrielse, L. Haarsma, and S. L. Rolston. Open-endcap Penning traps for high precision experiments. *Int. J. Mass Spectrom. Ion Processes*, Vol. 88, No. 2, pp. 319–332, Apr. 1989.
- [Gohl 05] C. Gohle, T. Udem, M. Herrmann, J. Rauschenberger, R. Holzwarth, H. A. Schuessler, F. Krausz, and T. W. Hänsch. A frequency comb in the extreme ultraviolet. *Nature*, Vol. 436, No. 7048, pp. 234–237, July 2005.
- [Gram 22] M. A. Gramberg. *Aufbau und Inbetriebnahme einer Raumtemperatur-Elektronenstrahl-Ionenfalle*. Bachelor thesis, Ruperto-Carola-University of Heidelberg, Germany, 2022.
- [Haff 00] H. Häffner. *Präzisionsmessung des magnetischen Moments des Elektrons in wasserstoffähnlichem Kohlenstoff*. PhD thesis, Johannes Gutenberg-Universität Mainz, 2000.
- [Hall 06] J. L. Hall. Nobel Lecture: Defining and measuring optical frequencies. *Rev. Mod. Phys.*, Vol. 78, No. 4, pp. 1279–1295, Nov. 2006.
- [Hans 06] T. W. Hänsch. Nobel Lecture: Passion for precision. *Rev. Mod. Phys.*, Vol. 78, No. 4, pp. 1297–1309, Nov. 2006.
- [Heis 23] F. Heisse, M. Door, T. Sailer, P. Filianin, J. Herkenhoff, C. König, K. Kromer, D. Lange, J. Morgner, A. Rischka, C. Schweiger, B. Tu, Y. Novikov, S. Eliseev, S. Sturm, and K. Blaum. High-Precision Determination of  $g$  Factors and Masses of  $^{20}\text{Ne}^{9+}$  and  $^{22}\text{Ne}^{9+}$ . *Phys. Rev. Lett.*, Vol. 131, No. 25, p. 253002, Dec. 2023.
- [Herk 21] J. Herkenhoff, M. Door, P. Filianin, W. Huang, K. Kromer, D. Lange, R. X. Schüssler, C. Schweiger, S. Eliseev, and K. Blaum. A digital feedback system for advanced ion manipulation techniques in Penning traps. *Rev. Sci. Instrum.*, Vol. 92, No. 10, p. 103201, Oct. 2021.
- [Huan 21] W. J. Huang, M. Wang, F. G. Kondev, G. Audi, and S. Naimi. The AME 2020 atomic mass evaluation (I). Evaluation of input data, and adjustment procedures\*. *Chin. Phys. C*, Vol. 45, No. 3, p. 030002, March 2021.
- [Hukk 23] M. Hukkanen, W. Ryssens, P. Ascher, M. Bender, T. Eronen, S. Grévy, A. Kankainen, M. Stryjczyk, L. Al Ayoubi, S. Ayet, O. Beliuskina, C. Delafosse,

- W. Gins, M. Gerbaux, A. Husson, A. Jokinen, D. A. Nesterenko, I. Pohjalainen, M. Reponen, S. Rinta-Antila, A. De Roubin, and A. P. Weaver. [Odd-odd neutron-rich rhodium isotopes studied with the double Penning trap JYFLTRAP](#). *Phys. Rev. C*, Vol. 107, No. 1, p. 014306, Jan. 2023.
- [Jones 05] R. J. Jones, K. D. Moll, M. J. Thorpe, and J. Ye. [Phase-Coherent Frequency Combs in the Vacuum Ultraviolet via High-Harmonic Generation inside a Femtosecond Enhancement Cavity](#). *Phys. Rev. Lett.*, Vol. 94, No. 19, p. 193201, May 2005.
- [Julin 01] R. Julin. [In-beam spectroscopy of heavy actinides](#). *Nucl. Phys. A*, Vol. 685, No. 1, pp. 221–232, March 2001.
- [Kais 24] A. Kaiser, S. Dickopf, M. Door, R. Behr, U. Beutel, S. Eliseev, A. Kaushik, K. Kromer, M. Müller, L. Palafox, S. Ulmer, A. Mooser, and K. Blaum. [Josephson voltage standards as ultra-stable low-noise voltage source for precision penning-trap experiments](#). *in preperation*, 2024.
- [Kars 05] S. G. Karshenboim. [Precision physics of simple atoms: QED tests, nuclear structure and fundamental constants](#). *Phys. Rep.*, Vol. 422, No. 1, pp. 1–63, Dec. 2005.
- [Kart 19a] J. Karthein. [Nuclear chart plotter](#). <https://github.com/jonas-ka/nuclear-chart-plotter>, 2019.
- [Kart 19b] J. Karthein, D. Atanasov, K. Blaum, S. Eliseev, P. Filianin, D. Lunney, V. Manea, M. Mougeot, D. Neidherr, Y. Novikov, L. Schweikhard, A. Welker, F. Wienholtz, and K. Zuber. [Direct decay-energy measurement as a route to the neutrino mass](#). *Hyperfine Interact.*, Vol. 240, No. 1, p. 61, June 2019.
- [Kett 14] J. Ketter, T. Eronen, M. Höcker, S. Streubel, and K. Blaum. [First-order perturbative calculation of the frequency-shifts caused by static cylindrically-symmetric electric and magnetic imperfections of a Penning trap](#). *Int. J. Mass Spectrom.*, Vol. 358, pp. 1–16, Jan. 2014.
- [King 22] S. A. King, L. J. Spieß, P. Micke, A. Wilzewski, T. Leopold, E. Benkler, R. Lange, N. Huntemann, A. Surzhykov, V. A. Yerokhin, J. R. Crespo López-Urrutia, and P. O. Schmidt. [An optical atomic clock based on a highly charged ion](#). *Nature*, Vol. 611, No. 7934, pp. 43–47, Nov. 2022.
- [Koiv 98] H. Koivisto, J. Arje, and M. Nurmi. [Metal ions from the volatile compounds method for the production of metal ion beams](#). *Rev. Sci. Instrum.*, Vol. 69, No. 2, pp. 785–787, Feb. 1998.

- 
- [Kond 21] F. G. Kondev, M. Wang, W. J. Huang, S. Naimi, and G. Audi. [The NUBASE2020 evaluation of nuclear physics properties](#). *Chin. Phys. C*, Vol. 45, No. 3, p. 030001, March 2021.
- [Kozl 18] M. G. Kozlov, M. S. Safronova, J. R. Crespo López-Urrutia, and P. O. Schmidt. [Highly charged ions: Optical clocks and applications in fundamental physics](#). *Rev. Mod. Phys.*, Vol. 90, No. 4, p. 045005, Dec. 2018.
- [Krom 19] K. Kromer. [Environmentally-induced systematic effects at the high-precision mass spectrometer PENTATRAP](#). Master thesis, Ruperto-Carola-University of Heidelberg, Germany, 2019.
- [Lang 96] K. Langanke and C. A. Barnes. [Nucleosynthesis in the big bang and in stars](#). *Adv. Nucl. Phys.*, Vol. 22, pp. 173–263, 1996.
- [Ludl 15] A. D. Ludlow, M. M. Boyd, J. Ye, E. Peik, and P. O. Schmidt. [Optical atomic clocks](#). *Rev. Mod. Phys.*, Vol. 87, No. 2, pp. 637–701, June 2015.
- [Lunn 03] D. Lunney, J. M. Pearson, and C. Thibault. [Recent trends in the determination of nuclear masses](#). *Rev. Mod. Phys.*, Vol. 75, No. 3, pp. 1021–1082, Aug. 2003.
- [Lyu 23a] C. Lyu, Z. Harman, and C. H. Keitel. [Ultrastable optical, XUV and soft-x-ray clock transitions in open-shell highly charged ion](#). *submitted*, 2023.
- [Lyu 23b] C. Lyu. internal communication. 2023.
- [Maye 48] M. G. Mayer. [On Closed Shells in Nuclei](#). *Phys. Rev.*, Vol. 74, No. 3, pp. 235–239, Aug. 1948.
- [Mick 18] P. Micke, S. Kühn, L. Buchauer, J. R. Harries, T. M. Bücking, K. Blaum, A. Cieluch, A. Egl, D. Hollain, S. Kraemer, T. Pfeifer, P. O. Schmidt, R. X. Schüssler, Ch. Schweiger, T. Stöhlker, S. Sturm, R. N. Wolf, S. Bernitt, and J. R. Crespo López-Urrutia. [The Heidelberg compact electron beam ion traps](#). *Rev. Sci. Instrum.*, Vol. 89, No. 6, p. 063109, June 2018.
- [Mick 20] P. Micke, T. Leopold, S. A. King, E. Benkler, L. J. Spieß, L. Schmöger, M. Schwarz, J. R. Crespo López-Urrutia, and P. O. Schmidt. [Coherent laser spectroscopy of highly charged ions using quantum logic](#). *Nature*, Vol. 578, No. 7793, pp. 60–65, Feb. 2020.
- [Mohr 98] P. J. Mohr, G. Plunien, and G. Soff. [QED corrections in heavy atoms](#). *Phys. Rep.*, Vol. 293, No. 5-6, pp. 227–369, Jan. 1998.

- [Morg 23] J. Morgner, B. Tu, C. M. König, T. Sailer, F. Heiße, H. Bekker, B. Sikora, C. Lyu, V. A. Yerokhin, Z. Harman, J. R. Crespo López-Urrutia, C. H. Keitel, S. Sturm, and K. Blaum. [Stringent test of QED with hydrogen-like tin](#). *Nature*, Vol. 622, No. 7981, pp. 53–57, Oct. 2023.
- [Mull 13] F. Müller, T. Scheller, R. Wendisch, R. Behr, O. Kieler, L. Palafox, and J. Kohlmann. [NbSi Barrier Junctions Tuned for Metrological Applications up to 70 GHz: 20 V Arrays for Programmable Josephson Voltage Standards](#). *IEEE Transactions on Applied Superconductivity*, Vol. 23, No. 3, pp. 1101005–1101005, June 2013.
- [Myer 13] E. G. Myers. [The most precise atomic mass measurements in Penning traps](#). *Int. J. Mass Spectrom.*, Vol. 349–350, pp. 107–122, Sep. 2013.
- [Nils 55] S. G. Nilsson. [Binding states of individual nucleons in strongly deformed nuclei](#). *Dan. Mat. Fys. Medd.*, Vol. 29, No. 16, pp. 1–69, 1955.
- [Ogan 12] Y. Oganessian. [Nuclei in the "Island of Stability" of Superheavy Elements](#). *J. Phys.: Conf. Ser.*, Vol. 337, p. 012005, Feb. 2012.
- [Pove 01] A. Poves and F. Nowacki. [The nuclear shell model](#). In: J. M. Arias and M. Lozano, Eds., *An Advanced Course in Modern Nuclear Physics*, pp. 70–101, Springer, Berlin, Heidelberg, 2001.
- [Pupe 13] I. Pupeza, S. Holzberger, T. Eidam, H. Carstens, D. Esser, J. Weitenberg, P. Rußbüldt, J. Rauschenberger, J. Limpert, T. Udem, A. Tünnermann, T. W. Hänsch, A. Apolonski, F. Krausz, and E. Fill. [Compact high-repetition-rate source of coherent 100 eV radiation](#). *Nat. Photonics*, Vol. 7, No. 8, pp. 608–612, Aug. 2013.
- [Pupe 21] I. Pupeza, C. Zhang, M. Högner, and J. Ye. [Extreme-ultraviolet frequency combs for precision metrology and attosecond science](#). *Nat. Photonics*, Vol. 15, No. 3, pp. 175–186, March 2021.
- [Rain 04] S. Rainville, J. K. Thompson, and D. E. Pritchard. [An Ion Balance for Ultra-High-Precision Atomic Mass Measurements](#). *Science*, Vol. 303, No. 5656, pp. 334–338, Jan. 2004.
- [Rain 05] S. Rainville, J. K. Thompson, E. G. Myers, J. M. Brown, M. S. Dewey, E. G. Kessler, R. D. Deslattes, H. G. Börner, M. Jentschel, P. Mutti, and D. E. Pritchard. [A direct test of  \$E = mc^2\$](#) . *Nature*, Vol. 438, No. 7071, pp. 1096–1097, Dec. 2005.

- [Repp 12] J. Repp, C. Böhm, J. R. Crespo López-Urrutia, A. Dörr, S. Eliseev, S. George, M. Goncharov, Y. N. Novikov, C. Roux, S. Sturm, S. Ulmer, and K. Blaum. [PENTATRAP: A novel cryogenic multi-Penning-trap experiment for high-precision mass measurements on highly charged ions.](#) *Appl. Phys. B*, Vol. 107, No. 4, pp. 983–996, June 2012.
- [Risc 14] A. Rischka. *Aufbau des Stabilisierungssystems des Heliumdrucks und Heliumlevels und Konstruktion eines kryogenen Faraday-Bechers für PENTATRAP.* Master thesis, Ruperto-Carola-University of Heidelberg, Germany, 2014.
- [Risc 18] A. Rischka. *The First Direct  $Q_{EC}$  Measurement in  $^{163}\text{Ho}$  and the Development of the High-Precision Mass Spectrometer PENTATRAP for Neutrino Physics.* PhD thesis, Ruperto-Carola-University of Heidelberg, Germany, 2018.
- [Risc 20] A. Rischka, H. Cakir, M. Door, P. Filianin, Z. Harman, W. Huang, P. Indelicato, C. Keitel, C. König, K. Kromer, M. Müller, Y. Novikov, R. Schüssler, C. Schweiger, S. Eliseev, and K. Blaum. [Mass-Difference Measurements on Heavy Nuclides with an  \$\text{eV}/c^2\$  Accuracy in the PENTATRAP Spectrometer.](#) *Phys. Rev. Lett.*, Vol. 124, No. 11, p. 113001, March 2020.
- [Roux 12a] C. Roux, C. Böhm, A. Dörr, S. Eliseev, S. George, M. Goncharov, Y. N. Novikov, J. Repp, S. Sturm, S. Ulmer, and K. Blaum. [The trap design of PENTATRAP.](#) *Appl. Phys. B*, Vol. 107, No. 4, pp. 997–1005, June 2012.
- [Roux 12b] C.-E. Roux. *High-Resolution Mass Spectrometry: The trap design and detection system of Pentatrap and new  $Q$ -values for neutrino studies.* PhD thesis, Ruperto-Carola-University of Heidelberg, Germany, 2012.
- [Sasi 23] S. Sasidharan, O. Bezrodnova, S. Rau, W. Quint, S. Sturm, and K. Blaum. [Penning-Trap Mass Measurement of Helium-4.](#) *Phys. Rev. Lett.*, Vol. 131, No. 9, p. 093201, Aug. 2023.
- [Saul 19] T. Saule, S. Heinrich, J. Schötz, N. Lilienfein, M. Högner, O. deVries, M. Plötner, J. Weitenberg, D. Esser, J. Schulte, P. Russbueldt, J. Limpert, M. F. Kling, U. Kleineberg, and I. Pupeza. [High-flux ultrafast extreme-ultraviolet photoemission spectroscopy at 18.4 MHz pulse repetition rate.](#) *Nat. Commun.*, Vol. 10, No. 1, p. 458, Jan. 2019.
- [Schu 19a] M. Schuh, F. Heiße, T. Eronen, J. Ketter, F. Köhler-Langes, S. Rau, T. Segal, W. Quint, S. Sturm, and K. Blaum. [Image charge shift in high-precision Penning traps.](#) *Phys. Rev. A*, Vol. 100, No. 2, p. 023411, Aug. 2019.

- [Schu 19b] R. Schüßler. *First High-Precision Mass Measurements at PENTATRAP on highly charged Xe and Re ions*. PhD thesis, Ruperto-Carola-University of Heidelberg, Germany, 2019.
- [Schu 20] R. X. Schüssler, H. Bekker, M. Braß, H. Cakir, J. R. Crespo López-Urrutia, M. Door, P. Filianin, Z. Harman, M. W. Haverkort, W. J. Huang, P. Indelicato, C. H. Keitel, C. M. König, K. Kromer, M. Müller, Y. N. Novikov, A. Rischka, C. Schweiger, S. Sturm, S. Ulmer, S. Eliseev, and K. Blaum. [Detection of metastable electronic states by Penning trap mass spectrometry](#). *Nature*, Vol. 581, No. 7806, pp. 42–46, May 2020.
- [Schw 17] C. Schweiger. *Construction and commissioning of a room-temperature electron beam ion trap and development of a wire probe injection system*. Master thesis, Ruperto-Carola-University of Heidelberg, Germany, 2017.
- [Schw 19] Ch. Schweiger, C. M. König, J. R. Crespo López-Urrutia, M. Door, H. Dorrer, Ch. E. Düllmann, S. Eliseev, P. Filianin, W. Huang, K. Kromer, P. Micke, M. Müller, D. Renisch, A. Rischka, R. X. Schüssler, and K. Blaum. [Production of highly charged ions of rare species by laser-induced desorption inside an electron beam ion trap](#). *Rev. Sci. Instrum.*, Vol. 90, No. 12, p. 123201, Dec. 2019.
- [Schw 22] C. Schweiger, M. Door, P. Filianin, J. Herkenhoff, K. Kromer, D. Lange, D. Marschall, A. Rischka, T. Wagner, S. Eliseev, and K. Blaum. [Fast silicon carbide MOSFET based high-voltage push-pull switch for charge state separation of highly charged ions with a Bradbury–Nielsen gate](#). *Rev. Sci. Instrum.*, Vol. 93, No. 9, p. 094702, Sep. 2022.
- [Shab 18] V. M. Shabaev, A. I. Bondarev, D. A. Glazov, M. Y. Kaygorodov, Y. S. Kozhedub, I. A. Maltsev, A. V. Malyshev, R. V. Popov, I. I. Tupitsyn, and N. A. Zubova. [Stringent tests of QED using highly charged ions](#). *Hyperfine Interact.*, Vol. 239, No. 1, p. 60, Nov. 2018.
- [Sobi 07] A. Sobiczewski and K. Pomorski. [Description of structure and properties of superheavy nuclei](#). *Prog. Part. Nucl. Phys.*, Vol. 58, No. 1, pp. 292–349, Jan. 2007.
- [Stur 14] S. Sturm, F. Köhler, J. Zatorski, A. Wagner, Z. Harman, G. Werth, W. Quint, C. H. Keitel, and K. Blaum. [High-precision measurement of the atomic mass of the electron](#). *Nature*, Vol. 506, No. 7489, pp. 467–470, Feb. 2014.
- [Stur 19] S. Sturm, I. Arapoglou, A. Egl, M. Höcker, S. Kraemer, T. Sailer, B. Tu, A. Weigel, R. Wolf, J. C. López-Urrutia, and K. Blaum. [The ALPHATRAP](#)



- experiment. *Eur. Phys. J. Spec. Top.*, Vol. 227, No. 13, pp. 1425–1491, Feb. 2019.
- [Tu 23] B. Tu, R. Si, Y. Shen, J. Wang, B. Wei, C. Chen, K. Yao, and Y. Zou. [Experimental access to observing decay from extremely long-lived metastable electronic states via Penning trap spectrometry](#). *Phys. Rev. Research*, Vol. 5, No. 4, p. 043014, Oct. 2023.
- [Voge 19] M. Vogel, M. S. Ebrahimi, Z. Guo, A. Khodaparast, G. Birkl, and W. Quint. [Electron Magnetic Moment in Highly Charged Ions: The ARTEMIS Experiment](#). *Ann. Phys. (Berl.)*, Vol. 531, No. 5, p. 1800211, 2019.
- [Wang 21] M. Wang, W. J. Huang, F. G. Kondev, G. Audi, and S. Naimi. [The AME 2020 atomic mass evaluation \(II\). Tables, graphs and references](#). *Chin. Phys. C*, Vol. 45, No. 3, p. 030003, March 2021.
- [Yudi 14] V. I. Yudin, A. V. Taichenachev, and A. Derevianko. [Magnetic-Dipole Transitions in Highly Charged Ions as a Basis of Ultraprecise Optical Clocks](#). *Phys. Rev. Lett.*, Vol. 113, No. 23, p. 233003, Dec. 2014.
- [Zato 17] J. Zatorski, B. Sikora, S. G. Karshenboim, S. Sturm, F. Köhler-Langes, K. Blaum, C. H. Keitel, and Z. Harman. [Extraction of the electron mass from g-factor measurements on light hydrogenlike ions](#). *Phys. Rev. A*, Vol. 96, No. 1, p. 012502, July 2017.

## Acknowledgment

Mein besonderer Dank geht an dieser Stelle an alle, die mich während meiner Doktorarbeit unterstützt haben. Ohne euch wäre diese Arbeit nicht möglich gewesen.

Zu allererst geht mein Dank an Klaus Blaum. Lieber Klaus, vielen Dank für deine Erreichbarkeit üblicherweise innerhalb von 5 min und deine ganze Unterstützung. Danke für die Möglichkeiten die du uns bietest wie die Teilnahme an Konferenzen überall auf der Welt, Tagesausflüge an Forschungsinstitute, die Möglichkeit unsere Ergebnisse zu publizieren, was du nicht nur unterstützt sondern auch Schritt für Schritt begleitest und vieles mehr. Danke, dass du mir die Möglichkeit geboten hast, bei einem so erfolgreichen Experiment mitzuwirken.

Vielen Dank an Selim Jochim für die Übernahme des Zweitgutachtens!

Vielen Dank an das ganze PENTATRAP Team! Sergey Eliseev, Pavel Filianin, Menno Door, Jost Herkenhoff, Lucia Enzmann und Jan Nägele in der aktuellen Konstellation aber auch die ehemaligen Mitglieder Daniel Lange, Christoph Schweiger, Alexander Rischka, Rima Schüssler und viele mehr: Es hat mir viel Spaß bereitet mit euch zusammen zu arbeiten. Die vielen hilfreichen Diskussionen, das Kaffeetrinken, EMBL Ausflüge oder das gemeinsame Rätseln über Experiment-Probleme haben den Alltag am Experiment immer kurzweilig sein lassen. Auch wenn das Experiment mal nicht so wollte wie wir, haben wir es gemeinsam doch immer wieder hingebogen und verbessert oder das Problem im Zweifel "russian style" behoben. Mein besonderer Dank geht an Menno Door und Christoph Schweiger, für die vielen lustigen Stunden im Labor und Kontrollraum, unzählige fruchtbare Diskussionen und den tollen Zusammenhalt selbst in den schwierigen Zeiten der Pandemie.

Vielen Dank an Gabi Weese und Ludmila Hollmach, die guten Seelen unserer Abteilung ohne deren Organisation die Abteilung vermutlich im Chaos versinken würde.

Thanks to all the fellow Penning trappers from ALPHATRAP, LIONTRAP, and  $\mu$ TE<sub>x</sub> for great lunches, interesting discussions, help whenever needed, and fun MATSdays with ice-cold swimming breaks. The combined knowledge between our groups meant that I never had to search for an answer long and the probability of facing the same problems signifies the solution will probably be known already and shared without hesitation. Thank you for that- it is by no means a matter of course.

Mein Dank gilt ebenfalls den MPIK Werkstätten. Dem MPIK-Konstruktionsbüro unter der Leitung von Frank Müller für die Umsetzung der experimentellen Bauteile. Ein besonderer Dank an Yannick Steinhauser für die schönen Renderings des PENTATRAP Experiments für diese Arbeit. Vielen Dank an die Zentrale Feinwerktechnik unter der Leitung von Thorsten Spranz für die präzise Fertigung sämtlicher Bauteile für das Experiment und Uwe Zeiske für

diverse spontane Kleinaufträge. Der IT gilt mein Dank für den Rückhalt auf Computerseite und das schnelle Lösen sämtlicher Probleme der Server oder des PENTATRAP Netzwerks. Danke auch der Elektronik unter der Leitung von Thomas Wagner für das Bauen von elektronischen Speziallösungen für die sehr spezifischen Anforderungen eines Präzisionsexperimentes.

Ein ganz besonderer Dank geht auch an meine ganze Familie. Meine Eltern, Ursula und Thomas Kromer, die mit drei Kids die einen PhD machen wirklich alle Hände voll zu tun haben aber trotzdem zu jeder Zeit ein offenes Ohr für große und kleine Probleme haben und uns ohne Ende unterstützen. Mom, danke für deine fleißigen sprachlichen Korrekturen der Arbeit sowie der Paper! An meine Geschwister Christian und Daniela Kromer für eure Unterstützung und die schönen Gespräche unter Leidensgenossen und ebenfalls für die Korrekturen der Arbeit.

Lieber Jost, vielen Dank für all deine Unterstützung! Von der teils mehrfachen Korrektur sämtlicher Paper und der gesamten Doktorarbeit bis zur Beruhigung wenn bei mir die Nerven mal wieder blank lagen, kann ich gar nicht ausdrücken wie sehr du mir die letzten Jahre geholfen hast. Es war immer wunderbar zu wissen, dass dein offenes Ohr und dein breites Wissen nur ein paar Bürotüren entfernt auf mich warten.

Danke!